

UNIVERSITY OF OKLAHOMA

GRADUATE COLLEGE

Examining Novel Profiling Systems and Their Synergy for Advancing

Boundary-Layer Research

A DISSERTATION

SUBMITTED TO THE GRADUATE FACULTY

in partial fulfillment of the requirements for the

Degree of

DOCTOR OF PHILOSOPHY

By

TYLER MATTHEW BELL

Norman, Oklahoma

2021

Examining Novel Profiling Systems and Their Synergy for Advancing  
Boundary-Layer Research

A DISSERTATION APPROVED FOR THE  
SCHOOL OF METEOROLOGY

BY THE COMMITTEE CONSISTING OF

Dr. Petra Klein, Chair

Dr. Phillip Chilson

Dr. Scott Salesky

Dr. Chris Fiebrich

Dr. Jeff Kelly

© Copyright by TYLER MATTHEW BELL2021  
All Rights Reserved.

## Acknowledgments

It was a great privilege to have the funding to pursue this research. Support for this research came from a variety of sources including the National Science Foundation (NSF) Office of Integrative Activities (grant no. 1539070), the National Mesonet Program with funding through Earth Networks, Inc., the National Oceanic and Atmospheric Administration (NOAA; grant no. NA19OAR4590218), and internal funding through the University of Oklahoma's Office of the Vice President for Research and Partnerships. Without this wide array of funding resources, this research would not be possible.

It is also a great privilege to be part of such a unique community within the National Weather Center and the surrounding research campus. I would not be the person I am today without the support of the people on this campus.

I would like to thank my committee for always being supportive and timely with the large amount of paperwork that it takes to pursue a graduate degree. Dr. Scott Salesky and Dr Chris Fiebrich agreed to continue to serve on my committee after I completed my masters and have continued to help me push the science forward. Their support and kind words are invaluable. I am thankful for my graduate college representative, Dr. Jeff Kelly, for stepping in to the role after my previous representative left the university and for taking such an interest in the research and finding new applications for it.

I am also incredibly thankful for Dr. Phillip Chilson for being my advisor for the majority of my doctoral studies. I have worked with Dr. Chilson on many different projects since starting my research career under his guidance as an undergraduate student studying bats with weather radar. The various projects have certainly been a wild ride, and the many ups and downs have shaped me into a better scientist.

I also want to thank Dr. Petra Klein for stepping back in to fill my advisor role when Dr. Chilson decided to make a career change. The guidance provided during

past few months has been invaluable. The constructive criticism and encouragement have made the last part of my studies something I will be eternally grateful for.

There is also a slew of friends and colleagues I need to thank. I want to thank the various students I have been fortunate mentor the past few years: Ariel Jacobs, Tyler Pardun, Cha'lita Thompson, Isaac Medina, Dana Pawlowski, Marshall Baldwin, and Victor Alvarez. It has been a pleasure to watch them grow as scientists and I can only hope that I helped them learn something new; I certainly learned a lot from them. I also want to thank all of my office-mates and colleagues from when CASS was still around: Brian Greene, Francesca Lappin, Tony Segales, Liz Pillar-Little, Gus Azevedo, and Bill Doyle. This group pushed the boundaries of what is possible and the weather community will reap the benefits of this effort for years to come. Dr. David Turner has been an invaluable resource for learning about retrieval science, and I look forward to continuing to work with him on this topic. Along these same lines, I also want to thank Dr. Joshua Gebauer for contributing to this science and for always looking to push the limits of it. I also want to thank him, and Dr. Christopher Riedel, for being great company while fishing. We may not always catch very much, but we always have a good time. Thanks also to Kathryn Gebauer for looking over this document and informing me that I need to use more dashes. Dr. Jeremy Gibbs has been a great friend and colleague, especially in the last few months. Though it may not seem like it, his continued advice to be sure to take a step back every once in a while has been incredibly helpful. I also want to give a huge thank you to Dr. Elizabeth Smith for being a fantastic colleague, mentor, and friend over the years. Even through the highs and lows, she was always there with encouragement and advice. Thank you for trusting me to help build out that vision we dreamed up in the old graduate student office. I look forward to continuing to build it out in the years to come.

Lastly, I want to thank my family for the support over the years. They always wanted me to be a medical doctor, so hopefully a PhD in Meteorology will suffice. Finally, I am very grateful to Katelyn Bell for her love and support as I pursued my PhD. Even though it often meant I was away from home, I always came back to loving arms. I would not have been able to do it without her. Thank you.

# Table of Contents

Acknowledgments	iv
List of Tables	ix
List of Figures	x
Abstract	xvii
<b>1 Introduction</b>	<b>1</b>
1.1 Model Deficiencies	5
1.2 The Observational Data Gap	10
1.3 Possible Data Gap Solutions	12
1.3.1 Ground-Based Remote Sensors	12
1.3.1.1 Doppler Lidars	14
1.3.1.2 Microwave Radiometers	17
1.3.1.3 Infrared Spectrometers	18
1.3.1.4 TROPoe	19
1.3.2 Weather-Sensing Uncrewed Aerial Systems	21
1.3.2.1 The CopterSonde	23
1.4 Research Questions	25
<b>2 Field Campaigns</b>	<b>26</b>
2.1 VORTEX-SE	26
2.2 LAPSE-RATE	28
2.3 Flux Capacitor	30
<b>3 Instrument Intercomparison</b>	<b>33</b>
3.1 Statistical Comparison of Systems	33
3.1.1 CLAMPS vs CopterSonde	35
3.1.2 Radiosonde vs CopterSonde	36
3.1.3 Radiosonde vs CLAMPS	37
3.2 Case Studies	38
3.2.1 LAPSE-RATE Case Study	38
3.2.2 Flux Capacitor Case	39
3.3 Issues Identified	40
<b>4 Identifying instrument synergy</b>	<b>53</b>
4.1 UAS Wind Speed Estimates	53
4.1.1 Ascending vs Loiter	58
4.1.2 Density correction	59

4.1.3	Non-linear fits . . . . .	62
4.2	Thermodynamic Retrievals . . . . .	63
4.2.1	Examining the effect of the prior during VORTEX-SE . . . . .	65
4.2.1.1	Superadiabatic max height . . . . .	72
4.2.2	Impact of using WxUAS . . . . .	77
<b>5</b>	<b>Instrument Synergy</b>	<b>91</b>
<b>6</b>	<b>Conclusions</b>	<b>97</b>
6.1	Limitations . . . . .	98
6.2	Looking Forward . . . . .	99
	<b>Reference List</b>	<b>102</b>
	<b>Appendix A</b>	
	. . . . .	116



## List of Tables

2.1	Summary of dates, locations, and the instruments present during the field campaigns discussed in Chapter 2. . . . .	27
4.1	Summary of CopterSonde measurement specifications based on the results of this study when compared to the Vaisala RS92-SGP data used in Chapter 3 . . . . .	79
A.1	Summary of results from the TROPoe tests presented in Section 4.2.2. The temperature and WVMR bias are relative to the measurements collected by the co-located Vaisala RS92-SGP radiosondes. The standard deviation is the standard deviation of the differences between the measurements from the retrieval and the radiosonde. . . . .	117

## List of Figures

1.1	A conceptual model of the ABL based on Stull (1988). The left panel shows a time-height figure of how the boundary layer grows throughout the diurnal cycle. Theoretical mean temperature profiles from throughout the diurnal cycle are shown on the right and correspond with the vertical lines on the left. The free atmosphere (FA), capping inversion (CI), entrainment zone (EZ), residual layer (RL), mixed layer (ML), and stable boundary layer (SBL) are labeled. . . . .	2
1.2	A 24-hour time-height cross section of temperature data collected by the CopterSonde during Flux Capacitor. Also shown are two radiosondes (two vertical lines with color fill) and 10 m Washington, OK Mesonet temperature measurements. Note the amount and fidelity of the CopterSonde data compared to the operational observations. During the overnight period, the nocturnal LLJ was too strong to fly the CopterSonde over 400 m. . . . .	9
1.3	Theoretical brightness temperatures calculated for the standard atmosphere at a $0^\circ$ (zenith) viewing angle (blue line) and an $80^\circ$ (off-zenith) viewing angle (red). Vertical gray lines indicate the frequencies measured on the HATPRO Version 4 in CLAMPS1. (Figure courtesy of Dave Turner, NOAA Global Systems Laboratory) . . . . .	16
2.1	Caption . . . . .	28
2.2	Key locations during the LAPSE-RATE field campaign in 2017. CLAMPS1 and CopterSondes were deployed at the Moffat School. Other WxUAS were flown at both Saguache Airfield and Leach Airfield, but are not examined in the following studies. . . . .	31

3.1	Two-dimensional histograms of DL measured wind speed vs CopterSonde measured wind speed (a) and DL measured wind direction vs CopterSonde measured wind direction (c). The 2D histograms are binned to $0.5 \text{ m s}^{-1}$ for wind speed and 5 degrees for wind direction. The histograms on the right show the difference in wind speed (b) and wind direction (d). The red dotted line is the 1-to-1 line and the black dotted line is the least-squares regression. The slope (m) and intercept (b) are shown in the titles. Various other statistics are also shown in the titles. N corresponds to the number of points, Corr is the Pearson correlation, Mean Diff is the mean difference between the CopterSonde and the DL, $\sigma$ is the standard deviation of the differences, and Median Diff is the median difference between the CopterSonde and the DL. . . . .	42
3.2	Similar to Figure 3.1, except for the air temperature (a and b) and dew point temperature (c and d). The 2D histograms of temperature and dew point temperature are binned by $0.5^\circ\text{C}$ . . . . .	43
3.3	Two-dimensional histograms of absolute wind direction difference vs wind speed for the CopterSonde and DL (a), CopterSonde and radiosonde (b), and DL and radiosonde (c). This shows that the lower wind speed measurements have a higher level of uncertainty to the wind direction. Again, the distribution is bi-modal, with LAPSE-RATE observations generally all falling below $5 \text{ m s}^{-1}$ . . . . .	44
3.4	Similar to Figure 3.1, except for comparing wind speed (a) and wind direction (c) from the radiosondes and the CopterSonde. . . . .	45
3.5	Similar to Figure 3.2, except for comparing measurements from the radiosondes and the CopterSonde. . . . .	46
3.6	Similar to Figure 3.1, except for comparing kinematic measurements from the radiosondes and the DL. . . . .	47

3.7	Similar to Figure 3.2, except for comparing thermodynamic measurements from the radiosondes and the AERI. . . . .	48
3.8	Time-height plots of temperature (a) and wind speed (b) from the Moffat site on July 19, 2018. In the top panel, the background is temperature from the AERI retrievals while the points overlaid on top are data from the CopterSonde at approximately 9m resolution. On the bottom, the background is the horizontal wind speed from the DL while the points overlaid on top are data from the CopterSonde at approximately 9-m resolution. The red arrow points to the profile shown in Figure 3.9. . . . .	49
3.9	Profile plots of wind speed (a), wind direction (b), and temperature and dew point temperature (c) from CLAMPS, the CopterSonde, and a radiosonde on July 19, 2018 at 11:33 UTC. The CopterSonde was launched just after the radiosonde, as soon as it was deemed the radiosonde was not in the flight path of the CopterSonde. . . . .	50
3.10	Same as Figure 3.8, except for October 5–6, 2018 during the Flux Capacitor campaign. These time-heights contain data from the entire 24-hour period sampled during Flux Capacitor. The red arrow points to the time of the profile shown in Figure 3.11 . . . . .	51
3.11	Same as Figure 3.9, except for October 6, 2018 at KAEFS during Flux Capacitor. These profiles were from approximately 2:30 UTC. . . . .	52
4.1	Cartoon depicting the coordinate system used to derive the wind speeds using the tilt angle of the CopterSonde. If the wind vane mode is active, the tilt angle $\psi$ is simply the pitch of the aircraft. The unit vectors $\mathbf{e}_v$ and $\mathbf{e}_d$ describe the direction of the relative wind (assumed to be horizontal) and the direction of the gravity force, respectively. . . . .	55

4.2	Two-dimensional histograms of DL-measured wind speed vs CopterSonde measured wind speed (a) using the linear coefficient derived by hovering next to the WASH Mesonet tower. The 2D histogram is binned to $0.5 \text{ m s}^{-1}$ for wind speed. The histogram on the right shows the difference in wind speed between the DL and the CopterSonde(b). The red dotted line in (a) indicates the 1-to-1 line and the black dotted line indicates the least-squares regression. The slope (m) and intercept (b) are shown in the title. Various other statistics are also shown in the titles. N corresponds to the number of points, Corr is the Pearson correlation, Mean Diff is the mean difference between the CopterSonde and the DL, $\sigma$ is the standard deviation of the differences, and Median Diff is the median difference between the CopterSonde and the DL. . . . .	60
4.3	Similar to Figure 4.2, except that the wind speed coefficients were generated using observations from the DL while the CopterSonde was ascending. . . . .	61
4.4	Similar to Figure 4.2, except that the wind speed coefficients were generated using observations from the DL while the CopterSonde was ascending and with the density correction applied. . . . .	62
4.5	Similar to Figure 4.2, except that the wind speed coefficients were calculated using DL observations when the CopterSonde was ascending and with a non-linear fit. . . . .	64

4.6	This figure illustrates the differences between the prior created from the BMX radiosonde archive and the SGP radiosonde archive. Panels A and B show the temperature and water vapor mixing ratio profiles, respectively, for the SGP (red, solid) and BMX (black, solid) priors. The dashed lines denote one standard deviation from the climatology. Panels C and D are the prior temperature correlation matrices for the SGP and BMX prior, respectively, while panels E and F are the prior water vapor mixing ratio correlation matrices. . . . .	66
4.7	Profile of the differences between the SGP retrieval and BMX retrieval for temperature (a) and water vapor mixing ratio (b) values at each retrieved level. The red points show the mean difference while the gray points are the individual differences. The errorbars indicate the standard deviation of the differences. . . . .	68
4.8	Mean difference of potential temperature (A) and water vapor mixing ratio (B) shown in a time–height cross-section comparing the BMX retrieval to SGP retrievals. The mean potential temperature and water vapor mixing ratio from the same period, respectively, are shown in C and D for the BMX retrieval and E and F for the SGP retrievals . . .	69
4.9	Composite temperature profiles from VORTEX-SE during April 2017 at 18Z using the SGP (black) and BMX (red) prior dataset. . . . .	71
4.10	Potential temperatures (black) of all the radiosondes used in the BMX prior (left) and the SGP prior (right). Superadiabatic layers are colored red. . . . .	73
4.11	Histogram of superadiabatic max heights identified in the the SGP prior. The bars are binned every 100 m. . . . .	74
4.12	Histogram of superadiabatic max heights identified in the the BMX prior. The bars are binned every 100 m. . . . .	75

4.13	Similar to Figure 4.8, except comparing the retrievals using with a maximum superadiabatic height of 300 m (C, D) and with a maximum superadiabatic height of 100 m (E, F). . . . .	76
4.14	Profile of the differences between the base BMX retrieval and BMX retrieval with the superadiabatic max height set to 100 m for temperature (a) and water vapor mixing ratio (b) values at each retrieved level. The red points show the mean difference while the gray points are the individual differences. The errorbars indicate the standard deviation of the differences. . . . .	78
4.15	Two-dimensional histograms of AERI-only retrievals vs radiosonde measured temperature (A) and AERI-only retrieval water vapor mixing ratio vs radiosonde measured water vapor mixing ratio (c). The 2D histograms are binned to 0.5 °C for temperature and 0.25 g kg <sup>-1</sup> water vapor mixing ratio. The histograms on the right show the difference in temperature (B) and water vapor mixing ratio (D). The red dotted line is the 1-to-1 line and the black line is the least-squares regression. The slope (m) and intercept (b) are shown in the title. Various other statistics are also shown in the titles. N corresponds to the number of points, Corr is the Pearson correlation, mean diff is the mean difference between the AERI-only and the radiosonde, $\sigma$ is the standard deviation of the differences, and median diff is the median difference between the radiosonde and the retrieval. . . . .	80
4.16	Similar to Figure 4.15, except for MWRonly temperature (A, B) and water vapor mixing ratio (C, D) retrievals. . . . .	81
4.17	Similar to Figure 4.15, except for AERI+UAS temperature (A, B) and water vapor mixing ratio (C, D) retrievals. . . . .	83

4.18	Similar to Figure 4.15, except for MWR+UAS temperature (A, B) and water vapor mixing ratio (C, D) retrievals. . . . .	84
4.19	Posterior, level-to-level correlation matrices for temperature (A, C) and water vapor mixing ratio (B, D) a representative retrieval from LAPSE-RATE. The AERIonly retrievals are located on top, while the AERI+UAS are below. . . . .	86
4.20	Temperature (A) and water vapor mixing ratio (B) uncertainty from a representative retrieval from LAPSE-RATE as a function of height. The AERIonly retrievals are denoted by solid lines, while the AERI+UAS lines are denoted by the dashed lines. . . . .	87
4.21	Similar to Figure 4.21, except showing showing MWRonly (top) and MWR+UAS (bottom) retrievals. . . . .	89
4.22	Similar to Figure 4.22, except showing showing MWRonly (solid line) and MWR+UAS (dashed line). . . . .	90
5.1	Example profile of temperature (red) and dew point temperature (blue) from each observation platform (a) and a time height cross section of vertical velocity measured from the CLAMPS DL from the same time period (b). The gray areas in (b) indicate the DL was not in vertical stare mode and was performing PPI scans. . . . .	95
5.2	Same as Figure 1.2, only with horizontal wind speed contoured instead of the temperature. . . . .	96



## Abstract

In recent years, increased attention has turned to studying the atmospheric boundary layer (ABL) as new observing systems have been developed. Traditionally, the ABL has been drastically under-sampled by conventional observing systems (e.g., radiosonde and meteorological towers). Filling this so-called “ABL data gap” using new, high-resolution observing systems has the potential to assist with the development of next-generation parameterization schemes for scales ranging from large-eddy simulation to climate scales, improve forecaster situational awareness during high-impact weather, and provide detailed information for assimilation into numerical weather prediction. Specifically, commercial availability of ground-based remote sensors and the recent widespread availability of small uncrewed aerial systems (UAS) has opened up a world of opportunity to observe and study the complex processes that occur in the ABL which have previously not been routinely observed.

However, it is important to evaluate the utility of each system by directly comparing them with one another in a variety of environments. In the following studies, thermodynamic and kinematic data from a suite of remote sensors contained in the Collaborative Lower Atmospheric Mobile Profiling System (CLAMPS) and state-of-the-art weather-sensing UAS (WxUAS) are compared to one another. CLAMPS contains an Atmospheric Emitted Radiance Interferometer (AERI) and a microwave radiometer (MWR) for thermodynamic profiling and a scanning Doppler wind lidar (DL) for kinematic profiling. The WxUAS used is the CopterSonde, which has been developed specifically to provide accurate kinematic and thermodynamic measurements. Data from two campaigns, one which took place in the San Luis Valley in Colorado and the other at the Kessler Atmospheric and Ecological Field Station in central Oklahoma, are used for the comparison.

From these intercomparisons, multiple instrument deficiencies are examined. Compared to both the DL and high-resolution radiosondes, the CopterSonde tended

to underestimate the wind speed using an empirically derived function that relates the tilt of the UAS to the wind speed. Utilizing the DL retrieved wind profiles, a new function is proposed and validated. Additionally, issues are identified with thermodynamic retrievals performed in locations where appropriate prior information is unavailable. A modified thermodynamic retrieval, the Tropospheric Remotely Observed Profiling via Optimal Estimation (TROPOe) algorithm, is used to combine multiple observation types to attempt to improve the retrievals. Additionally, data collected from the Verification of the Origins of Rotation in Tornadoes Experiment Southeast (VORTEX-SE) are used to examine sensitivities in TROPOe.

Throughout the analyses, synergies are present between the remote sensing and UAS. These synergies are discussed in the context of next generation profiling networks to fill the ABL data gap and suggestions are made for how a next generation network could function with remote-sensing and WxUAS.

# Chapter 1

## Introduction

The atmospheric boundary layer (ABL) is often regarded as the most important layer of the atmosphere; the processes that occur in the ABL are vital to human life, ecosystem health, and sustainability. After all, this is the layer of the atmosphere that humans interact with on a daily basis (unless one is lucky enough to be an astronaut). Despite our proximity to the processes in the boundary layer, the ABL is also known as one of the most difficult areas of study in the atmospheric sciences. Much of the difficulty stems from the role of turbulence, one of the unsolved problems of classical physics, in the exchange of momentum, heat, and mass. Additionally, the complexity of terrestrial and marine surface-atmosphere interactions (in addition to biosphere-atmosphere interactions) adds another layer of complexity to ABL processes.

The depth and structure of the ABL is highly variable in time and space. However, a conceptual model can be created that illustrates the diurnal variations of the ABL as the sun heats the land surface during the day and as the surface cools overnight (Stull 1988). Figure 1.1 shows how the ABL structure changes in a mean sense over a 24-hour period.

As the sun rises, it heats the surface, and the air immediately adjacent to the surface begins to warm, creating a shallow mixed layer (Figure 1.1B). This mixed layer continues to grow as the surface continues to be heated and thermal plumes penetrate higher into the atmosphere (Figure 1.1C). Eventually, a steady state is reached (Figure 1.1D) and there is a well-mixed ABL that typically extends from 1–3 km above the surface, the free atmosphere above the ABL, and a small zone between the mixed layer and the free atmosphere called the entrainment zone (where the free atmosphere can be entrained into the ABL). Within the ABL, there is a less

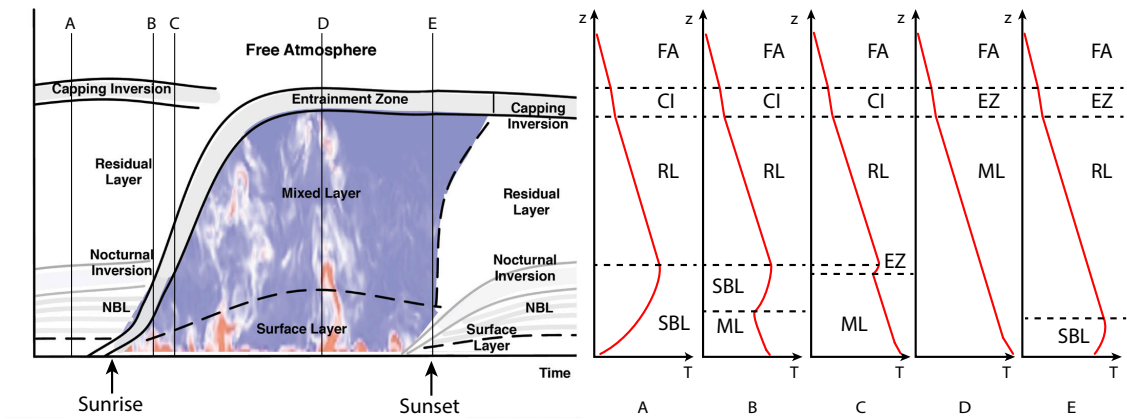


Figure 1.1: A conceptual model of the ABL based on Stull (1988). The left panel shows a time-height figure of how the boundary layer grows throughout the diurnal cycle. Theoretical mean temperature profiles from throughout the diurnal cycle are shown on the right and correspond with the vertical lines on the left. The free atmosphere (FA), capping inversion (CI), entrainment zone (EZ), residual layer (RL), mixed layer (ML), and stable boundary layer (SBL) are labeled.

pronounced layer right at the surface called the surface layer. The surface layer is traditionally defined as a layer where turbulent fluxes are approximately constant with height (Stull 1988) and is typically estimated to be approximately 10% of the total boundary-layer height. This is also the layer where the atmosphere can sometimes be described by empirically derived, universal logarithmic functions, such as those described by Monin–Obukhov Similarity Theory (MOST, Monin and Obukhov 1959). Scaling down even further, above homogeneous surfaces, there is the roughness sublayer. This layer is described as the layer where individual roughness elements (e.g., buildings, trees) create horizontal variability. The roughness sublayer also deviates from the universal function of MOST. Since the daytime ABL growth is determined by the strength of thermal eddies, the surface latent and sensible heat fluxes (and their partitioning) play a large role in modulating the ABL depth

When the sun sets, the turbulent mixing abruptly ceases and the surface begins to cool (Figure 1.1E). During the overnight hours, the air nearest the surface is colder than the air above it (due to radiative cooling of the surface) creating a stably stratified layer near the surface which is the nocturnal boundary layer (NBL; Figure 1.1B). Above this stable layer, the mixed layer from the daylight hours remains, though there are no buoyant plumes present. In this so-called residual layer, any turbulence is generally weak and intermittent, unless it is induced by shear (e.g., from the nocturnal LLJ). The surface continues to cool through the night and when the sun rises, the cycle repeats.

While this conceptual model is useful to understand the typical processes that underlay the ABL structure, deviations from this are incredibly common both temporally and spatially. For example, the boundary layers on both sides of a dryline (a boundary separating a relatively dry, hot airmass and a relatively cool, moist airmass) exhibit the typical characteristics of a classical convective boundary layer (i.e., well mixed with inversion at the top of the boundary layer), but are drastically different

thermodynamically due to the stark differences in boundary layer moisture. Dew-point temperature gradients up to  $10 \text{ K km}^{-1}$  have been observed (e.g., Ziegler and Hane 1993; Ziegler and Rasmussen 1998; Schultz et al. 2007). The relatively higher sensible heat fluxes on the dry side of the dryline cause the boundary layer to grow quicker, whereas the combination of latent heat flux and sensible heat flux on the moist side can cause relatively slower boundary layer growth. This means stronger momentum from aloft can mix down on the dry side of the dryline sooner than the moist side, which causes moisture convergence along the boundary.

This convergence means that drylines also have the capability to initiate convection (Rhea 1966; Schaefer 1974a,b; Parsons et al. 1991; Hane et al. 1993). CI modifies the convective boundary layer, further deviating it from the conceptual model shown in Figure 1.1. In turn, the boundary layer structure can have an impact on convection (Crook 1996). Deviations from the conceptual model are not only relegated to the convective boundary layer. The spatio-temporal evolution of the nocturnal LLJ can impact how the nocturnal ABL develops. Intermittent turbulent mixing, modifications to the thermodynamic structure, and CI have been found to be a result of the spatial heterogeneity nocturnal LLJ (Gebauer et al. 2018; Smith et al. 2019).

The ABL structure can also have an impact on sectors vital to preserving human life and property. Low-level inversions can impact the application of herbicides in the agricultural sector (Fiebrich et al. 2021). Improved forecasts and/or observations of these low-level inversions would minimize herbicide drift, preventing unnecessary crop loss. Additionally, the ABL structure drives how wildfires propagate and how smoke disperses (San-Miguel-Ayanz et al. 2003). Wildfires also have an impact on the boundary-layer structure, which creates complex feedbacks that are relatively poorly observed with current models and technologies (Liu et al. 2019). Along the same line, air quality forecasts would benefit from better observations and modeling of the ABL (World Health Organization 2016).

Improving numerical weather prediction is an often-cited benefit to increased ABL observation. The next section reviews some current limitations of ABL modeling and parameterization to frame how improved observations could be used.

## 1.1 Model Deficiencies

Improving the physics in atmospheric models, ranging from large-eddy simulation (LES) to climate-scale modeling, is often a primary motivation for improving the quality and number of atmospheric observations (National Research Council 2009; Hoff et al. 2012). Many of the assumptions and parameterizations used in numerical weather prediction are based on decades-old datasets collected with eddy-covariance towers (e.g., Businger et al. 1971). These parameterizations are necessary due to the large range of turbulent scales in the atmosphere; in other words, with current computing power, not all scales and processes can be explicitly represented in the model.

For example, forecasting convection initiation (CI) remains a challenge due to its inherent sensitivity to small changes in temperature and moisture (Hane et al. 1997; Weckwerth and Parsons 2006). Crook (1996) examined the sensitivity of CI to various boundary layer variables. In this study, CI was most sensitive to small scale differences of surface temperature and moisture. Fluctuations of temperature and mixing ratio as small as  $1\text{ }^{\circ}\text{C}$  and  $1\text{ g kg}^{-1}$ , respectively, were the difference between having CI with robust storms and having no CI whatsoever. Fabry (2006) used a variety of measurement platforms to find that on meso- and synoptic-scales, CI was most sensitive to fluctuations in temperature. However, at smaller scales, CI was sensitive to individual updraft strength. The updraft strength, in turn, affects the small scale fluctuations of temperature and moisture.

Forecasts of CI are often a popular reason to improve parameterizations, and will be a common point of discussion in the remainder of this section, but there are many

other areas where improved parameterization schemes would be beneficial. Often, ABL parameterization development is oriented toward improving the representation of specific processes. In addition to CI, wind energy forecasts will greatly benefit from improved parameterizations. A one-percent error in wind speed could result in billions in revenue lost by wind energy companies over a year (Banta et al. 2013). Recent campaigns like the Perdigão campaign (Fernando et al. 2019) and the upcoming American Wake Experiment (AWAKEN) aim to improve model parameterizations for wind energy applications. Additionally, wind farms can have an impact on the environment, so quantifying their effect on atmospheric flow and composition is an important area of study (e.g., Olson et al. 2019; Tomaszewski and Lundquist 2021). ABL characteristics like wind speed, the strength of mixing, and the ABL depth help modulate the transport of atmospheric constituents, both vertically and horizontally. It is well known that improved parameterizations of the exchanges between the ABL and the free troposphere will help improve pollution dispersion models (e.g. Angevine et al. 2014). Aerosols mixed into the ABL from the free troposphere can interact with solar radiation and cause adverse affects on air quality (Petäjä et al. 2016). Additionally, improving parameterizations of emissions that impact the air quality from ground-based sources is important for dispersion modeling.

Most popular general purpose ABL parameterization schemes relate turbulent fluxes of temperature, moisture, and momentum to the mean vertical gradient:

$$\overline{(w'\phi')} = -K_\phi \frac{\partial \bar{\phi}}{\partial z} \quad (1.1)$$

where  $w$  is the vertical velocity,  $\phi$  is the quantity (temperature, moisture, or momentum), and  $K_\phi$  is the eddy diffusivity, which is determined by the ABL scheme. The overbar notes the grid-observable mean state while the primes indicate a turbulent perturbation. This first order approximation is an analogy to molecular diffusion where a quantity is transferred down-gradient, in other words, from regions



of relatively high temperature/moisture/momentum to regions with relatively low temperature/moisture/momentum (Stull 1988; Arya 2001).

Some parameterization schemes determine  $K_\phi$  using the local kinetic energy, the specified mixing length, and specified dimensionless stability functions (e.g., MOST). These are often referred to as local parameterization schemes since they only use information at adjacent levels to determine the unknown quantities. Common schemes that use this approach are the Mellor–Yamada–Janjic (MYJ; Janjić 1994) and the Mellor–Yamada–Nakanishi–Niino (MYNN; Nakanishi and Niino 2004). These relatively simple schemes produce mixed results. For example, the MYJ scheme tends to produce ABLs that are too cool and moist due to a lack of robust mixing while the MYNN scheme performs relatively well when compared to radiosondes in the Great Plains (Hu et al. 2010; Coniglio et al. 2013).

Other parameterization schemes attempt to simulate the effects of large eddies and coherent structures in the ABL by using multiple levels to determine the eddy diffusivity. These non-local schemes are thought to improve upon local schemes by better representing mixing in the boundary layer by introducing a non-local gradient term to the eddy diffusivity (Coniglio et al. 2013). One important aspect of non-local schemes is the determination of ABL height, since this limits the size of the largest scale eddies (Helbig et al. 2021). These large-scale ABL motions have been shown to modulate near-surface turbulent processes (Salesky and Anderson 2018, 2020).

Despite continued improvements to ABL parameterization schemes in experimental and operational models, some processes are still not well represented. For example, the role of subgrid orography still proves to be a challenge (e.g., Steeneveld et al. 2008). Many parameterizations use strict assumptions to simplify the surface similarity relationships that are not valid for areas with complex terrain. For example, on steep slopes in complex terrain, it may be necessary to use 3D surface fluxes (Olson et al. 2019) or reformulate the surface similarity relationships to account for

anisotropic turbulence (Stiperski et al. 2019, 2021). Additionally, questions remain about how the horizontal heterogeneity of surface characteristics impact ABL mixing and near-surface fluxes (Olson et al. 2019) and how to best represent processes that occur during the morning and evening transition periods (Angevine et al. 2020; Helbig et al. 2021).

Another issue with ABL parameterization schemes is they are often built for forecast applications at particular grid spacing, which causes issues when changing to a different model configuration (Olson et al. 2019). Also, as computing power increases, grid spacing continues to decrease in operational mesoscale models. They are quickly approaching scales that begin to blur the lines between LES and traditional NWP, while not satisfying the underlying assumptions of either method of atmospheric simulation. This is known as *terra incognita* (Wyngaard 2004). At these grid resolutions, the dominant length scale of ABL turbulence is comparable to the scale of the resolved flow.

At these scales, between traditional LES scales of  $O(10\text{ m})$  to mesoscales of  $O(1 - 10\text{ km})$ , new parameterization schemes will need to be adaptive to grid size in order to account for the differing amount of subgrid-scale turbulence versus the explicitly resolved eddies (Wyngaard 2004; Honnert et al. 2020). Thus, so-called “scale-aware” parameterizations have been an active area of research in recent years (e.g., Shin and Dudhia 2016; Zhou et al. 2018; Chow et al. 2019; Zhou et al. 2021). Most of these have been developed under relatively idealized conditions and need to be tested and evaluated on more complicated case studies (Honnert et al. 2020).

Observations in the ABL will be a key component to improving parameterization schemes in the future. However, more advanced observations are likely required to make appreciable progress. High temporal resolution observations of the ABL depth are necessary to improve its parameterizations. This alone can have noticeable

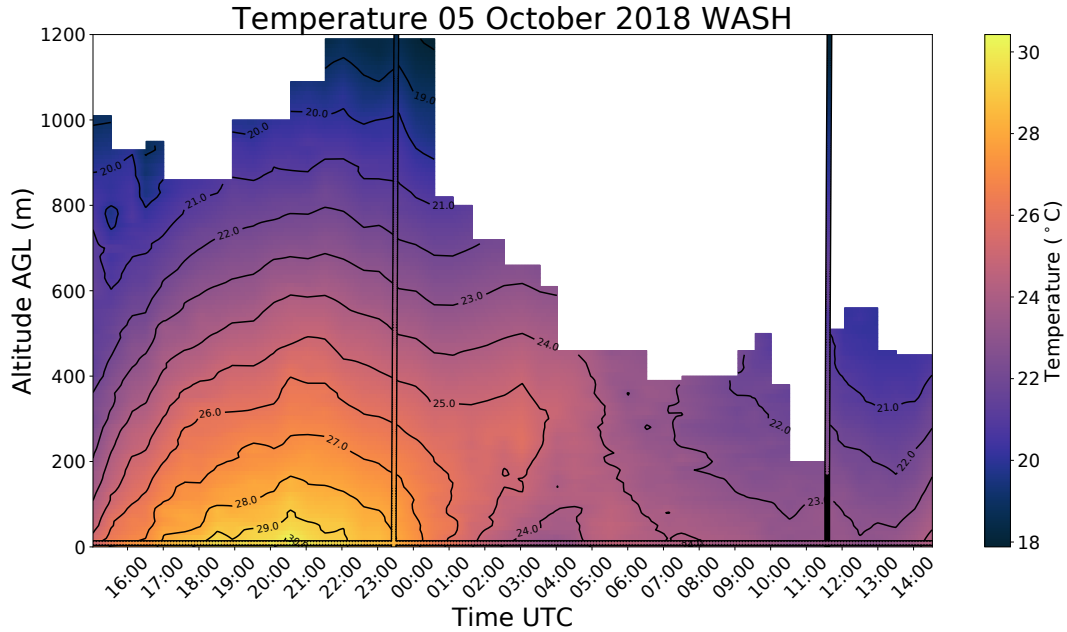


Figure 1.2: A 24-hour time-height cross section of temperature data collected by the CopterSonde during Flux Capacitor. Also shown are two radiosondes (two vertical lines with color fill) and 10 m Washington, OK Mesonet temperature measurements. Note the amount and fidelity of the CopterSonde data compared to the operational observations. During the overnight period, the nocturnal LLJ was too strong to fly the CopterSonde over 400 m.

impacts on the parameterizations of other processes (e.g., surface-atmosphere interaction, budgets of CO<sub>2</sub> and other constituents, and turbulent mixing; Helbig et al. 2021). Additionally, improvements to non-local parameterizations require more frequent measurements of the turbulent processes throughout the depth of the ABL, not only at relatively few points near the surface. Historically, few ABL observations are available in the region extending above typical meteorological towers, but new instrument technologies show promise of filling this observational gap.

## 1.2 The Observational Data Gap

By combining traditional surface flux measurements with new ABL observation platforms, many of the assumptions made in ABL parameterizations can now be revisited with additional context. Unfortunately, routine thermodynamic and kinematic observations throughout the ABL depth are sparse (National Research Council 2009; Hoff et al. 2012; Helbig et al. 2021). In recent decades, many parts of the country have invested in relatively dense networks of meteorological towers to measure atmospheric phenomena on the mesoscale (10s to 100s of km in size; Brock et al. 1995; Schroeder et al. 2005; McPherson et al. 2007). However, these measurements are typically only in the lowest 10 m of the atmosphere.

In a given day, typically there are two complete profiles of the ABL via radiosondes launched by the National Weather Service (NWS). However, the profiling locations are hundreds of miles apart and the boundary layer changes on much shorter time scales than what is captured by these NWS radiosondes, which are launched at 00Z and 12Z daily (Durre et al. 2006). Commercial aircraft can collect temperature and pressure data via the Aircraft Meteorological Data Relay (AMDAR). However, measurements of moisture from AMDAR are not common. Additionally, AMDAR measurements are relegated to large commercial airports and are less available during the nighttime hours due to airport closures (Zhang et al. 2019).

By combining traditional eddy covariance observations with new, high-resolution boundary-layer profiles in a relatively dense network, new insights to atmospheric physics, and thus better parameterizations, are possible. For example, ABL height was not included as a parameter in the initial scaling laws but is an important length scale since it determines the size of the largest scale eddies. Ground-based remote sensors are well suited to detect the boundary-layer height and, combined with surface flux measurements, have the potential to assist in determining the relationship between surface fluxes and the remainder of the ABL thermodynamic and kinematic

characteristic (Helbig et al. 2021). With more advanced remote sensors, it is possible to calculate sensible and latent heat flux even without surface stations (e.g., Behrendt et al. 2020).

In addition to improving fundamental understanding of atmospheric processes, ABL profiling systems also can improve model forecasts by reducing errors in the background analysis through data assimilation (Romine et al. 2013). Coniglio et al. (2019) was the first study to assimilate observations from ground-based remote profilers into high-resolution convection-allowing models and determine the impact of these observations on convection resolving models' short-term forecasts of CI. This study found that even assimilating only one system provides improvements to the prediction of CI and early storm improvements. While Coniglio et al. (2019) focused on the improvements of a single targeted system, studies from the Plains Elevated Convection at Night (PECAN; Geerts et al. 2017) campaign show that a network of boundary-layer profilers exhibit great promise in improving short-term forecasts (Hu et al. 2019; Degelia et al. 2019; Chipilski et al. 2020). Koch et al. (2018) examined the value of weather-sensing uncrewed aerial systems (WxUAS) in the pre-convective boundary layer during the Environmental Profiling and Initiation of Convection (EPIC) campaign in northern Oklahoma. While the WxUAS were effectively able to observe the rapid environmental changes leading to CI, they concluded that it could be difficult for forecasters to ingest the data in real time. They suggested that the real value in profiling WxUAS may be as a network designed for assimilation into NWP models. However, more work is needed to truly quantify the impact of boundary layer profilers on models.

It is apparent that a single ABL profiling system is not likely to be a one-size-fits-all approach to filling the ABL data gap. The 2009 NRC report highlighted this by discussing that it will likely take a “network of networks” to effectively fill this gap. Some state mesonets are beginning to experiment with adding profilers. The

New York Mesonet (Brotzge et al. 2020) and West Texas Mesonet (Schroeder et al. 2005) have augmented their existing network with ground-based remote sensors. It will take numerous types of instrumentation working in sync to provide information at the resolution necessary to improve basic understanding of the atmosphere and for the purposes of assimilation into NWP. However, relatively little research has been done to determine which combinations of instruments are best in which scenarios. As more systems come to market, careful consideration will be required to optimize ABL profiling.

### **1.3 Possible Data Gap Solutions**

After the 2009 NRC report was published, multiple workshops were held and accompanying reports were published to begin the process of identifying possible technologies to fill the data gap (Hoff et al. 2012). Initially, the technologies identified were primarily ground-based remote systems such as lidars, microwave radiometers (MWRs), and infrared interferometers such as the Atmospheric Emitted Radiance Interferometer (AERI). However, in more recent years, WxUAS have reached a level of maturity that shows promise for collecting high-resolution, parcel-scale observations. The sections that follow will describe the systems examined herein and the main advantages and limitations of each.

#### **1.3.1 Ground-Based Remote Sensors**

Ground-based remote sensors have the advantage of being mechanically simple and robust. Due to this, the amount of maintenance required for remote sensors is fairly minimal, aside from the occasional need for calibration. However, they do not directly measure the quantities researchers are interested in (e.g., temperature, moisture, wind speed). These variables must be obtained through a retrieval process, which can introduce error and uncertainty to the desired measurement.

The remote sensors used for the studies herein are all part of the Collaborative Lower Atmospheric Mobile Profiling System (CLAMPS). CLAMPS currently consists of 3 instruments: a Halo Photonics Streamline scanning Doppler lidar (DL; Pearson et al. 2009), an Atmospheric Emitted Radiance Interferometer (AERI; Knuteson et al. 2004a,b), and a version 4 Humidity and Temperature Profiling Microwave Radiometer (HATPRO MWR; Rose et al. 2005). As part of the HATPRO MWR, a Vaisala WXT-530 weather station mounted approximately 3 m above ground level is also included. These instruments are housed in a heavily modified off-the-shelf trailer for portability. The AERI and MWR are combined into a physics-based retrieval to derive thermodynamic profiles (Turner and Löhnert 2014; Turner and Blumberg 2019).

While the Doppler lidar, AERI, and MWR in CLAMPS will be the primary instrumentation examined in the following studies, there are numerous other remote sensors that could help augment the current observation network. The Atmospheric Sounder Spectrometer by Infrared Spectral Technology II (ASSIST-II) takes the same measurements as the AERI, but is a relative newcomer to the market and needs evaluation. Despite taking high-resolution spectra, infrared spectrometer like the AERI and ASSIST-II are still not ideal for measuring water vapor. Thus, other instruments also need to be evaluated. There are multiple instruments, most of which are still research oriented and non-commercialized, that can assist with water vapor measurements. Water Vapor Differential Absorption Lidars (WVDIALs) are one example. Currently, the National Center for Atmospheric Research (NCAR) is testing multiple WVDIALs. Additionally, Vaisala is nearing completion of a commercial WVDIAL. Both have shown promise in providing high-resolution water vapor profiles in the boundary layer (Smith et al. 2021). Another system on the horizon is the Purple Pulse Raman lidar (Lange et al. 2019). Raman lidars can also provide high resolution temperature and humidity profiles. Since they are an active remote sensor, they look

promising in quantifying moisture entrainment at the top of the ABL (Lange et al. 2019; Smith et al. 2021).

### 1.3.1.1 Doppler Lidars

Doppler lidars have been used for a wide range of studies related to the ABL. They are useful for wind energy meteorology (Banta et al. 2013, 2015; Newman et al. 2016; Mann et al. 2017; Choukulkar et al. 2017; Barthelmie et al. 2018; Wildmann et al. 2018; Fernando et al. 2019), classical boundary-layer meteorology (Gal-Chen et al. 1992; Calhoun et al. 2006; Klein et al. 2015; Bonin et al. 2017; Bodini et al. 2018; Kral et al. 2018; Smith et al. 2019), and more recently, near-storm measurements (Laser 2020).

The Halo Photonics Streamline DL in CLAMPS operates with a 1.5  $\mu\text{m}$  wavelength and scatters off of aerosols and particulates in the ABL (Pearson et al. 2009). Doppler lidars use pulses of light to measure the radial wind velocity along the beam by detecting the Doppler shift of backscattered light (Werner 2005). In essence, DLs are the optical analog of Doppler radar systems. The more common Doppler wind lidars used today are generally pulsed heterodyne systems. In a pulsed heterodyne system, the return signal from each pulse is mixed with a local oscillator. This signal oscillates at the difference between the local oscillator and the return signal, which gives the Doppler shift (Werner 2005). This Doppler shift is then used to calculate wind velocity along the lidar beam, or the radial velocity.

Scanning DLs, like the Halo, are able to direct the laser beam in any direction. Due to this, a number of scanning strategies are possible depending on the flow of interest. Vertical wind speeds can be directly measured by simply pointing the DL laser to zenith. Other strategies can be used to provide information about the horizontal winds if assumptions are applied to the flow. For example, a velocity azimuth display (VAD) can be calculated from a plan position indicator (PPI) scan to



provide the horizontal wind speed and direction (Browning and Wexler 1968). A PPI scan has a fixed elevation but changing azimuth, providing a spatial representation of the velocities around the DL. To calculate the VAD, one must assume that the flow in the PPI scan is homogeneous. While this is often the case, especially in the nocturnal boundary layer, complex terrain and highly convective days can result in violations to this assumption and cause erroneous measurements. VADs are calculated from the PPI scans using a least-squares fitting of the radial velocity as a function of azimuth to the radial velocity equation:

$$V_r(\theta) = u \sin \theta \cos \phi + v \cos \theta \cos \phi + w \sin \phi \quad (1.2)$$

where  $\phi$  is the elevation,  $\theta$  is the azimuth, and  $u$  (east–west),  $v$  (north–south), and  $w$  (vertical) are the wind components in the traditional meteorological sense. One of the advantages of the VAD technique is the goodness-of-fit can be used to determine how well the retrieval performs and thus give some uncertainty to the observation.

Though they will not be explored here, there are many other DL scanning techniques that can be used to infer information about the atmosphere. Range-height indicator (RHI) scans, where the DL azimuth is fixed and the elevation is changed, can show flow heterogeneity over larger areas. If two or more DLs are present and have overlapping or intersecting RHI scans, virtual towers of wind speed and direction can be calculated at those points (Calhoun et al. 2006; Hill et al. 2010; Bell et al. 2018, submitted). In addition, more specialized scans can be used to estimate turbulent quantities. Sathe and Mann (2013) provides an extensive review of methods to estimate quantities from a scanning DL such as turbulence kinetic energy, turbulence length scales, and vertical velocity variance, to name a few.

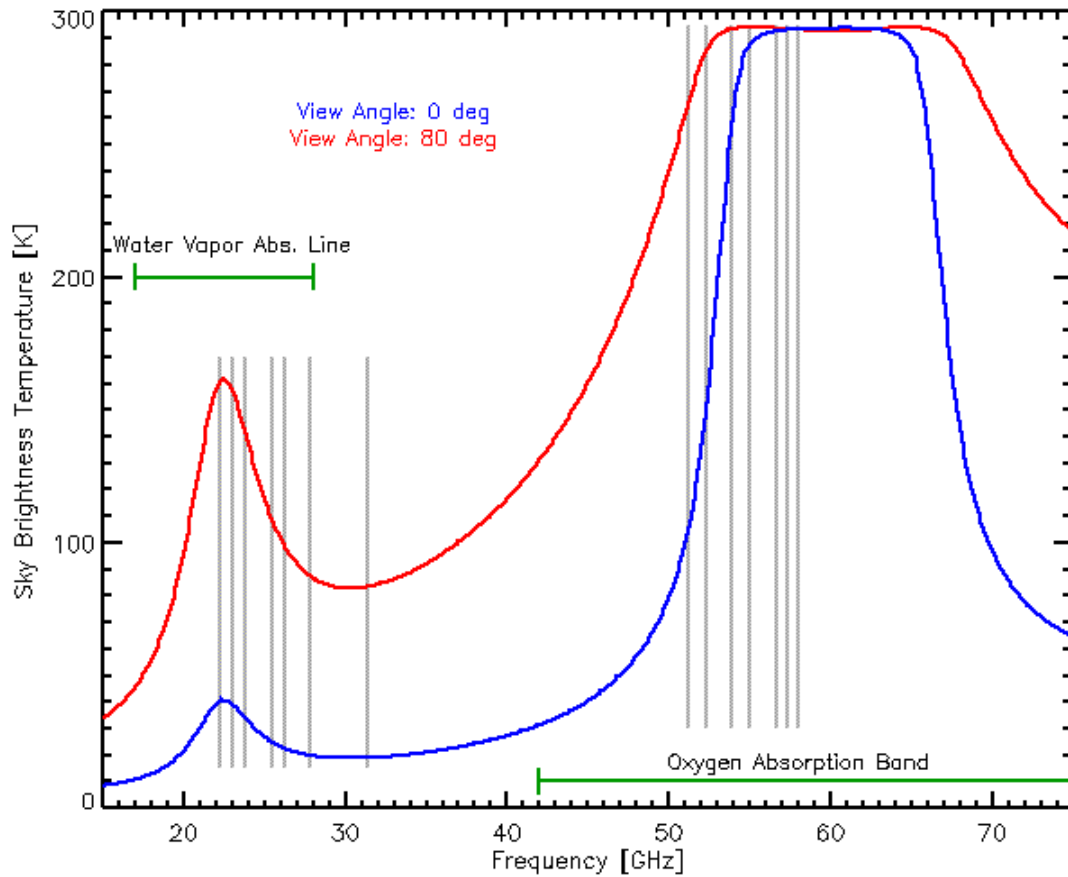


Figure 1.3: Theoretical brightness temperatures calculated for the standard atmosphere at a  $0^\circ$  (zenith) viewing angle (blue line) and an  $80^\circ$  (off-zenith) viewing angle (red). Vertical gray lines indicate the frequencies measured on the HATPRO Version 4 in CLAMPS1. (Figure courtesy of Dave Turner, NOAA Global Systems Laboratory)

### 1.3.1.2 Microwave Radiometers

Microwave radiometers (MWRs) measure downwelling radiation emitted from the atmosphere in the microwave spectrum. The HATPRO MWR used in CLAMPS measures radiation in 14 channels with 1 s temporal resolution (Rose et al. 2005). There are 7 channels in the K-band (22.2 to 31.4 GHz) and 7 in the V-band (51.8 to 58.8 GHz). The K-band channels are located in a water vapor absorption line and are used for deriving column-integrated water vapor (Figure 1.3). Additionally, there is some limited information on the water vapor profile. The V-band channels are used for deriving temperature profiles (Liljegren et al. 2001; Löhnert and Maier 2012; Blumberg et al. 2015a).

Typically, MWRs measure downwelling radiation from zenith. However, off-zenith scans may be used to gather more information on the ABL temperature profile (again, this assumes the ABL is pseudo-homogeneous). In order to minimize the effects of heterogeneities (such as cloud contributions that are not present at zenith), the most opaque V-band channels are used in retrievals.

In order to accurately retrieve the atmospheric temperature and humidity profiles, the MWR needs to be well calibrated. MWRs contain an internal blackbody at ambient temperature that is periodically viewed to calibrate the gain of the instrument, however this is only a relative calibration. Though there are a couple different techniques that can be used for absolute calibration (see Yong Han and Westwater 2000 for details on the tip-calibration method), the CLAMPS MWR typically uses liquid nitrogen to get an absolute calibration by alternating views between the internal blackbody and the liquid nitrogen target. However, this method must be completed manually. Many times this will fail to get the calibration better than 1 K in total error (Maschwitz et al. 2013) and additional bias correction is often needed (Blumberg et al. 2015a).

Classically, the temperature and humidity profiles are derived from the brightness temperatures using either multi-variable linear regression or artificial neural network retrievals. These statistics-based retrievals are developed on long-term radiosonde and/or model datasets and are tailored for the particular location where the MWR will be deployed (Rose et al. 2005). The retrievals are relatively simple to produce and are computationally efficient, which is advantageous for high-temporal resolution observations like those from the HATPRO system. However, statistical retrievals have multiple disadvantages for meteorological research applications. Since they are trained on data for a particular location, the retrievals are only good for the conditions observed in the long-term training dataset (Rose et al. 2005). Thus, statistical retrievals often perform best in “typical” conditions and are less accurate at the extremes of the distribution where researchers are often seeking observations. Additionally, due to the required training dataset being for a specific location, statistical retrievals are not suited for mobile deployments of MWRs (e.g., with systems like CLAMPS).

Fortunately, other methods of retrieval are available. Physics-based retrievals solve many of the issues with statistical retrievals, but they come at the cost of being computationally inefficient due to the need of a radiative transfer model to simulate the physics of the atmosphere. One specific physical retrieval is described in Section 1.3.1.4.

### **1.3.1.3 Infrared Spectrometers**

Ground-based infrared spectrometers such as the AERI (Knuteson et al. 2004a,b) and the ASSIST-II (Rochette et al. 2009) measure downwelling radiation from the atmosphere in the infrared spectrum. For this paper, we will only use data collected by an AERI, though the same principals can be applied to the ASSIST-II.

The AERI measures downwelling radiance emitted by the atmosphere from wavelengths (wavenumbers)  $3.3 \mu\text{m}$  ( $3020 \text{ cm}^{-1}$ ) to  $19 \mu\text{m}$  ( $400 \text{ cm}^{-1}$ ) at  $1 \text{ cm}^{-1}$  resolution with a temporal resolution of approximately 20 s (Turner and Blumberg 2019). This portion of the infrared spectrum contains absorption lines from methane ( $\text{CH}_4$ ), ozone ( $\text{O}_3$ ), carbon dioxide ( $\text{CO}_2$ ), and water vapor ( $\text{H}_2\text{O}$ ). The AERI self calibrates using two National Institute of Standards and Technology (NIST) traceable blackbodies, with one blackbody being heated to a constant temperature and the other at ambient temperature. These blackbodies combined with non-linearity corrections for the detectors allow a high radiometric accuracy of better than 1% (Knuteson et al. 2004b). By carefully selecting absorption bands that do not overlap with other gasses in different parts of the spectrum, temperature, water vapor mixing ratio, and some cloud properties can be retrieved from observed AERI radiance spectra. One such retrieval is described in Section 1.3.1.4.

While at full spectral resolution, the AERI can take measurements in over 5000 channels, not all of these are used in the retrievals. Typically, only channels that do not overlap with multiple gasses are used. Additionally, only regions where the spectroscopy is well established are used. Channels between  $538 \text{ cm}^{-1}$  and  $588 \text{ cm}^{-1}$  are used for water vapor retrievals and various windows between  $612 \text{ cm}^{-1}$  and  $722 \text{ cm}^{-1}$  are used for temperature information. Windows between  $828 \text{ cm}^{-1}$  to  $905 \text{ cm}^{-1}$  are primarily sensitive to clouds and are used to retrieve cloud properties.

#### 1.3.1.4 TROPoe

The observations from AERIs and MWRs have been used for years to derive thermodynamic profiles of the atmospheric state. For the remainder of the studies herein, an iterative optimal-estimation algorithm based on Rodgers (2000) will be used to invert the radiance and brightness temperature observations into temperature and moisture profiles. This optimal-estimation method uses a forward model  $F$  to relate

the atmospheric state  $\mathbf{X}$  to the observations  $\mathbf{Y}$ . Through multiple iterations, the algorithm adjusts the state vector based on the differences between the forward calculation  $F(\mathbf{X})$  and  $\mathbf{Y}$  until a convergence criteria has been met. Since the inversion is an ill-posed problem, multiple solutions can satisfy the observations, thus an a priori (the “prior”) dataset is needed to constrain the retrieval. This consists of a reasonably long climatology of temperature and moisture profiles.  $\mathbf{X}_a$  and  $\mathbf{S}_a$  represents the prior profile and the prior covariance matrix, respectively. Since the microwave and infrared radiative transfer models used for the forward model are highly non-linear, the Jacobian of the forward model  $\mathbf{K}$  needs to be calculated for each iteration,  $n$ , of the algorithm. The equation used is:

$$\mathbf{X}^{n+1} = \mathbf{X}_a + (\gamma \mathbf{S}_a^{-1} + \mathbf{K}_n^T \mathbf{S}_e^{-1} \mathbf{K}_n)^{-1} \mathbf{K}_n^T \mathbf{S}_e^{-1} [\mathbf{Y} - F(\mathbf{X}^n) + \mathbf{K}_n(\mathbf{X}^n - \mathbf{X}_a)] \quad (1.3)$$

where  $\mathbf{S}_e$  is observation covariance matrix, the superscripts -1 and T are the matrix inverse and transpose, and  $\gamma$  is a factor used to constrain the retrieval in early iterations.

The forward model used for the AERI spectra is the Line-by-Line Radiative Transfer Model (LBLRTM) Version 12.1 while MonoRTM Version 5.0 is used for MWR observations. In addition to the spectra collected by the MWR and AERI, outside observations can be added to  $Y$  as long as there is an appropriate forward model to convert from observation space to state space. For example, numerical weather prediction forecasts are often used in the upper levels to constrain the retrieval where there is minimal information content. In this case, the forward model is simply interpolation of the temperature and moisture fields from the model grid to the TROPoe retrieval grid.

Two different, but equivalent, versions of this algorithm are used for these studies: the AERIOe algorithm (Turner and Löhnert 2014; Turner and Blumberg 2019) and the Tropospheric Remotely Observed Profiling via Optimal Estimation (TROPoe)

algorithm. TROPoe is a Python port of AERIOe, which was originally written in the IDL programming language. TROPoe improves upon AERIOe by using modern software containerization to standardize the retrieval as much as possible.

The motivation behind the uniquely different names of AERIOe and TROPoe is two fold: 1) to make a clear delineation between the IDL version and the Python version and 2) to show that TROPoe is being developed to be more generalized in the types of observations it can ingest into the retrieval. AERIOe was largely focused on using AERI observations as the main component of the retrieval, with other observations being used primarily to constrain the retrieval in areas where the AERI information content is small. TROPoe is being designed to not be AERI-centric and will instead be capable of ingesting many different types of observations, including those from MWRs and other active remote sensors. The goal is to provide a standardized retrieval for thermodynamic profiling to make adoption easier across the research, data assimilation, and forecasting sector.

### **1.3.2 Weather-Sensing Uncrewed Aerial Systems**

In recent years, a new paradigm for atmospheric profiling has emerged. As uncrewed aerial systems (UAS; also referred to as remotely piloted aircraft systems, RPAS) have become more cost effective due to a boom in UAS in the commercial sector, they have become an attractive alternative to ground-based remote sensing. While many of the limitations of ground-based remote sensors are solved with UAS, they do present their own set of challenges. For example, regulatory issues related to the integration of UAS into the National Airspace System (NAS) mean that UAS are currently less utilized for boundary-layer profiling than ground-based remote sensors (Hoff et al. 2012; Koch et al. 2018). However, this situation is changing quickly. The Federal Aviation Administration (FAA) recently released guidelines for UAS to include remote identification on systems by mid- and late-2022 for manufacturers and

operators, respectively. This will pave the way for flights occurring beyond visual line of sight.

As the FAA continues to examine how to integrate UAS into the NAS, work has continued to create high quality weather-sensing UAS (WxUAS). Traditionally, observations of the atmosphere using WxUAS utilized fixed-wing aircraft (e.g., Reuder et al. 2009; Chilson et al. 2009; Houston et al. 2012; Reuder et al. 2012; Bonin et al. 2013; Lawrence and Balsley 2013; Wildmann et al. 2014, 2015; Frew et al. 2020). Using fixed-wing WxUAS allowed researchers to leverage major technological advances from decades of measurement research from piloted aircraft (e.g., Gioli et al. 2006; Saide et al. 2015). Additionally, fixed-wing WxUAS are capable of flight times of an hour or more, allowing researchers to cover a large spatial range.

In recent years, the commercial boom of UAS has made rotary-wing UAS (rwUAS) easily accessible to the public. Researchers are now turning to rwUAS because they are more versatile, readily available, and are relatively easy to operate. A common application of rwUAS in atmospheric science is collecting thermodynamic and kinematic variables as a function of altitude, similar to the traditional radiosonde. Forecasters and researchers can use the same conceptual framework as radiosondes to analyze and interpret data from rwUAS profiles. In a sense, the framework is even more applicable since rwUAS can remain somewhat fixed over the same geographical location during observation periods while radiosondes drift many kilometers downwind.

Using rwUAS poses new challenges that must be overcome before they can be considered a viable platform for atmospheric observation. For example, the rotor-wash of rwUAS modify the environment surrounding them, so measuring ambient variables like temperature can be difficult. Careful considerations must be made to ensure the true environmental temperature is being measured, as opposed to the modified rwUAS environment. Additionally, proper aspiration of the sensors and



shielding from solar radiation is vital to accurate measurements (Tanner et al. 1996; Hubbard et al. 2004; Greene et al. 2018, 2019).

For this study, a WxUAS developed by the Center for Remote Sensing and Sampling (CASS) at the University of Oklahoma (OU) was used to evaluate the thermodynamic state in multiple conditions. This WxUAS is described in detail below.

### **1.3.2.1 The CopterSonde**

The CopterSonde v2.5 is a WxUAS developed by CASS for the purpose of collecting thermodynamic and kinematic profiles of the ABL at a high vertical resolution. The original CopterSonde was built and deployed for the Environmental Profing and Initiation of Convection campaign (EPIC, Koch et al. 2018). The original plan was to use an off-the-shelf rotary wing UAS, but it was determined that there was no airframe that could account for the needs of atmospheric sampling. Thus, the original CopterSonde was build and deployed during EPIC with mixed results (Koch et al. 2018). Details on the original CopterSonde can be found in Greene (2018).

Despite the mixed results, many lessons were learned about the design and mode of operation. The second version of the CopterSonde was developed for the 2018 Innovative Strategies for Observations in the Arctic Atmospheric Boundary Layer (ISOBAR) campaign (Kral et al. 2018). For this version, several upgrades were implemented to improve the quality of data collected by the UAS. Instead of the temperature and humidity sensors simply being attached to the frame of the UAS as “passengers”, the sensors were directly integrated into the nose of the CopterSonde using a custom, 3D-printed shell. The shell also shielded the sensors from solar radiation and aspirated the sensors with a ducted fan. Custom autopilot software was created to make sure that the nose of the CopterSonde always pointed into the wind. All these improvements minimized the effect of the UAS itself on the sensors (Greene

et al. 2019). More details on the development of the CopterSonde are available in Segales et al. (2020).

Data from the CopterSonde were processed to a 3-m vertical resolution starting from 6 m above ground level (AGL) in order to not contaminate the profile with effects induced by the ground before the ducted fan activates. The temperature measurements were made using three iMet-XF glass bead thermistors while the relative humidity measurements were made using three Innovative Sensor Technology HYT 271 relative humidity sensors. Three sensors were used for redundancy; if one sensor went bad, the other two could be used to automatically identify the bad sensor. If only 2 sensors were used and a sensor malfunctioned, it would be difficult to determine the faulty sensor automatically. Wind speed and direction were calculated using a methodology based on Neumann and Bartholmai (2015a), which used the tilt of the airframe to estimate the velocity. This was done in real time so that custom autopilot software could always direct the nose of the CopterSonde into the wind, which improved thermodynamic and kinematic measurements (Greene et al. 2019). Herein, the thermodynamic package and ducted fan are referred to as the “scoop”. The methodology used to estimate the wind speed will be expanded upon in Chapter 4.

The sensors in the CopterSonde scoop were characterized in the Oklahoma Climatological Survey calibration laboratory. The entire scoop was placed inside of a controlled calibration chamber and aspirated using the ducted fan to account for any heat that emanated from the fan. The scoop was calibrated for 1-hr periods at multiple chamber reference temperatures and humidities. Data from each sensor in the scoop were compared to a calibrated thermistor and a chilled-mirror hygrometer and any sensor bias was corrected. CopterSonde data used in this analysis had these correction curves applied.

## 1.4 Research Questions

These new technologies have the potential to revolutionize observations in the ABL and provide insights into atmospheric processes that have largely not been routinely observed with operational instrumentation. However, all of these systems need to be evaluated against each other to determine what systems may be appropriate for different atmospheric situations and geographical areas. The studies contained herein aim to begin to answer the following research questions:

- How well do these platforms currently address the ABL data gap? Are there any deficiencies in the platforms that could hinder scientific progress?
- Can we leverage the strengths of one type of observation to improve other types of observations in order to better meet proposed benchmarks for ABL profilers?
- Can we combine observations from these platforms in a synergistic fashion to provide a more accurate and/or useful product that better addresses the ABL data gap?
- Which instruments or combination of instruments are best for different gap-filling network types and applications?
- What considerations need to be made for each platforms in order to fulfill various needs?

To evaluate these questions, data from multiple field campaigns from around the United States were used. Chapter 2 describes the field campaigns in more detail and reviews how each instrument was used during the campaign. In Chapter 3, a detailed intercomparison and validation to identify potential weaknesses and/or strengths in the observation platforms is described. Based on what is learned, Chapter 4 summarizes ways to improve any weaknesses in the platforms and identifies potential synergies between the systems. These synergies are discussed further in Chapter 5.

## Chapter 2

### Field Campaigns

For the remainder of this study, data from numerous field campaigns will be used to answer the research questions outlined above. Since data from these campaigns will be dispersed throughout, this chapter will describe the motivation behind each campaign, a general description of the meteorological conditions pertinent to the ensuing analyses during each campaign, and the locations of the data collected. Table 2.1 and Figures 2.1 and 2.2 summarize general information and instrument locations for each campaign. They cover a wide range of geographic locations, terrain complexity, and background weather conditions with the goal of generalizing the analyses as much as possible.

#### 2.1 VORTEX-SE

The Verification of the Origins of Rotation in Tornadoes Experiment Southeast (VORTEX-SE) is a campaign designed to examine how the environment of the southeastern United States (US) affects the formation, propagation, and impact of tornadoes that occur in this region. The southeast (SE) US climatologically has more tornado deaths than any other region. Ashley (2007) found that these high fatality rates are likely due to a combination of factors unique to the SE US, including a relatively high frequency of tornadoes (many of which are a nocturnal tornado threat), a high density of mobile homes, and a relatively high population density. While VORTEX-SE aims to further the understanding of the meteorological processes that lead to the development of tornadoes in the SE, there is also important social work that has occurred to help understand the public perception of safety and the uncertainty of forecasts in this region (e.g., Lim et al. 2019; Ash et al. 2020; Walters et al. 2020).

Table 2.1: Summary of dates, locations, and the instruments present during the field campaigns discussed in Chapter 2.

Deployment Name	Deployment Information		
	Dates	Location	Instruments
VORTEX-SE	April 2017	Scottsboro, AL	CLAMPS2
LAPSE-RATE	14 to 20 July 2018	Moffat, CO	CLAMPS1, CopterSonde, Radiosonde
Flux Capacitor	15 to 16 October 2018	Washington, OK	CLAMPS1, CopterSonde, Radiosonde

Since 2016, additional instrumentation (e.g., thermodynamic profilers, wind profilers, mobile Doppler radar, and radiosondes) has been deployed during the cool season (February through April) across the SE US to study how the meteorological processes in the southeast differ from those in the Southern Great Plains, where tornado-oriented field campaigns have typically been held in the past. Since 2016, at least one CLAMPS facility has been deployed each year to the SE in support of VORTEX-SE. For the purpose of the studies to follow, the CLAMPS2 data from 2017 were used due to their relative high quality. Data collected by CLAMPS in 2017 were relatively continuous for the AERI, DL, and MWR.

During the 2017 campaign, CLAMPS2 was deployed at Scottsboro Municipal Airport in Scottsboro, Alabama. Scottsboro sits near the Tennessee River in northeast Alabama. The terrain to the west is characterized by forested hills while to the east is a large, relatively flat plateau (Sand Mountain). During this deployment, both the AERI and MWR in CLAMPS2 were operational. The DL performed 8-point VADs every 5 minutes, and staring vertically between each VAD. The AERI data

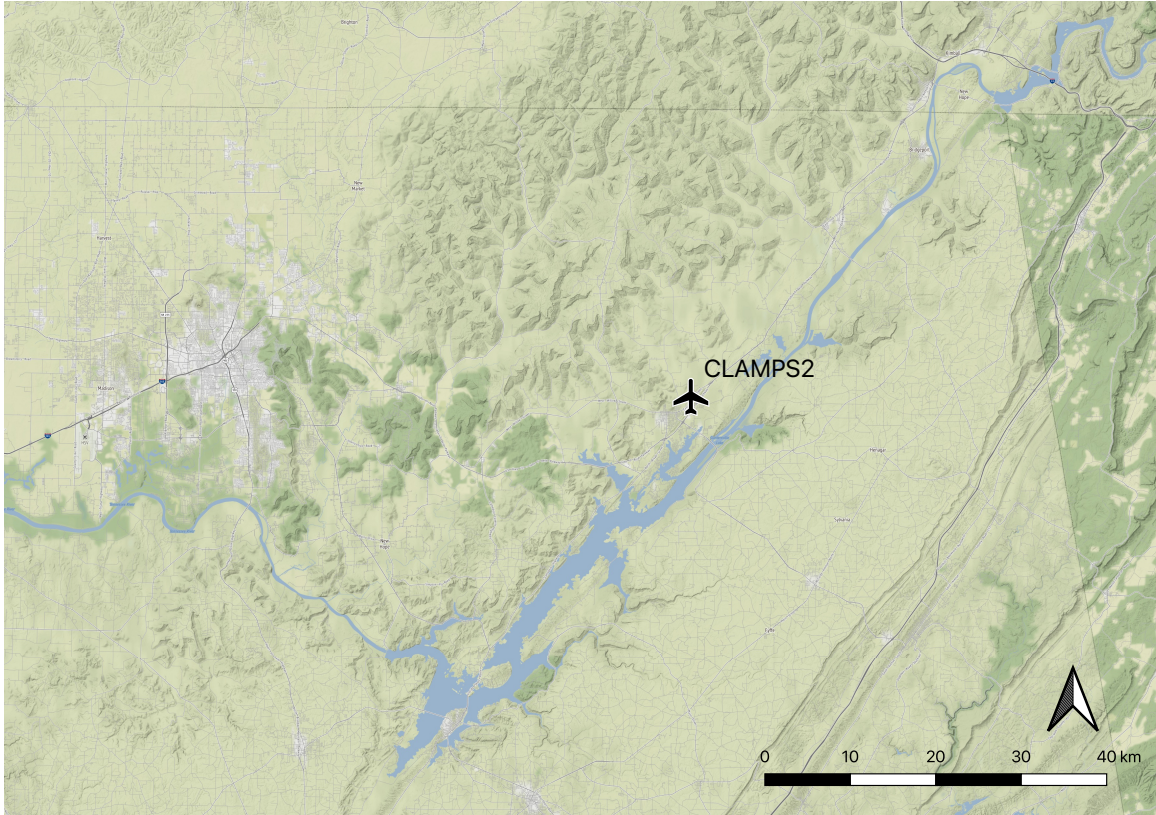


Figure 2.1: Caption

were post-processed through TROPoe at 10-minute resolution using Rapid Refresh (RAP) model temperature and moisture to constrain the atmosphere above 4 km while surface temperature and relative humidity from the CLAMPS meteorological station were used to constrain the surface.

## 2.2 LAPSE-RATE

The Lower Atmospheric Process Studies at Elevation—a Remotely piloted Aircraft Team Experiment (LAPSE-RATE) campaign took place from 15–19 July, 2018 following the annual meeting of the International Society for Atmospheric Research using Remotely piloted Aircraft (ISARRA) in the San Luis Valley in southern Colorado. Multiple university, international, and private-sector groups deployed WxUAS and

other assets like mobile mesonets and ground-based profilers (de Boer et al. 2020a; Bell et al. 2021; de Boer et al. 2021).

Previous flight weeks associated with ISARRA primarily focused on demonstrating developments that have been made in WxUAS technology and intercomparing all the WxUAS with each other. While there still was a large focus on this (Barbieri et al. 2019), LAPSE-RATE was the first effort to focus on organizing the WxUAS in a way to enable data collection for scientific analysis. The San Luis valley provided an opportunity to study flow in complex terrain due to the mountain ranges to the east and west. Topics of interest in the San Luis Valley include complex valley flows, the impact of complex terrain on convection initiation, and morning boundary-layer transition in the arid, high-altitude terrain (de Boer et al. 2020b). The valley floor is primarily flat shrubland and irrigated agricultural fields. The eastern portion of the valley is primarily shrubland while the western portion contains irrigated farmland. This dichotomy can create complex moisture gradients inside the valley which are thought to influence CI.

Both the CopterSonde and the CLAMPS facility were deployed during LAPSE-RATE to the center of the valley in Moffat, Colorado (Figure 2.2). CLAMPS was positioned there to collect continuous observations of the background state of the atmosphere in the valley. In addition, a CopterSonde was deployed to the Saguache Airfield approximately 25 km northwest of Moffat. During the week, WxUAS flew during targeted intensive observation periods (IOP). These IOPs typically began in the early morning and continued to late morning or early afternoon, depending on the goal of the flights for that day. For LAPSE-RATE, Certificate of Authorization was active that allowed WxUAS flights up to 910 m AGL. When practical and useful, the CopterSonde flew at a 15-minute cadence (i.e., the CopterSonde took off and landed every 15 minutes). This tempo was reduced to a 30-minute cadence if conditions were determined to be steady-state or it was unsafe to continue at the faster cadence.

During LAPSE-RATE, the CLAMPS DL scan strategy consisted of an 18-point VAD (Browning and Wexler 1968) at a  $70^\circ$  elevation angle and 6-point VAD scan at a  $45^\circ$  elevation angle that occurred every 5 minutes. During all other times, the DL was in vertical stare mode to collect vertical velocity statistics. For the ensuing analyses, only the 18-point VAD was used since the 6-point VAD was primarily for situational awareness when flying the CopterSonde.

The thermodynamic data collected by the AERI in CLAMPS were processed through the TROPoe retrieval described in Section 1.3.1.4. These retrievals were constrained by surface temperature and moisture data collected by the Vaisaa WXT-530 weather station that is part of CLAMPS. Additionally, the co-located radiosondes launched from CLAMPS were used to constrain the atmosphere above 3 km AGL since the AERI primarily contained information below 2 km AGL (Turner and Löhnert 2014). Retrievals were calculated every 15 minutes in order to match the cadence of the CopterSonde.

## 2.3 Flux Capacitor

Flux Capacitor was an OU sponsored campaign where various OU groups combined efforts to gather a high-resolution dataset of atmospheric fluxes at multiple scales. One of the main goals was to capture a full diurnal cycle with the CopterSonde to demonstrate the 3D-Mesonet concept (Chilson et al. 2019). The following analyses primarily focus on data collected during an IOP on 5–6 October, 2018 where the CopterSonde, CLAMPS, and radiosondes were launched in a similar manner to LAPSE-RATE. The campaign took place at the Kessler Atmospheric and Ecological Field Station (KAEFS), which is approximately 28-km SW of the OU Norman campus and is a primary testing site for the CopterSonde.

During Flux Capacitor, CLAMPS was again co-located with the launch site for the CopterSonde, allowing comparisons between the systems. CopterSonde flights



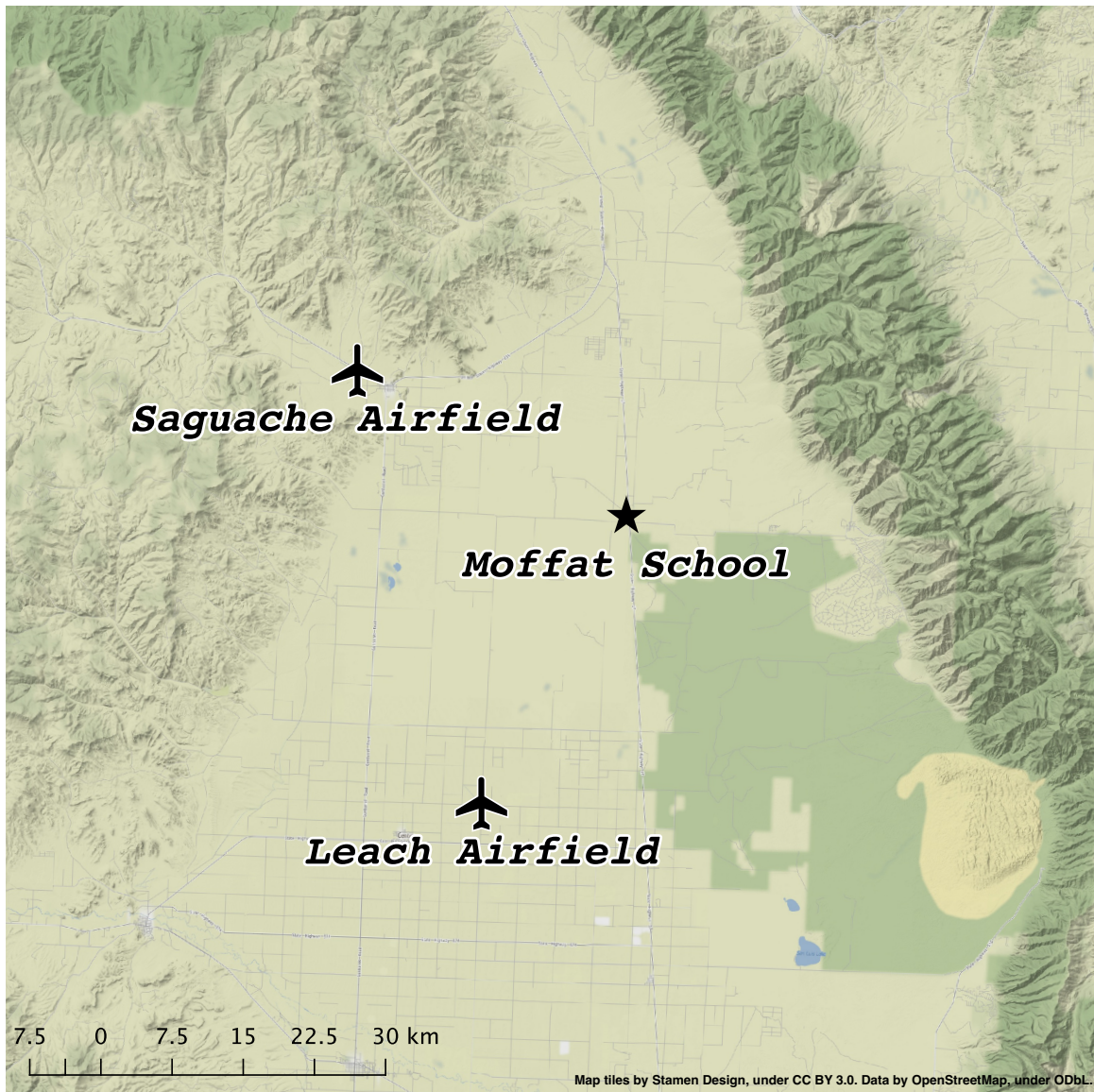


Figure 2.2: Key locations during the LAPSE-RATE field campaign in 2017. CLAMPS1 and CopterSondes were deployed at the Moffat School. Other WxUAS were flown at both Saguache Airfield and Leach Airfield, but are not examined in the following studies.

were conducted on a 30-minute interval up to a max altitude of 1,200 m AGL. In total, 46 flights were conducted over a 24-hour period. Two flights were missed due to mechanical issues with the CopterSonde, which have since been addressed.

## Chapter 3

### Instrument Intercomparison

In order to identify potential limitations in the instruments discussed in Section 1.3, the following analysis compares WxUAS and ground-based remote sensing data collected by CLAMPS to the historical standard for atmospheric profiling: the radiosonde. Intercomparisons of data collected from both LAPSE-RATE and Flux Capacitor (Section 2.3) are analyzed to determine the strengths and weaknesses of each platform. Additionally, synergies between WxUAS and ground-based remote sensing are identified. Note, the results presented in this chapter have previously been published in Bell et al. (2020).

#### 3.1 Statistical Comparison of Systems

It is important to characterize differences statistically to draw conclusions about system performance relative to each other. For each of the system combinations (CLAMPS–Copter, CLAMPS–Radiosonde, Copter–Radiosonde), data from all heights and from both campaigns are compared to one another. A large number of data points are needed to draw any conclusions since the measurements from each platform are based on different assumptions and affected by different sources of error. While all three profiling methods are most often interpreted as a perfect vertical profile, this is obviously not true. For example, the VAD scan assumes that the wind field is horizontally homogeneous and stationary in order to retrieve the horizontal wind vector. This means the DL observations are averaged spatially both in terms of radial bins and the PPI scan required to calculate the VAD. Additionally, radiosondes drift and

can often be collecting in situ measurements far from the launch point. So while comparing the systems one-to-one may not be ideal, at this point it is the best approach available to us.

Due to these limitations, any spread in the data presented from the following analyses contains three components: one component from instrument imprecision, one from the inability of the instruments to measure the same point at precisely the same time, and one component that arises from the differences in measurement technique. The goal of this study was to examine the spread that arises from the measurement technique itself.

Therefore, in order to eliminate any differences due to changing atmospheric conditions, data points with a difference that lie outside the  $2\sigma$  envelope are considered outliers and were removed from the analysis. As a result, most of the comparisons had under 10 percent of the points removed. However, the kinematic comparison between the radiosonde and the DL had the largest percentage of points removed at 33 percent. This was due to a combination of fewer overlapping observations and the fact that the VAD technique and radiosondes struggle to capture the very low wind speeds observed during the daytime hours of LAPSE-RATE. In general, approximately 15 percent of profiles had at least one outlier. Of these 15 percent, the median number of outliers per profile was 2. These outliers followed no apparent pattern and would not contribute to any observed bias.

The outliers from the thermodynamic comparisons exhibited a different pattern. While fewer profiles overall contained outliers, there tended to be more outliers within affected profiles. After analyzing these cases in depth, it was concluded that most of the outliers were likely due to changing atmospheric conditions between measurement times. Put another way, since the measurements were not taken at exactly the same moment, non-stationary conditions could lead to different conditions being measured between the two observations.

### 3.1.1 CLAMPS vs CopterSonde

Kinematic and thermodynamic data from CLAMPS and the CopterSonde are presented in Figs. 3.1 and 3.2, respectively. The wind speed and direction from the CopterSonde and the 12-point VAD performed by CLAMPS compare remarkably well. In general, wind speeds less than  $5 \text{ m s}^{-1}$  are from LAPSE-RATE while the higher wind speeds are associated with the low-level jet observed during Flux Capacitor. The Pearson correlation (hereafter, just “correlation”) between wind speed and wind direction is 0.976 and 0.83, respectively. There is some disagreement in wind speed between the VAD and the CopterSonde, especially at higher wind speeds. This is discussed more in the next section.

The observed wind directions are largely bi-modal (Figure 3.1c), with one group of observations around 90 degrees and one group around 180 degrees. The group around 180 degrees largely consists of observations from the Flux Capacitor dataset (southerly low-level jet) while the group around 90 degree is largely from LAPSE-RATE (easterly katabatic flows from mountains). Additionally, there are points scattered elsewhere that are also largely from LAPSE-RATE.

Overall, the wind directions have a correlation of 0.83. The low wind speeds from LAPSE-RATE make it difficult to accurately measure the wind direction on both the CopterSonde and the CLAMPS DL; the CopterSonde needs strong enough wind to tilt the craft while the DL needs a strong enough wind to ensure homogeneity over the scan volume. This results in a large standard deviation in the differences. This can also be seen in Figure 3.3a. Additionally, there appears to be a small bias in wind directions from LAPSE-RATE. This is likely due to uncertainties in the true heading of the DL.

The comparison of the thermodynamic measurements reveals deficits in the AERI moisture retrieval. The data points for the AERI moisture retrievals have more spread than those for the temperature retrieval, especially in the dry, hot conditions observed

during LAPSE-RATE (dew point temperatures below 13°C in Figure 3.2c). The AERI moisture retrievals performed better during the Flux Capacitor campaign (dew point temperatures greater than 15°C), which could be due to the more representative prior used for the retrieval. This prior data is used to help initially constrain the retrievals. The prior dataset used for the Flux Capacitor retrievals was generated from radiosondes launched from the National Weather Service (NWS) in Norman, OK. The LAPSE-RATE prior was constructed with radiosondes launched by the NWS in Boulder, CO, which may not fully represent the conditions in the San Luis Valley. For reference, the distance between KAEFS and NWS Norman is approximately 23 km, while the distance between Moffat, CO and Boulder, CO is approximately 220 km.

Overall, the mean difference in dew point temperature between the CopterSonde and the AERI was -0.190°C, with a standard deviation of 1.681°C. The CopterSonde temperature and the AERI temperature retrieval have a high correlation of 0.981. The difference between the CopterSonde and the AERI temperatures average to 0.038°C, with a standard deviation of 0.817°C.

### 3.1.2 Radiosonde vs CopterSonde

Figure 3.4 shows the wind speeds estimated by the radiosonde compared to the CopterSonde estimate. The wind speed observations have a high correlation of 0.969 and a relatively low standard deviation of 1.355 m s<sup>-1</sup>. The same bias in wind speed presented in Section 3.1.1 is also seen here, indicating the CopterSonde is consistently underestimating the wind speed by approximately 0.75 m s<sup>-1</sup>. Possible reasons for this bias are discussed in Section 4.1.

The wind direction from the two systems has a lower correlation (0.853). While the wind directions observed generally agree well (mean difference of 4.204 degrees), there is a large standard deviation (36.854 degrees). Much of this noise results from the low

wind-speed observations from LAPSE-RATE; both the radiosonde and CopterSonde struggle to capture the correct wind direction when wind speeds are low (Figure 3.3b).

The radiosonde and CopterSonde have a high level of agreement between their thermodynamic measurements. The correlation of the temperature and dew point temperature are both 0.99 (Figure 3.5). The temperature comparison is slightly better, evidenced by the lower standard deviation ( $0.408^{\circ}\text{C}$ ) and mean difference ( $-0.091^{\circ}\text{C}$ ). A bias is observed in dew point temperatures lower than  $13^{\circ}\text{C}$ . This grouping of measurements is entirely from the LAPSE-RATE campaign and there is a consistent offset. Given the CopterSonde was calibrated in a lab setting while the radiosondes were not, this could be a moist bias on the part of the radiosondes. However, this has not been documented to the knowledge of the authors. It is also possible that the bias could be a result of a pressure dependency on the relative humidity sensors. Given the AERI moisture retrievals contained a high amount of spread compared to these instruments, it is difficult to determine which system is causing the bias.

### 3.1.3 Radiosonde vs CLAMPS

Finally, Figs. 3.6 and 3.7 show comparisons between the observations from the radiosondes and CLAMPS. The kinematic measurements from radiosondes and the DL compare well with a correlation of 0.984 for wind speed and 0.899 for wind direction (Figure 3.6). There appears to be more noise in the wind directions, corresponding to a mean difference of  $-11.079$  degrees. This is primarily from the low wind speeds observed during LAPSE-RATE where all the systems have difficulty in accurately capturing the wind speed and direction (Figure 3.3). There is a slight wind speed bias in one of the instruments, especially at higher wind speeds. However, since the CopterSonde also exhibited bias when compared with the radiosondes and CLAMPS

(e.g., see Section 3.1.1 and 3.1.2), it is impossible to determine which instrument contributed to the bias. These results are similar to the results of Päsche et al. (2015), in particular the better performance at higher wind speeds.

Figure 3.7 shows the thermodynamic comparisons between radiosondes and the AERI retrievals. These observations have a high correlation of 0.98 and a mean difference of  $-0.17^{\circ}\text{C}$  for temperature. The median difference is  $0.249^{\circ}\text{C}$  and  $0.324^{\circ}\text{C}$  for temperature and dew point temperature, respectively. These results also agree with past comparisons of AERI retrievals to radiosondes (Blumberg et al. 2015a; Turner and Blumberg 2019), namely the finding that the temperature retrieval tends to perform better (in terms of uncertainty) than the moisture retrieval.

## 3.2 Case Studies

It is meaningful to analyze a couple of case studies in order to better understand how various features observed in the statistical analysis manifest themselves in individual profiles. Case studies also provide perspective on the conditions observed during the campaigns. Representative cases from both Flux Capacitor and LAPSE-RATE are next discussed to illustrate the different conditions observed.

### 3.2.1 LAPSE-RATE Case Study

The first case considered is for 19 July, 2018. During this period, the focus of LAPSE-RATE participants was to capture drainage flows in the northwest part of the valley. CLAMPS and one of the CopterSonde teams continued to operate at the Moffat site during this period. Figure 3.8 shows the temperatures and wind speeds observed by CLAMPS and the CopterSonde at the Moffat site during this period. Flights started shortly after 11 UTC while there was still a strong nocturnal temperature inversion present and continued until 17 UTC. During this period, some of the highest wind speeds observed during LAPSE-RATE occurred.



Examining an example profile reveals some of the features presented in the statistical analysis. The wind speeds generally all fall within  $2 \text{ m s}^{-1}$  of each other, with the CopterSonde wind speed estimates generally tending to be the lowest (Figure 3.9a). In terms of wind direction, the instruments all follow the same general pattern with height and are generally within 20 degrees of each other (Figure 3.9b). There is a wind speed maximum around 200 m AGL, likely due to the drainage flows from the surrounding mountains. The directional shear layer starting at approximately 600 m AGL also indicates the presence of a slope flow.

The thermodynamic comparison between the AERI, CopterSonde, and radiosonde is shown in Figure 3.9c. As would be expected, a nocturnal inversion is present. While all the systems capture the inversion, the measurements are slightly different. The AERI retrieval smooths out the temperature inversion and shows the maximum temperature to be higher both in elevation and magnitude than as represented by the UAS and the radiosonde. This is a common occurrence in the data from the LAPSE-RATE campaign and may be due to the prior dataset that was used to generate the initial guess for the LAPSE-RATE retrievals, as mentioned in Section 3.1.1.

Additionally, there is a consistent offset between dew point temperatures measured by the CopterSonde and the radiosondes, which is observed throughout the LAPSE-RATE campaign. In addition, the AERI moisture retrieval performs poorly close to the surface. This could be due to a bad surface constraint.

### **3.2.2 Flux Capacitor Case**

The next case considered is from the OU-organized Flux Capacitor campaign in October 2018 (Figure 3.10). During the overnight hours of the study period, wind speeds were much higher than the LAPSE-RATE case due to the onset of a nocturnal low-level jet (LLJ, Figure 3.10b). This is a common nighttime feature for the Southern

Plains, thus it is important to characterize how the CopterSonde performs in these high winds.

Figure 3.11 shows observations from the three systems on October 6, 2018 at 0232 UTC. During this time period, maximum wind speeds reached  $20 \text{ m s}^{-1}$  around 850 m AGL. Due to the high winds, the flight was terminated before reaching 1,200 m; this is one of the limitations of the CopterSonde. The CopterSonde also slightly underestimates the wind speed compared to the other systems once the vertical shear decreases. This could be due to the CopterSonde being calibrated for wind while it is stationary, rather than while it is ascending. It could also simply be that the calibration coefficients for wind speed are not valid for such high velocities. More investigation is needed in this area.

The thermodynamic data from the systems deployed during Flux Capacitor are in better agreement than the data obtained during LAPSE-RATE. All instruments are able to capture the nocturnal temperature inversion and accurately capture the residual layer. The difference in dew point temperature between the radiosonde and the CopterSonde is much smaller and the instruments agree well. The dew point temperature from the AERI has a slight bias, but captures the general shape of the profile much better. This is likely due to the more appropriate prior used for the thermodynamic retrievals.

### **3.3 Issues Identified**

In general, measurements between the the WxUAS, CLAMPS, and the RS92-SGP radiosonde all compared relatively well with correlations between all the instruments and variables exceeding 0.85. However, there are important nuances to the analysis that must also be discussed. One important finding from this study is the CopterSonde 2.5 likely underestimates the horizontal wind speeds when compared to both

the radiosonde- and VAD-measured wind. There are numerous reasons this could happen and they will be further explored in Chapter 4.

In addition to the kinematic measurements from the CopterSonde, issues with the thermodynamic retrievals during LAPSE-RATE were identified, most notably in the moisture fields. Again, there are multiple reasons that could explain this. One of the major issues with the LAPSE-RATE retrievals is the relatively large distance between the actual observations site and the location of the NWS radiosonde launch location on which the a priori for the retrieval was developed. This possible sensitivity will also be analyzed in Chapter 4.

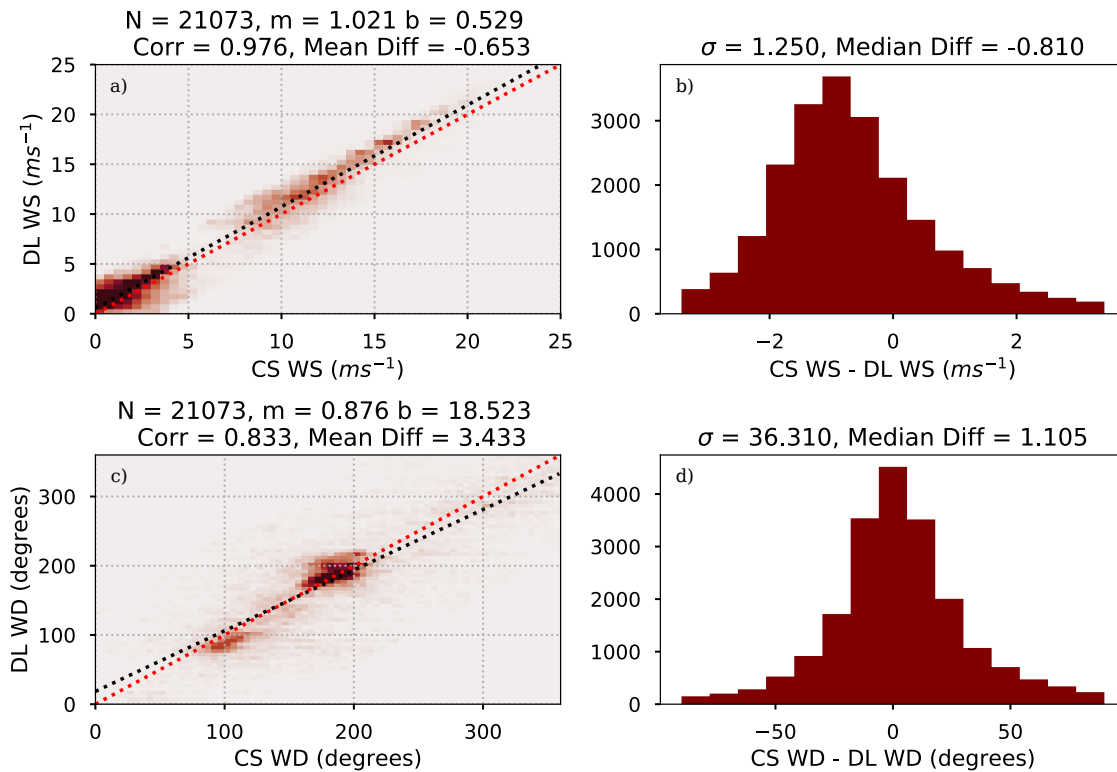


Figure 3.1: Two-dimensional histograms of DL measured wind speed vs CopterSonde measured wind speed (a) and DL measured wind direction vs CopterSonde measured wind direction (c). The 2D histograms are binned to  $0.5\text{ m s}^{-1}$  for wind speed and 5 degrees for wind direction. The histograms on the right show the difference in wind speed (b) and wind direction (d). The red dotted line is the 1-to-1 line and the black dotted line is the least-squares regression. The slope ( $m$ ) and intercept ( $b$ ) are shown in the titles. Various other statistics are also shown in the titles.  $N$  corresponds to the number of points,  $Corr$  is the Pearson correlation,  $Mean\ Diff$  is the mean difference between the CopterSonde and the DL,  $\sigma$  is the standard deviation of the differences, and  $Median\ Diff$  is the median difference between the CopterSonde and the DL.

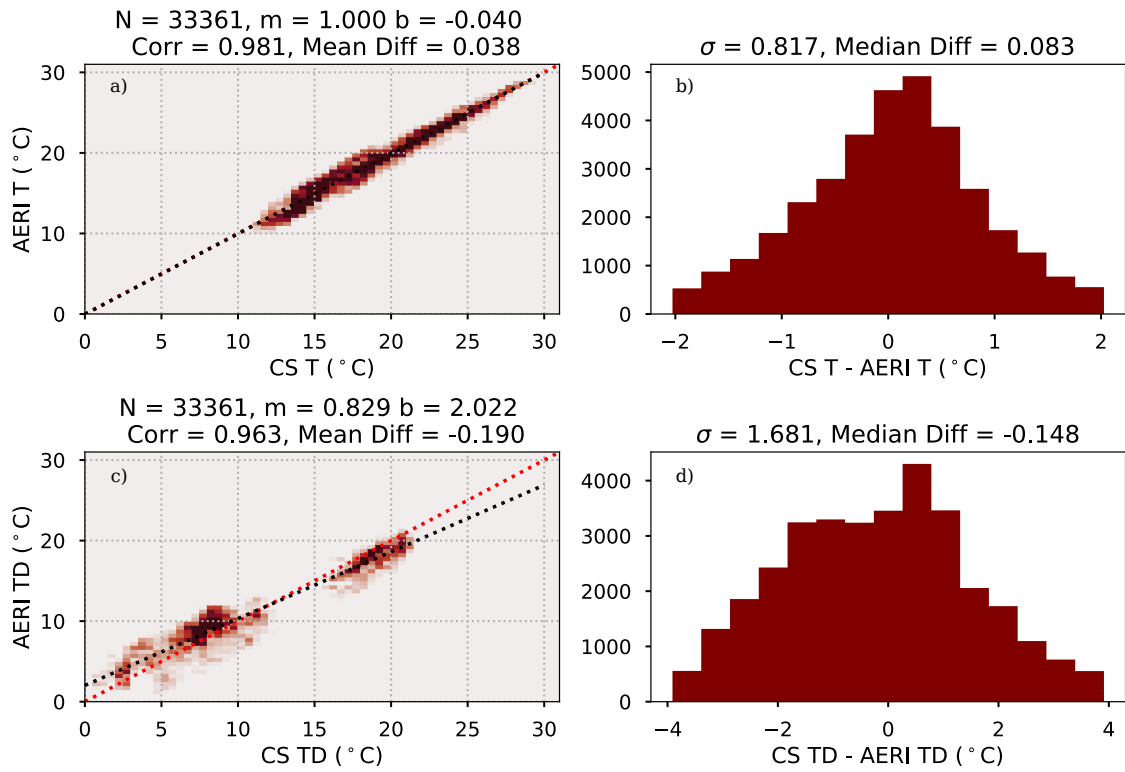


Figure 3.2: Similar to Figure 3.1, except for the air temperature (a and b) and dew point temperature (c and d). The 2D histograms of temperature and dew point temperature are binned by  $0.5^{\circ}\text{C}$ .

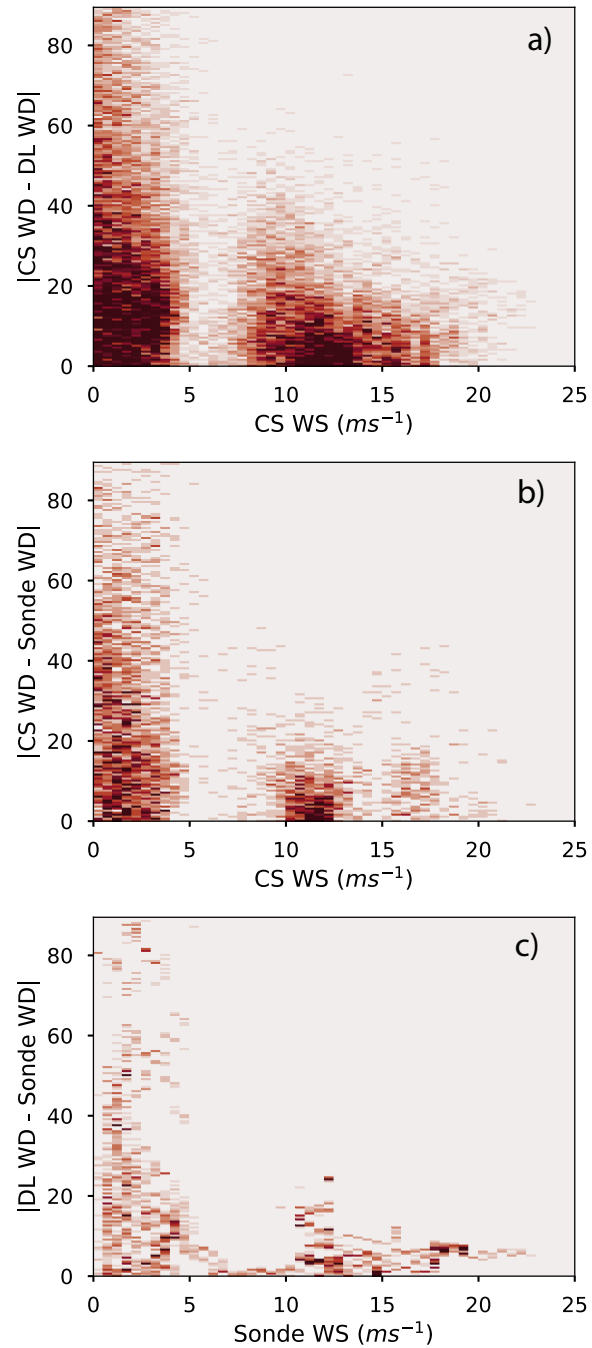


Figure 3.3: Two-dimensional histograms of absolute wind direction difference vs wind speed for the CopterSonde and DL (a), CopterSonde and radiosonde (b), and DL and radiosonde (c). This shows that the lower wind speed measurements have a higher level of uncertainty to the wind direction. Again, the distribution is bi-modal, with LAPSE-RATE observations generally all falling below  $5\text{ m s}^{-1}$

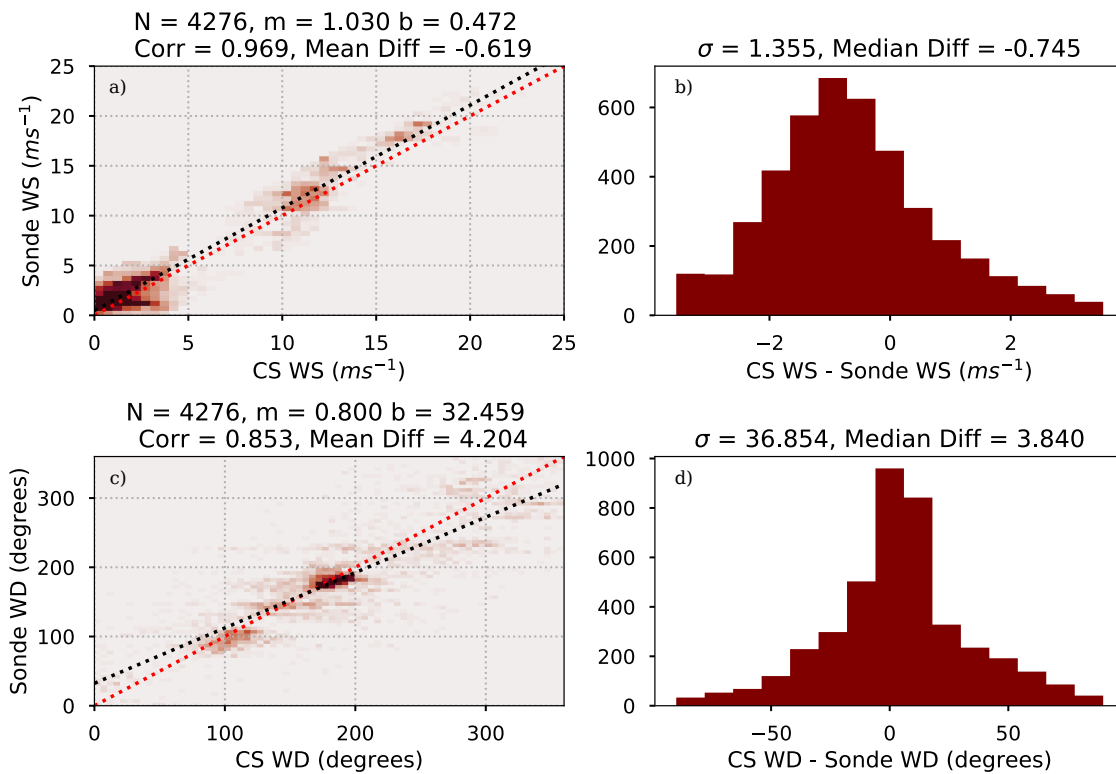


Figure 3.4: Similar to Figure 3.1, except for comparing wind speed (a) and wind direction (c) from the radiosondes and the CopterSonde.

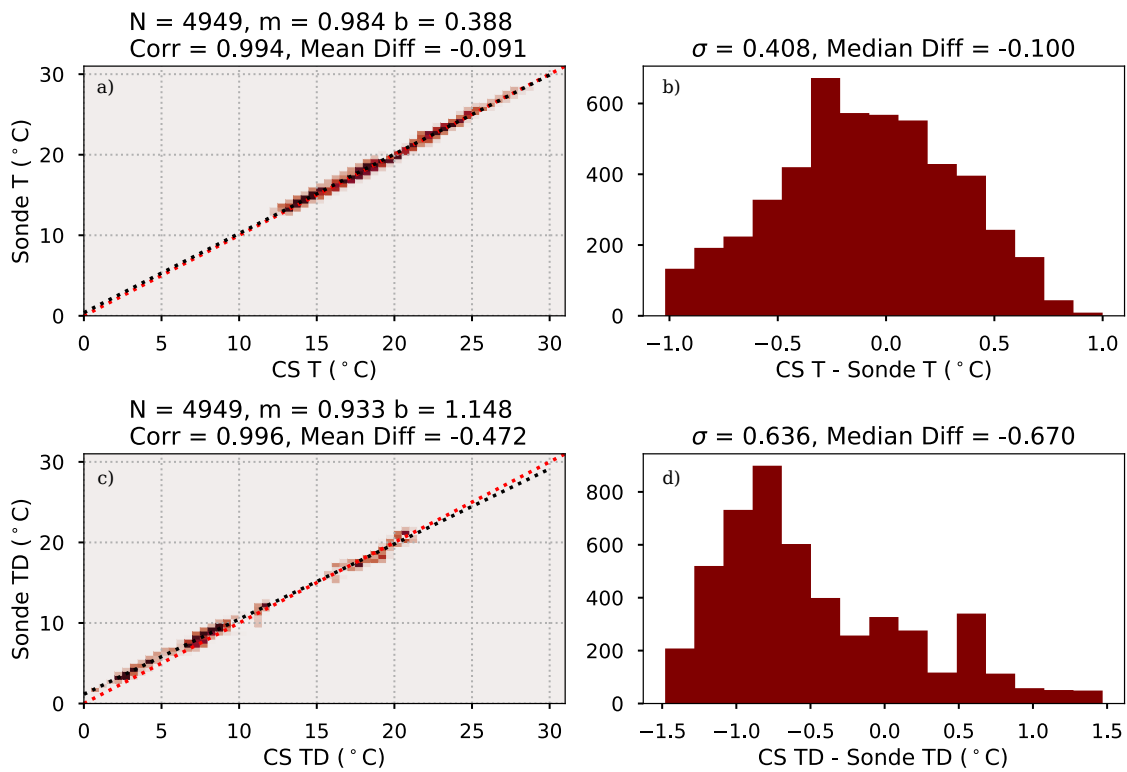


Figure 3.5: Similar to Figure 3.2, except for comparing measurements from the radiosondes and the CopterSonde.



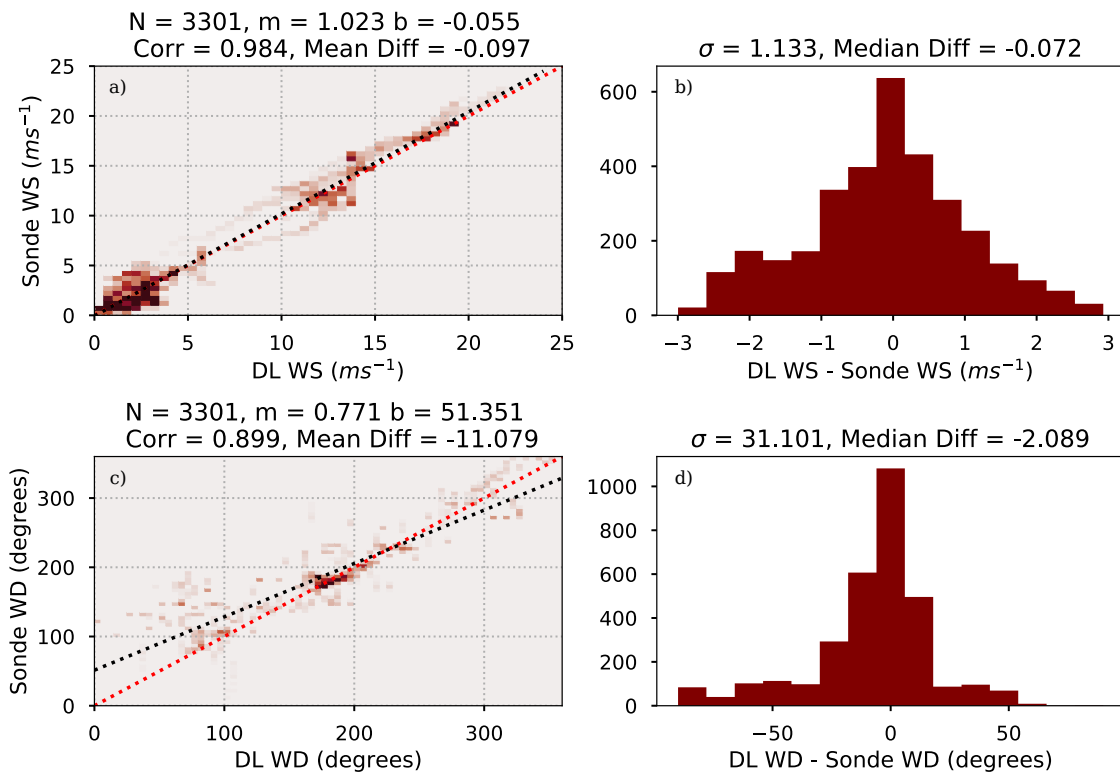


Figure 3.6: Similar to Figure 3.1, except for comparing kinematic measurements from the radiosondes and the DL.

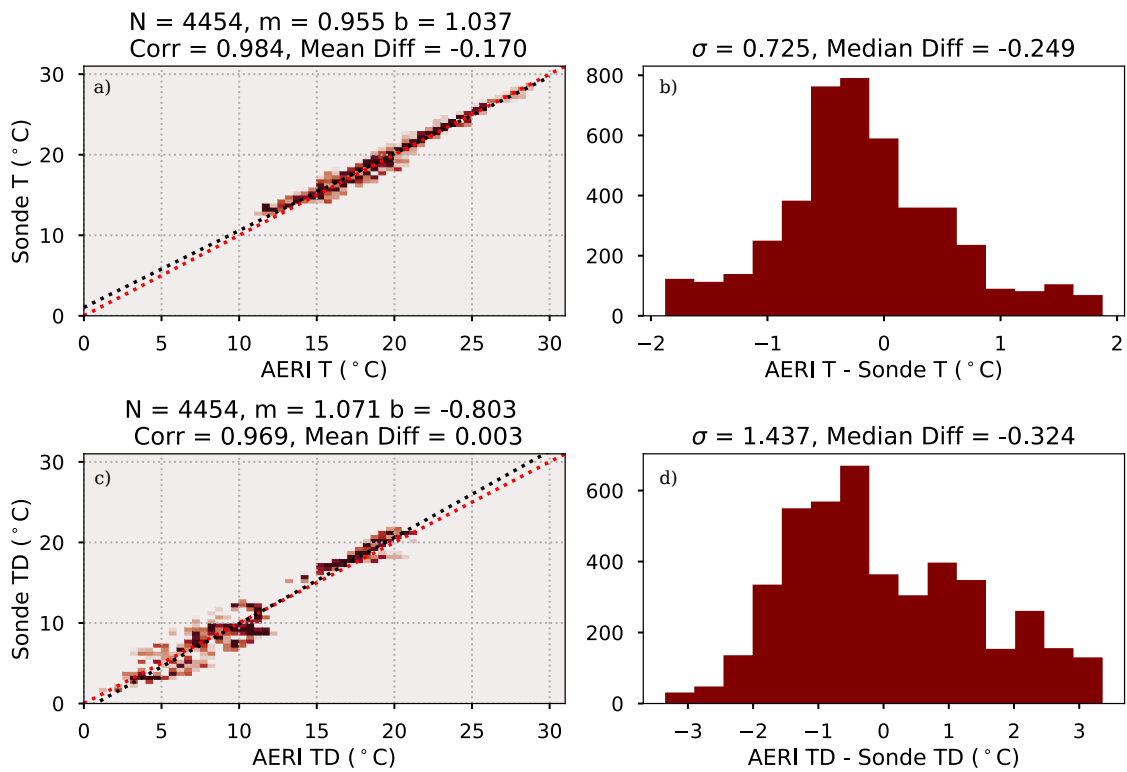


Figure 3.7: Similar to Figure 3.2, except for comparing thermodynamic measurements from the radiosondes and the AERI.

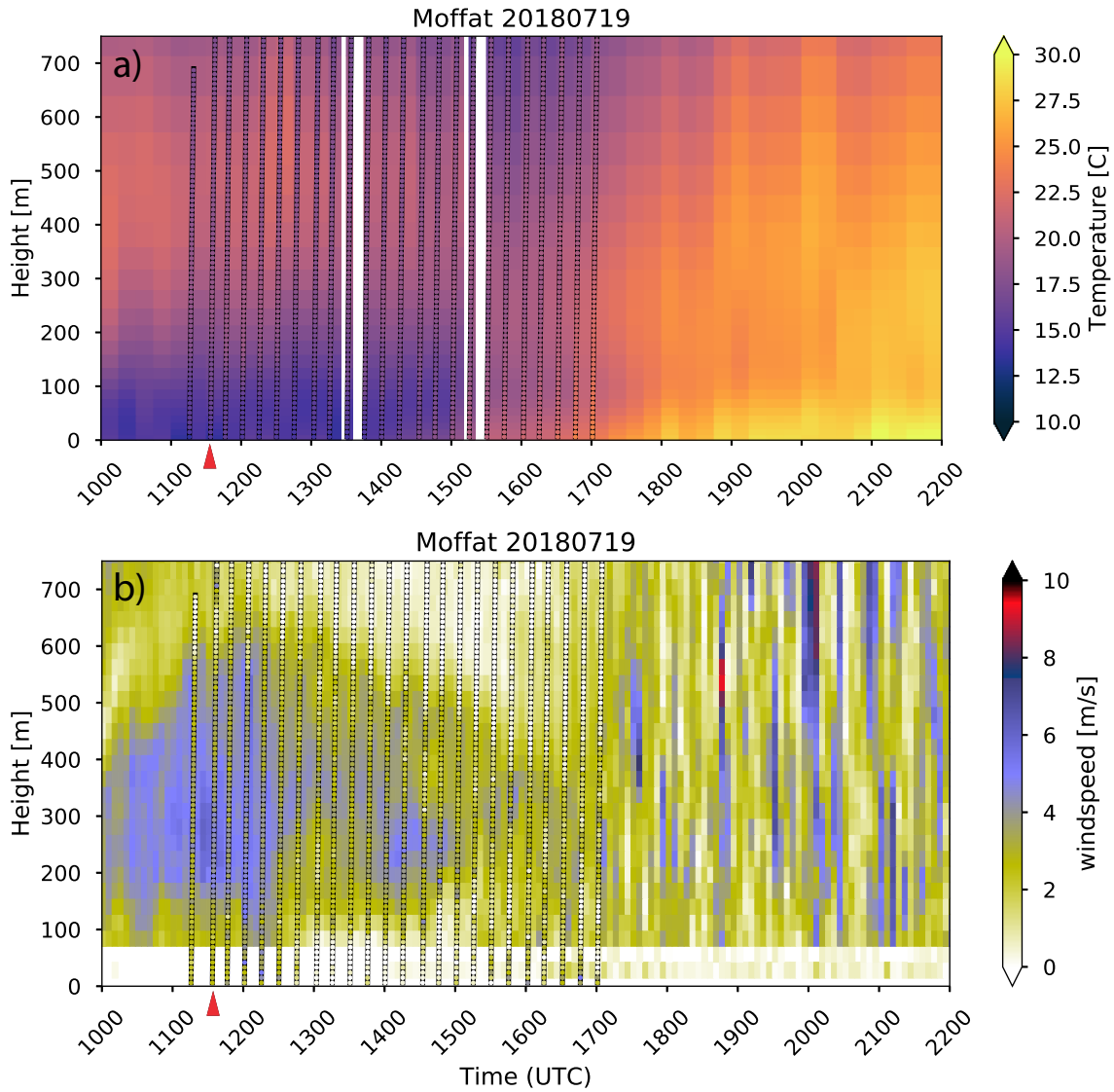


Figure 3.8: Time-height plots of temperature (a) and wind speed (b) from the Moffat site on July 19, 2018. In the top panel, the background is temperature from the AERI retrievals while the points overlaid on top are data from the CopterSonde at approximately 9m resolution. On the bottom, the background is the horizontal wind speed from the DL while the points overlaid on top are data from the CopterSonde at approximately 9-m resolution. The red arrow points to the profile shown in Figure 3.9.

20180719-11:33:47 Coptersonde944

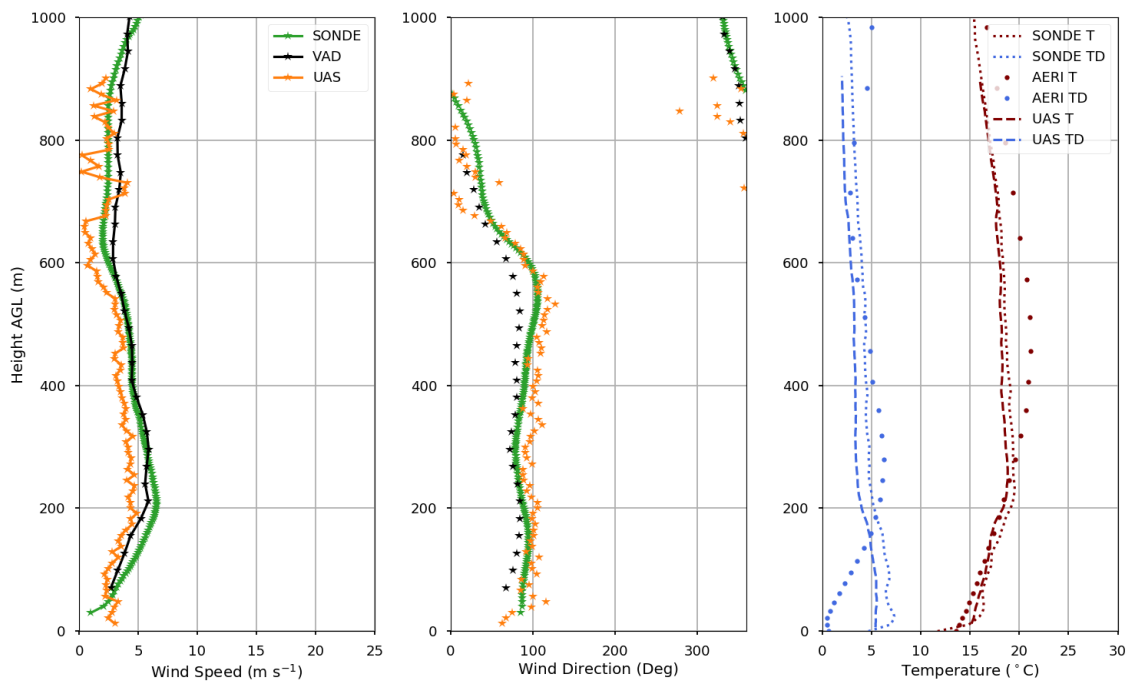


Figure 3.9: Profile plots of wind speed (a), wind direction (b), and temperature and dew point temperature (c) from CLAMPS, the CopterSonde, and a radiosonde on July 19, 2018 at 11:33 UTC. The CopterSonde was launched just after the radiosonde, as soon as it was deemed the radiosonde was not in the flight path of the CopterSonde.

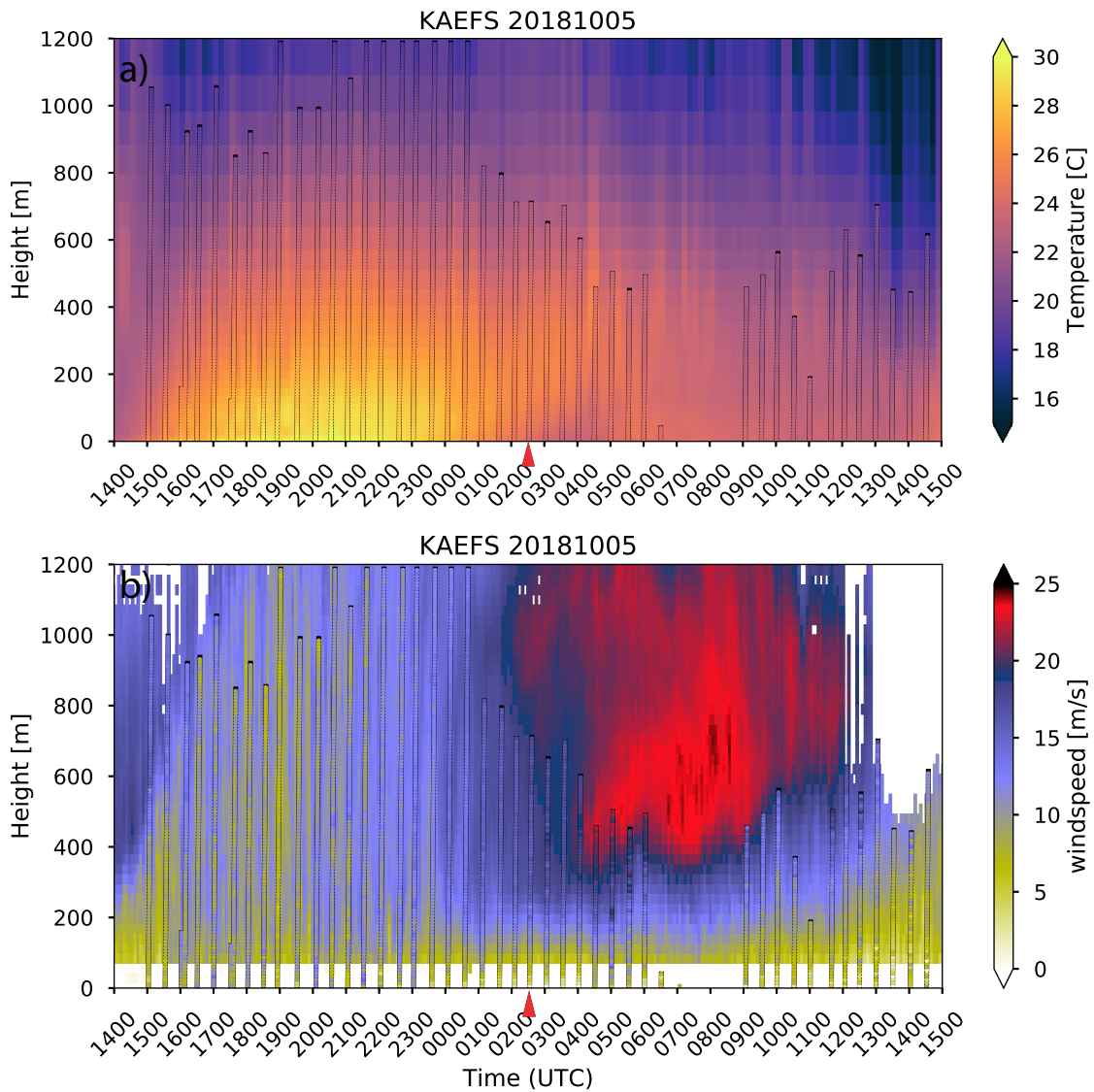


Figure 3.10: Same as Figure 3.8, except for October 5–6, 2018 during the Flux Capacitor campaign. These time-heights contain data from the entire 24-hour period sampled during Flux Capacitor. The red arrow points to the time of the profile shown in Figure 3.11

20181006-02:32:31 Coptersonde955

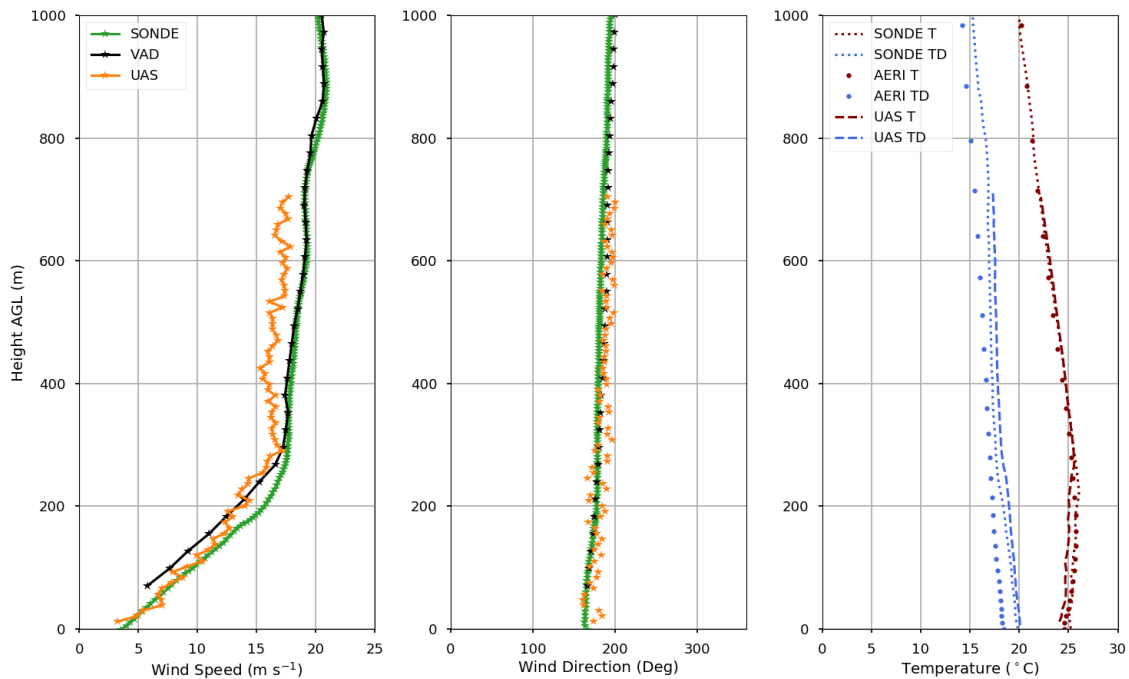


Figure 3.11: Same as Figure 3.9, except for October 6, 2018 at KAEFS during Flux Capacitor. These profiles were from approximately 2:30 UTC.

## Chapter 4

### Identifying instrument synergy

While Chapter 3 primarily focused on identifying issues with various observation techniques using the unique datasets from LAPSE-RATE and Flux Capacitor, these datasets also provide the opportunity to examine how remote sensors and WxUAS could be used synergistically to improve one another. The following sections will examine the use of the CLAMPS DL to help identify the issues with and improve upon the wind speed estimates from the CopterSonde (Section 4.1), the role of the prior in the TROPoe retrieval system (Section 4.2), and attempts to improve the results of the TROPoe retrievals from LAPSE-RATE by also including observations from the CopterSonde (Section 4.2.2).

#### 4.1 UAS Wind Speed Estimates

Since the CopterSonde was designed primarily as a profiling WxUAS, the decision was made early in the development to forego trying to properly fit an anemometer onto the craft. Instead, the fact that the CopterSonde must keep its latitude and longitude fixed and only move in the vertical directions means it must counteract the wind by tilting into it. The associated measurements of tilt and roll thus provide a relatively simple way to measure the horizontal wind speed and direction.

This method was first introduced by Neumann and Bartholmai (2015b). They used a wind tunnel to determine a relation between the pitch and roll measured by the on-board internal measurement unit and the wind speed in the wind tunnel. To achieve this, a simple relation can be derived to determine the wind speed from the tilt of the copter. This was later expanded by Palomaki et al. (2017) to be more

accessible by those without access to a wind tunnel. A brief description is provided below.

If the copter is not accelerating (i.e., the copter is hovering or ascending/decending at a constant rate), we can say that the three main forces acting on the copter sum to zero:

$$0 = \mathbf{G} + \mathbf{D} + \mathbf{T} \quad (4.1)$$

where  $\mathbf{G}$  is the gravitational force,  $\mathbf{D}$  is the drag force, and  $\mathbf{T}$  is the thrust force. From there, the various terms can be expanded:

$$\mathbf{G} = mg\mathbf{e}_D \quad (4.2)$$

$$\mathbf{D} = -D\mathbf{e}_v \quad (4.3)$$

$$\mathbf{T} = T_v\mathbf{e}_v + T_D\mathbf{e}_D = |\mathbf{T}| \sin(\psi)\mathbf{e}_v + |\mathbf{T}| \cos(\psi)\mathbf{e}_D \quad (4.4)$$

where  $\mathbf{e}_D$  is the unit vector in the downward direction,  $\mathbf{e}_v$  is the unit vector in the direction of the relative wind velocity,  $m$  is the mass of the craft,  $g$  is the acceleration due to gravity,  $-D$  is the drag force opposite of the relative wind velocity, and  $T_v$  and  $T_D$  are the thrust forces in the direction of the relative wind and the downward directions, respectively. Substituting these into Equation 4.1 and rearranging results in:

$$D\mathbf{e}_v + mg\mathbf{e}_D = |\mathbf{T}| \sin(\psi)\mathbf{e}_v + |\mathbf{T}| \cos(\psi)\mathbf{e}_D \quad (4.5)$$

Thus, we can say:

$$|\mathbf{T}| \sin(\psi) = D \quad (4.6)$$



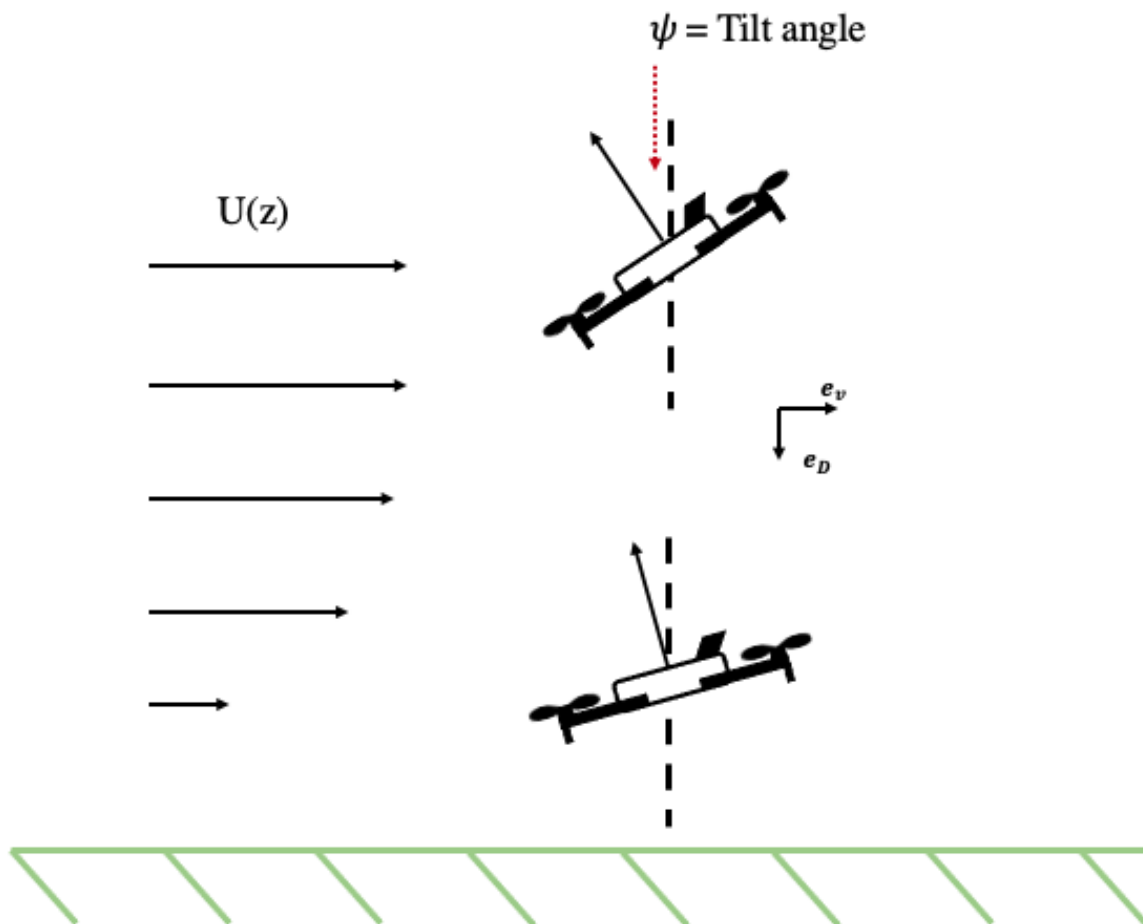


Figure 4.1: Cartoon depicting the coordinate system used to derive the wind speeds using the tilt angle of the CopterSonde. If the wind vane mode is active, the tilt angle  $\psi$  is simply the pitch of the aircraft. The unit vectors  $e_v$  and  $e_d$  describe the direction of the relative wind (assumed to be horizontal) and the direction of the gravity force, respectively.

$$|\mathbf{T}| \cos(\psi) = mg \quad (4.7)$$

Taking the ratio of these equations:

$$D = mg \tan(\psi) \quad (4.8)$$

Finally, we can use the Raleigh drag equation,

$$D = \frac{1}{2} C_D \rho A v^2 \quad (4.9)$$

to relate the drag force in Equation 4.8 to the wind velocity  $v$ , the coefficient of drag  $C_D$ , the air density  $\rho$ , and the cross-sectional area of the drone to the tilt angle of the craft:

$$v = \sqrt{\frac{2mg \tan(\psi)}{C_D \rho A}} \quad (4.10)$$

Unfortunately, many of the quantities in Equation 4.10 are difficult to calculate practically. For example, calculating the cross-sectional area  $A$  is complicated by the fact that the propellers are pseudo-permeable while spinning and are a function of the rotations-per-minute (González-Rocha et al. 2019). In order to simplify the calculation, Palomaki et al. (2017) proposed to simply lump all the difficult terms into a coefficient such that

$$v = C_0 \sqrt{\tan(\psi)} \quad (4.11)$$

where

$$C_0 = \sqrt{\frac{2mg}{C_D \rho A}} \quad (4.12)$$

Palomaki et al. (2017) found that by simply hovering next to an anemometer mounted on a 10 m tower and linearly relating the aircraft tilt to the wind speed

measured by this anemometer, the wind speed could be measured to an accuracy of approximately  $0.5 \text{ m s}^{-1}$  in calm environments (i.e., wind speed from  $0\text{-}5 \text{ m s}^{-1}$ ).

For the Flux Capacitor and LAPSE-RATE campaigns, the wind speed relationship was derived in a similar manner to Palomaki et al. (2017) in light to moderate winds ( $0\text{-}10 \text{ m s}^{-1}$ ) next to the Washington, Oklahoma Mesonet tower 10 m anemometer (see Greene 2018). Using this calibration method produced underestimations of the wind speed in both campaigns, but especially in the high winds observed during the Flux Capacitor campaign (Section 3.1). In the previous studies, commercial off-the-shelf UAS were used to test the linear fit. These UAS are not designed to handle wind speeds above approximately  $10 \text{ m s}^{-1}$ . However, the CopterSonde has been designed to be able to handle wind speeds up to approximately  $20 \text{ m s}^{-1}$  maximize the number of conditions in which it can safely fly to measure the ABL.

There are a few different factors that could explain the underestimates in the derived wind speed. First, the coefficients used to linearly relate the tilt of the craft to the wind speed were determined while the craft was *hovering*, but the CopterSonde *ascends* at a constant speed. In order to ascend, the CopterSonde must change its tilt to direct more thrust downward and create lift. Therefore, the craft tilt recorded while hovering and ascending are different, and the equation derived while hovering next to a tower is not valid. Another factor that may have affected the wind speed measurements is the density of the air in the LAPSE-RATE campaign. Finally, the simple linear fit used by Palomaki et al. (2017) may not be fully appropriate at higher wind speeds. At higher wind speeds, the cross-sectional area and drag coefficient cannot be assumed constant since the tilt of the aircraft becomes much larger.

In order to test the sensitivity of the wind measurements to these variables, data from a specific CopterSonde (tail number N955UA) used in both LAPSE-RATE and Flux Capacitor were used. This CopterSonde successfully flew 79 times between the two campaigns in a large range of wind conditions and with minimal changes in

hardware and software between campaigns, which means it is well suited for these tests. For the following examinations, the wind algorithm tested is “trained” on 10 randomly chosen flights (provided they cover an appropriately wide range of wind conditions), and then the algorithm is applied to the remainder of the data and compared to the DL in the same manner described in Chapter 3.

#### 4.1.1 Ascending vs Loiter

To analyze the impact of pitch while ascending, the most obvious test to begin with is an examination of how the pitch of the CopterSonde varies between a loiter and an ascending profile and the effect this has on the derived wind speed. Determining the linear coefficient in Equation 4.12 proves difficult to do while ascending using the tower methodology in Palomaki et al. (2017). Either a large tower is needed, or many “push-ups” (where the UAS rapidly ascends and descends around a specified height) need to be done next to the anemometer on the tower to build up a large enough dataset to perform the linear regression. Instead of using a tower, the Doppler lidar from CLAMPS1 that was co-located with the CopterSonde was used for these experiments.

Some considerations need to be made since the horizontal wind speeds measured by the Doppler lidar are calculated using the VAD method, which contains spatial averaging as opposed to a point measurement from an anemometer or from the CopterSonde. First, the CopterSonde data were vertically averaged to the vertical resolution of the VAD profiles. Next, only VADs that occurred when a CopterSonde was actively ascending were used to “train” the algorithms. Finally, strict quality control on flow homogeneity was applied to each vertical gate of the VAD. The degree of homogeneity of the flow as a function of  $z$  can be quantified using the coefficient of determination (Päschke et al. 2015):

$$R^2 = 1 - \frac{\sum_i (V_{ri} - \tilde{V}_{ri})^2}{\sum_i (V_{ri} - \bar{V}_r)^2} \quad (4.13)$$

with  $\bar{V}_r = \sum_i V_{ri}$  and  $\tilde{V}_{ri}$  being the radial velocities calculated from the least-square fit of the sine wave from the VAD. In practice, this is used as a way to filter out scans that do not sufficiently meet the requirements of the VAD. Päsche et al. (2015) found that having a value of  $R^2$  greater than .95 generally meant that the homogeneity condition was satisfied enough to get a decent retrieval using a VAD. However, for training the following algorithms, a higher threshold of .99 was used to ensure invalid assumptions do not affect the results of the training. Note all the same filtering is applied to the following sections as well.

Figure 4.2 shows the data from CopterSonde N955UA using the original linear coefficients derived using tower data compared to the Doppler lidar data from CLAMPS. As shown in Figure 3.1, the CopterSonde tends to underestimate the wind speed, especially at higher wind speeds, with a mean difference of  $.759 \text{ m s}^{-1}$ . Figure 4.3 shows CopterSonde wind estimates using the same type of linear relationship, however, the linear coefficient was determined while the CopterSonde was ascending using the previously described methodology to relate the wind speed to  $\sqrt{\tan(\psi)}$ . It is immediately apparent that the mean bias the CopterSonde showed before is eliminated, however, the 2D histogram still shows that the CopterSonde is underestimating wind speeds higher than  $\sim 15 \text{ m s}^{-1}$ .

#### 4.1.2 Density correction

One of the advantages of the OU CopterSonde over UAS used in previous studies is more accurate thermodynamic measurements. This allows the density parameter to be extracted from  $C_0$  and directly calculated from the thermodynamic data, allowing one to estimate  $v$  using:

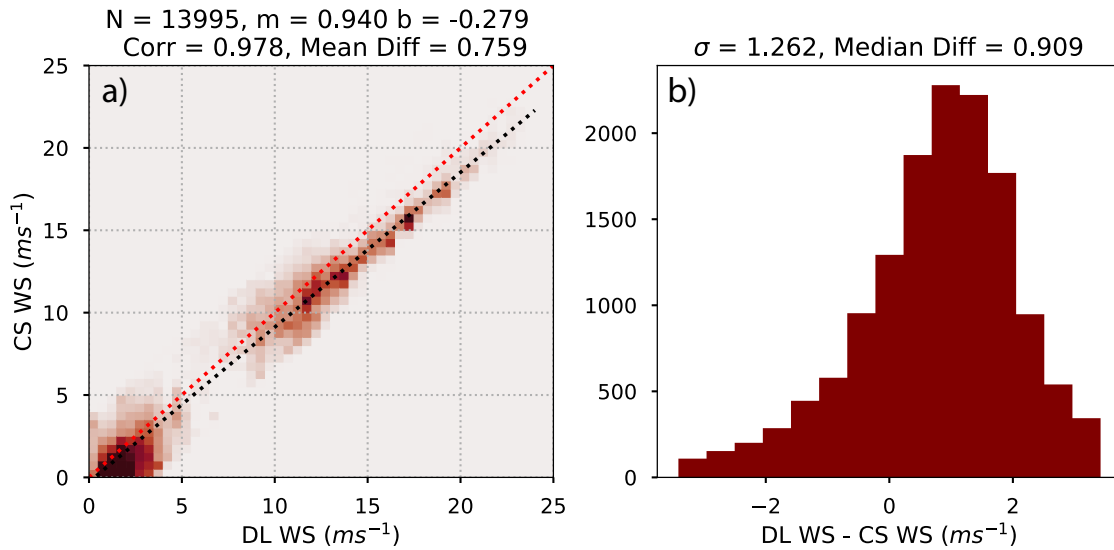


Figure 4.2: Two-dimensional histograms of DL-measured wind speed vs CopterSonde measured wind speed (a) using the linear coefficient derived by hovering next to the WASH Mesonet tower. The 2D histogram is binned to  $0.5 \text{ ms}^{-1}$  for wind speed. The histogram on the right shows the difference in wind speed between the DL and the CopterSonde(b). The red dotted line in (a) indicates the 1-to-1 line and the black dotted line indicates the least-squares regression. The slope (m) and intercept (b) are shown in the title. Various other statistics are also shown in the titles. N corresponds to the number of points, Corr is the Pearson correlation, Mean Diff is the mean difference between the CopterSonde and the DL,  $\sigma$  is the standard deviation of the differences, and Median Diff is the median difference between the CopterSonde and the DL.

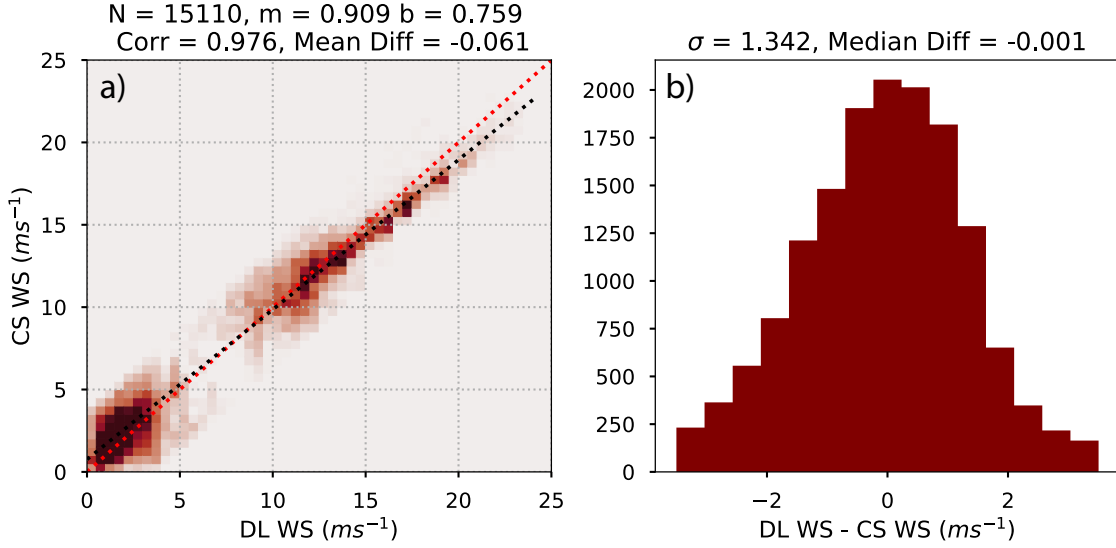


Figure 4.3: Similar to Figure 4.2, except that the wind speed coefficients were generated using observations from the DL while the CopterSonde was ascending.

$$v = C_1 \sqrt{\tan(\psi)/\rho} \quad (4.14)$$

where

$$C_1 = \sqrt{\frac{2mg}{C_D A}} \quad (4.15)$$

This density correction may be needed due to the large difference in elevations between the LAPSE-RATE and Flux Capacitor campaign, given Moffat, CO is located 2038 m above sea level while KAEFS is located 348 m above sea level. However, adding in this correction to the ascending profiles resulted in minimal changes to the overall result (Figure 4.4). In fact, in some metrics, it made the wind estimates worse when compared to the Doppler lidar (e.g., the median difference and the standard deviation of the differences).

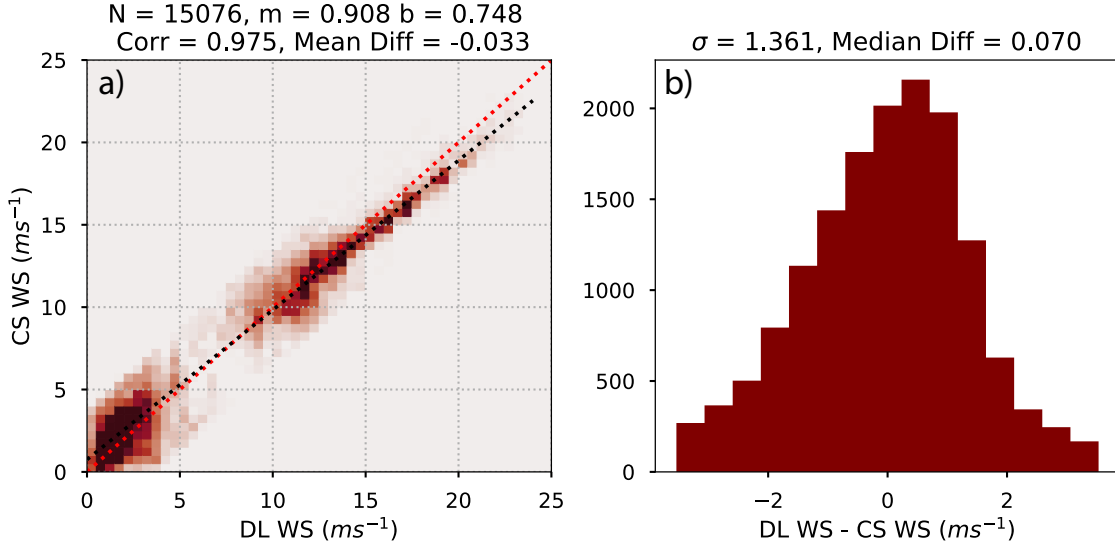


Figure 4.4: Similar to Figure 4.2, except that the wind speed coefficients were generated using observations from the DL while the CopterSonde was ascending and with the density correction applied.

#### 4.1.3 Non-linear fits

Despite being calibrated on the full envelope of possible wind speeds for the CopterSonde, the linear fit still exhibited bias at higher wind speeds (Figure 4.2 and 4.4). This begs the question of whether a linear fit is appropriate for  $\sqrt{\tan(\psi)}$ . One reason for the discrepancy is that  $C_D$  and  $A$  likely cannot be treated as constant inside of  $C_0$  or  $C_1$ . One of the assumptions that went into the wind estimation method described by Palomaki et al. (2017) is the tilt angles are relatively small. In the case of the CopterSonde, the pitch can easily be  $>20^\circ$ . To address this, a more complex function needs to be introduced to provide higher accuracy at larger tilt angles. González-Rocha et al. (2019) note that in wind-tunnel experiments, drag was found to vary approximately linearly with pitch angle. Thus, we can introduce a linear function into Equation 4.13 for  $C_D$ :



$$D^* = \frac{1}{2}(\alpha\psi + \beta)\rho Av^2 \quad (4.16)$$

resulting in:

$$v^* = \sqrt{\frac{2mg \tan(\psi)}{(\alpha\psi + \beta)\rho A}} \quad (4.17)$$

Rather than simplifying this and treating  $\sqrt{\tan(\psi)}$  as the independent variable, this function can be optimized using non-linear least squares to get  $\alpha$ ,  $\beta$ , and  $A$ . Using the same training data as before, and using SciPy’s non-linear least squares function (Virtanen et al. 2020), results in the wind speeds shown in Figure 4.5

This new function and type of fit produces near zero mean and median bias, which is very promising. The coefficients determined for this comparison do cause some over estimation at the highest wind speeds, but this could be improved by using more data in the fit. More data has not been included here in order to have as many independent comparisons as possible to the Doppler lidar.

## 4.2 Thermodynamic Retrievals

The thermodynamic profilers (and profilers in general) have an advantage over Wx-UAS in the sense that they continuously record data, and thus provide higher temporal resolution data. However, they are often reliant on outside data sources to retrieve the atmospheric state, whether that be a large climatology of observations or model data, or additional in situ/remote-sensing data. The TROPoe retrievals from LAPSE-RATE may have performed poorly, especially in the moisture field (Section 3.1.1), due to the lack of an appropriate data source from which to build a prior dataset ( $\mathbf{X}_a$  and  $\mathbf{S}_a$ ). In previous work, the prior has been thought to have minimal impact on the resulting thermodynamic profile (Turner and Löhnert 2014). However, this study focused on retrieval convergence rather than retrieval accuracy.

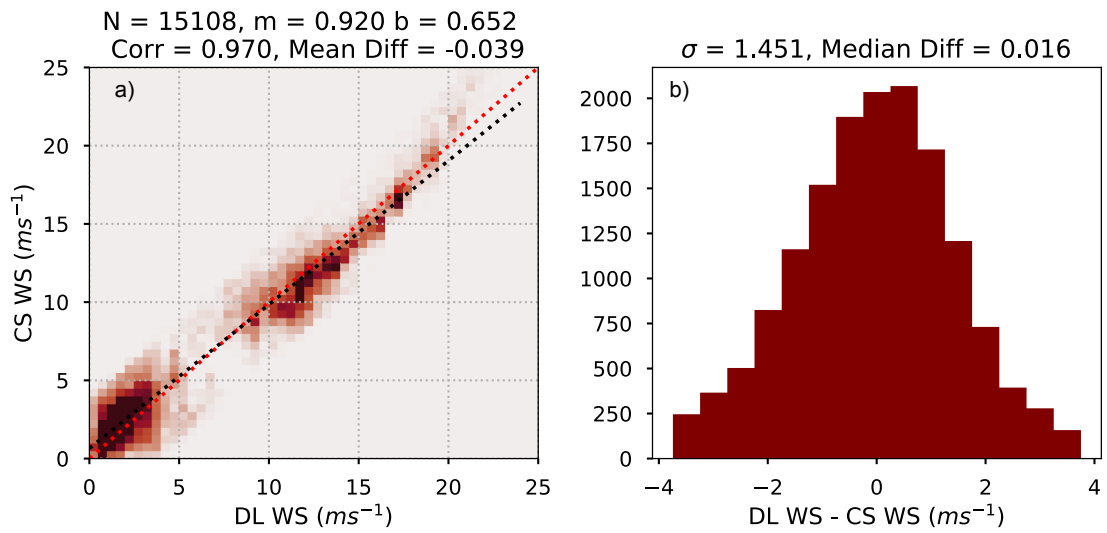


Figure 4.5: Similar to Figure 4.2, except that the wind speed coefficients were calculated using DL observations when the CopterSonde was ascending and with a non-linear fit.

In the following sections, the sensitivity of TROPoe is tested using CLAMPS data collected during the 2017 VORTEX-SE field season. In addition to examining the impact of the prior, two parameters are examined for sensitivity as well based on patterns seen in the LAPSE-RATE data. Following that analysis, CopterSonde data is used to help further constrain the retrievals from LAPSE-RATE and examine the impact low-level WxUAS observations have on the TROPoe retrieval system.

#### **4.2.1 Examining the effect of the prior during VORTEX-SE**

In order to test the impact of the prior on the resulting retrieval in a relative sense, a slightly less topographically complex dataset, one with different thermodynamic regimes, was used to test the sensitivity of TROPoe to the prior. AERI data from the 2017 VORTEX-SE campaign (Section 2.1) were processed using two different prior datasets: one created from archived radiosondes launched from the Southern Great Plains (SGP) atmospheric observatory established by the Atmospheric Radiation Measurement (ARM) user facility in northern Oklahoma, and one using radiosondes launched by the Birmingham, Alabama NWS office (BMX). The data used are from April 2017 while CLAMPS2 was deployed near Scottsboro, AL. This time period contained a nearly continuous dataset of high quality observations.

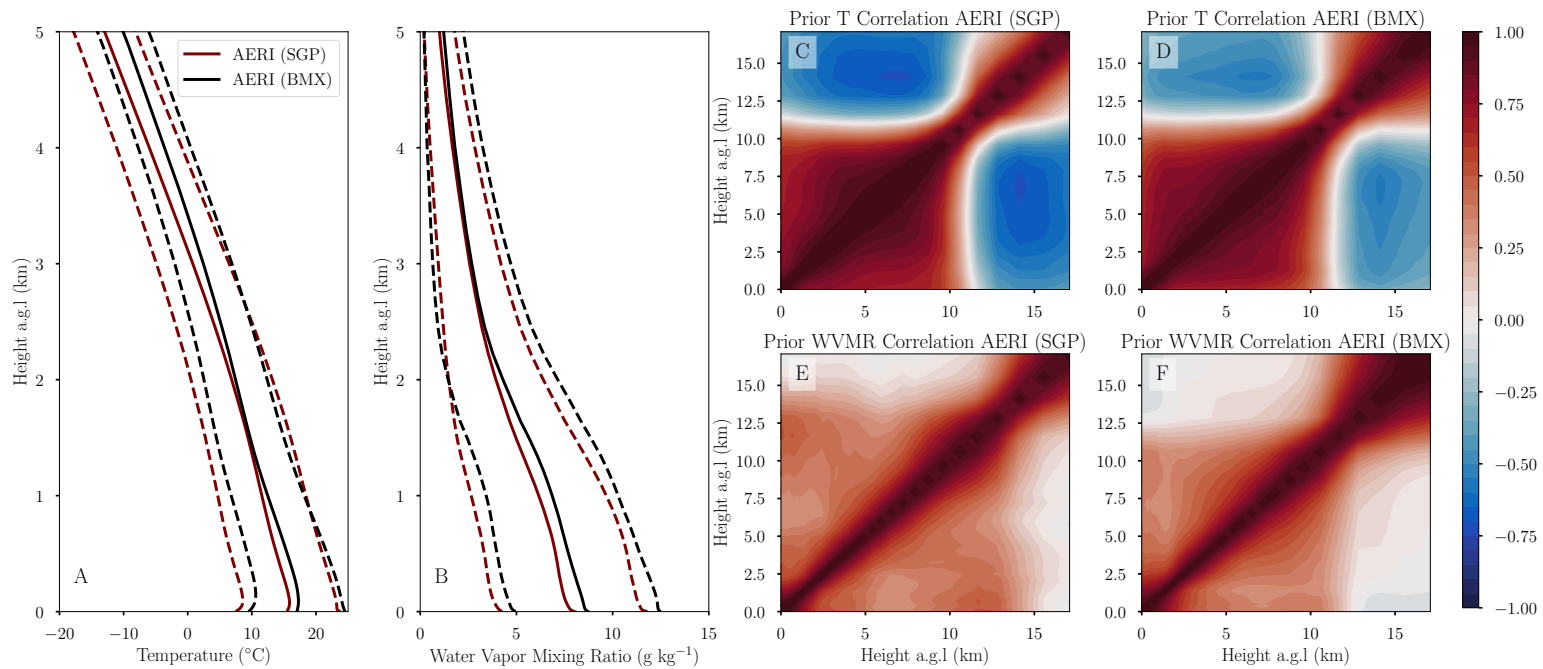


Figure 4.6: This figure illustrates the differences between the prior created from the BMX radiosonde archive and the SGP radiosonde archive. Panels A and B show the temperature and water vapor mixing ratio profiles, respectively, for the SGP (red, solid) and BMX (black, solid) priors. The dashed lines denote one standard deviation from the climatology. Panels C and D are the prior temperature correlation matrices for the SGP and BMX prior, respectively, while panels E and F are the prior water vapor mixing ratio correlation matrices.

Figure 4.6 shows a comparison between the SGP and BMX priors. The profiles show the mean temperature and water vapor mixing ratio (Figure 4.6A and B, respectively) and their  $1\text{-}\sigma$  uncertainty range. This uncertainty is determined by taking the square-root of the diagonal of  $\mathbf{S}_a$  in Equation 1.3. Overall, the BMX prior is slightly warmer (2–3 °C below 1 km, with slightly larger differences above 5 km) and moister (approximately  $1\text{ g kg}^{-1}$  below 2 km) than the SGP prior. The uncertainties appear to be approximately the same.

It is also important to look at the correlation matrices from each prior since they give insights into how the retrieval may behave. Since the information content of the AERI drops off rapidly with height, the retrieval relies on these correlations and the outside model profiles to determine how to adjust the middle and upper troposphere. Thus, their structure could have an impact on the retrieval.

Figure 4.6C and E shows the level-to-level correlation for SGP temperature and water vapor mixing ratio, respectively, while Figure 4.6D and F shows the level-to-level correlation for BMX temperature and water vapor mixing ratio, respectively. The temperature correlations between SGP (Figure 4.6C) and BMX (Figure 4.6D) have few differences. Above the tropopause (approximately 11.5–12 km; generally indicated by the area where correlations go from strongly positive to negative), temperature is slightly less anti-correlated with the middle troposphere. However, the rough pattern remains similar. In the water vapor field, there are some slight differences to the structure of the correlation matrix. The SGP prior has positive correlations extending above the tropopause for water vapor (Figure 4.6E), whereas the BMX prior does not have these positive correlations of water vapor above the tropopause (Figure 4.6F); rather the dropoff of positive correlation is rather sharp.

Figure 4.7 shows the average differences between the temperature (A) and water vapor mixing ratio fields (B) between the AERI retrievals using the SGP and BMX priors. Only the lowest two kilometers are shown since this is the region where the

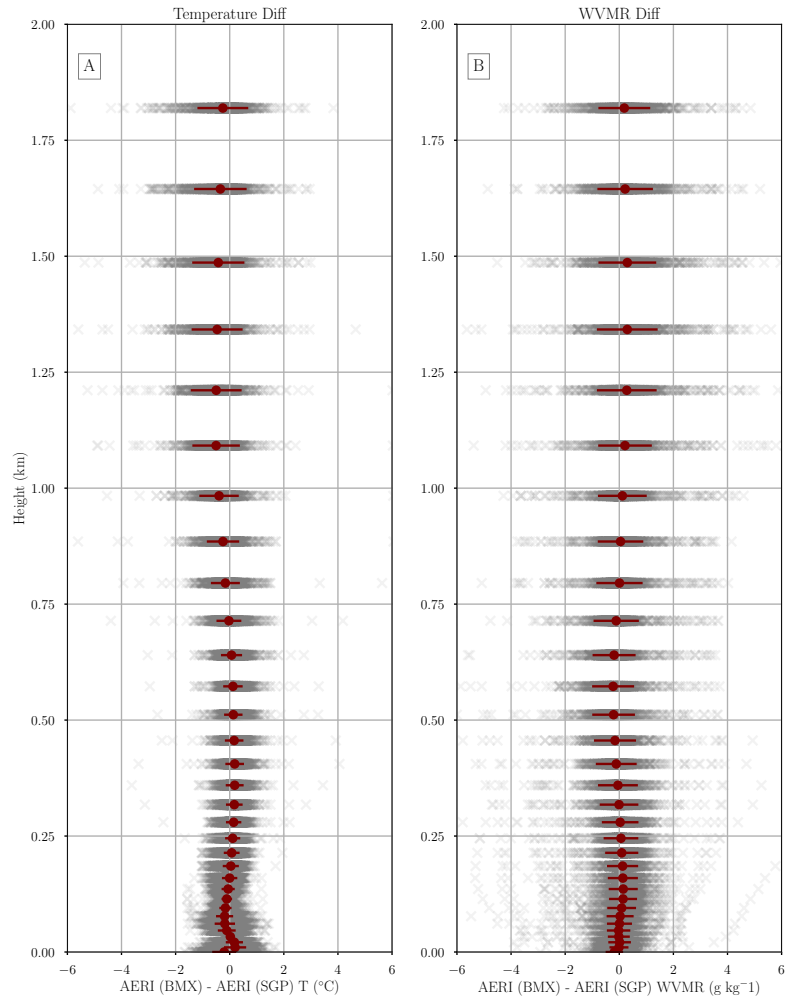


Figure 4.7: Profile of the differences between the SGP retrieval and BMX retrieval for temperature (a) and water vapor mixing ratio (b) values at each retrieved level. The red points show the mean difference while the gray points are the individual differences. The errorbars indicate the standard deviation of the differences.

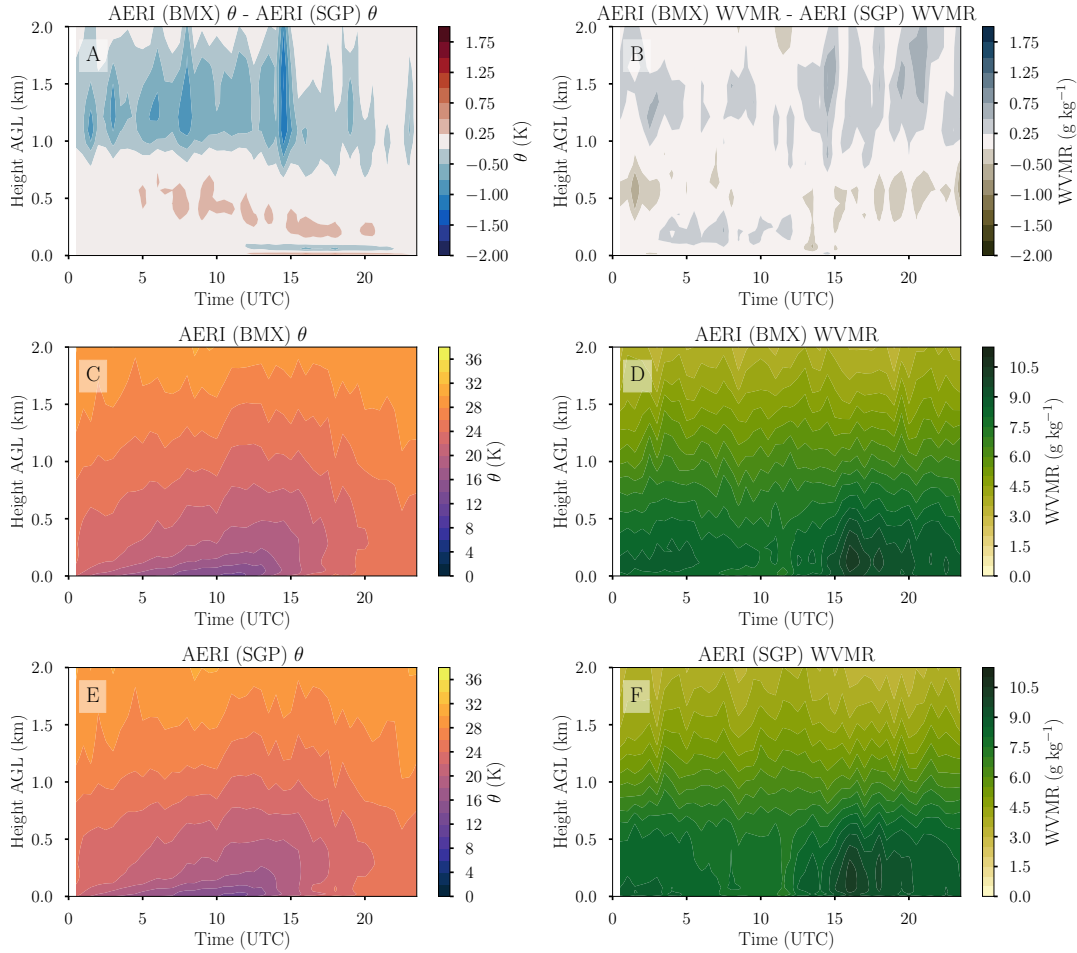


Figure 4.8: Mean difference of potential temperature (A) and water vapor mixing ratio (B) shown in a time–height cross-section comparing the BMX retrieval to SGP retrievals. The mean potential temperature and water vapor mixing ratio from the same period, respectively, are shown in C and D for the BMX retrieval and E and F for the SGP retrievals

AERI observations have the most information content. On average, the BMX prior is approximately 0.5–1 °C cooler above 1 km (Figure 4.7A). Interestingly, there appears to be a sort of inflection point in the lowest approximately 100 m of temperature retrievals. One of the retrievals struggles to capture the proper lapse-rates in this area of the profile. The moisture field does not exhibit the same pattern in the low levels (Figure 4.7B).

Figure 4.8 shows composite differences of potential temperature and water vapor mixing ratio as a function of time and height (A and B), as well as the composites of the individual retrievals (C–F). These figures show if there is a temporal variation to the differences between the retrievals using the SGP and BMX priors. Typically, the relative warmth of the SGP prior between 1 and 2 km shown in Figure 4.7 occurs primarily in the overnight period. The signal seen in the lowest 200 m also appears to occur primarily during the daylight hours (Figure 4.8A) between approximately 12Z and 13Z. The differences in water vapor mixing ratio (Figure 4.8B) do not appear to follow any diurnal pattern.

Using the time-height composites allows a time to be extracted where the low-level-temperature feature is present. Figure 4.9 shows the mean temperature profile extracted at 18Z. Here we see that the SGP prior is the culprit of the low level signal. It is displaying uncharacteristic lapse rates in the lowest 100 m, most notably the extreme superadiabatic lapse rate in the lowest 30 m and statically stable layer from 30 m to 70 m.

Based on this analysis, the prior does appear to impact the retrievals in this case. While there is no verification data available, there are obvious patterns that are undesirable in the retrievals using the SGP prior. Very near-surface superadiabatic layers could erroneously initiate convection in models or mislead forecasters. The next section examines a physical parameter in the retrieval that is related to how



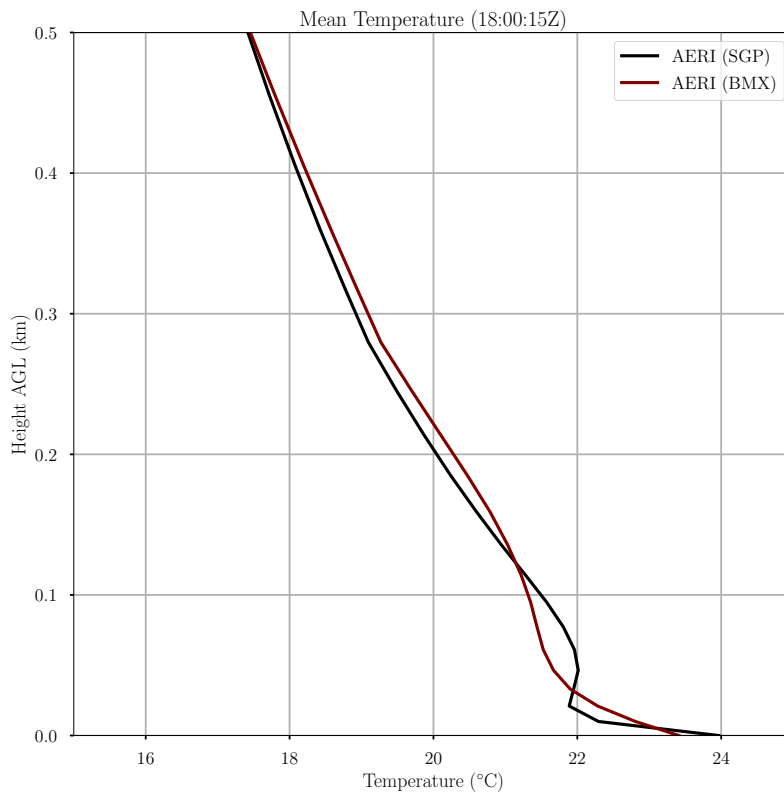


Figure 4.9: Composite temperature profiles from VORTEX-SE during April 2017 at 18Z using the SGP (black) and BMX (red) prior dataset.

the retrieval handles superadiabatic layers and explores its effect on the retrievals calculated with both the SGP and BMX priors.

#### 4.2.1.1 Superadiabatic max height

TROPoe contains numerous physical constraints in order to limit the number of possible solutions that may be produced. One of these is that the potential temperature must monotonically increase above a specified height. Below this, the retrieval is allowed to be superadiabatic in order to capture the shallow superadiabatic layer that often forms near the surface. Typically, this height is kept at 300 m based on trial and error using an SGP-based dataset (upon close inspection of Figure 4.9, the effect of this parameter can be seen by the slight kink in the profiles around 0.3 km). However, the sensitivity of TROPoe to this parameter has never been tested in another location. It was hypothesized that the superadiabatic max height could be different in the SE US, and a more accurate estimate could have an effect on the retrievals.

In order to examine the sensitivity of the retrieval to this parameter, the radiosonde datasets used to calculate the prior were utilized to determine an appropriate value for the superadiabatic max height. It should be noted that the NWS radiosonde datasets that are publicly available *are not ideal* for this purpose since they often only have a few points in the boundary layer. However, since there is no other long-term, high-resolution dataset, they will be sufficient for some a first exploration into the sensitivity of TROPoe to this parameter.

Superadiabatic layers were found by calculating potential temperature and finding layers where it decreases between two levels (this is the same methodology used for the physical constraint mentioned before). In order to attempt to account for artificially deep superadiabatic layers due to low-resolution data, a small threshold  $.05\text{ }^{\circ}\text{C}$  for the potential temperature difference between the two layers of was applied and

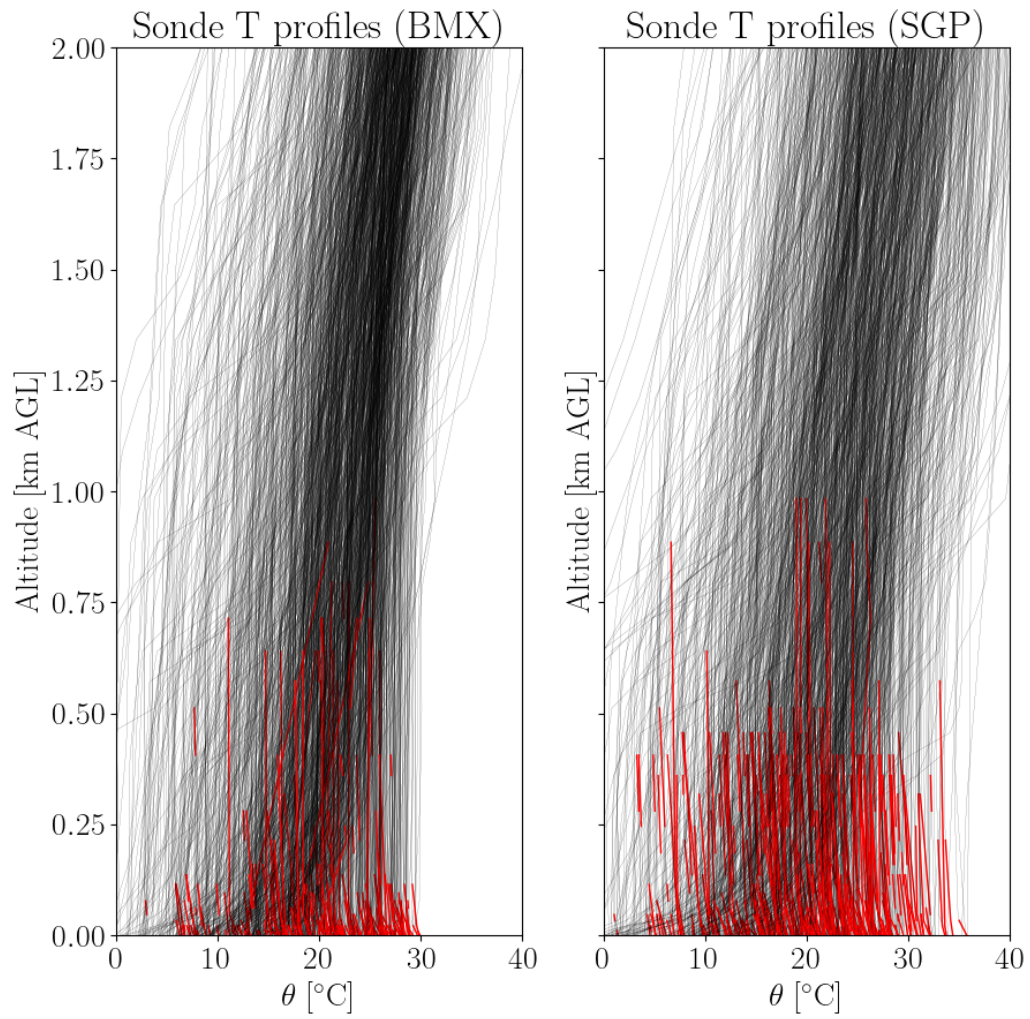


Figure 4.10: Potential temperatures (black) of all the radiosondes used in the BMX prior (left) and the SGP prior (right). Superadiabatic layers are colored red.

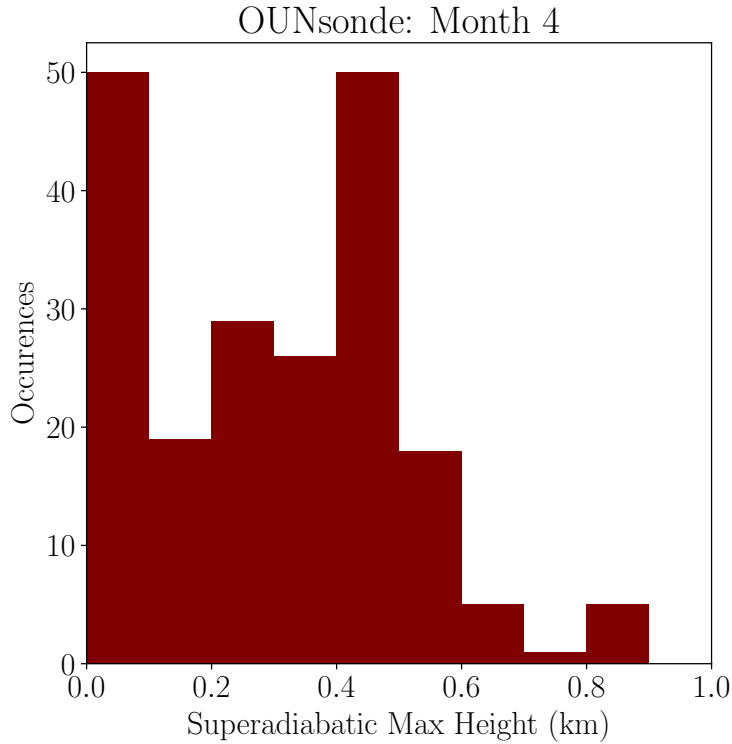


Figure 4.11: Histogram of superadiabatic max heights identified in the the SGP prior. The bars are binned every 100 m.

maximum heights were limited to 1 km. Figure 4.10 shows the individual superadiabatic layers. The SGP radiosondes displayed a superadiabatic layer in approximately 18% of the soundings while the BMX radiosondes displayed superadiabatic layers in approximately 10% of the soundings. Figure 4.11 and 4.12 show histograms of the maximum superadiabatic height from the SGP and BMX datasets, respectively. The SGP dataset shows more of a bi-modal distribution (Figure 4.11) with relative maxima between 0–0.1 km and 0.4–0.5 km. The median maximum superadiabatic height is 0.33 km, which is close to the default value in TROPoe. The BMX dataset (Figure 4.12) is largely concentrated in the first 0.1 km. The median value is .13 km. Thus there is enough difference between SGP and BMX to warrant testing the impact the superadiabatic max height parameter has on the retrieval

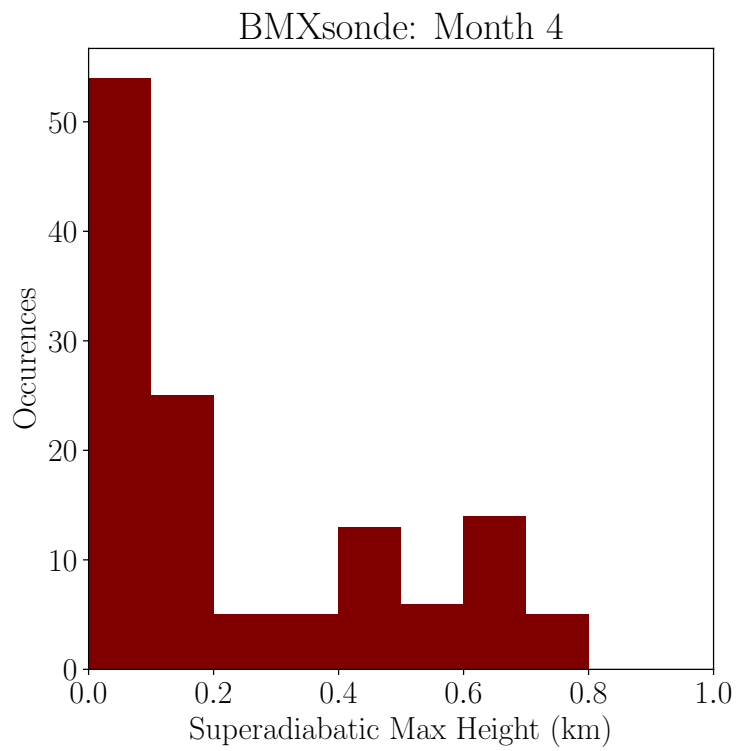


Figure 4.12: Histogram of superadiabatic max heights identified in the the BMX prior. The bars are binned every 100 m.

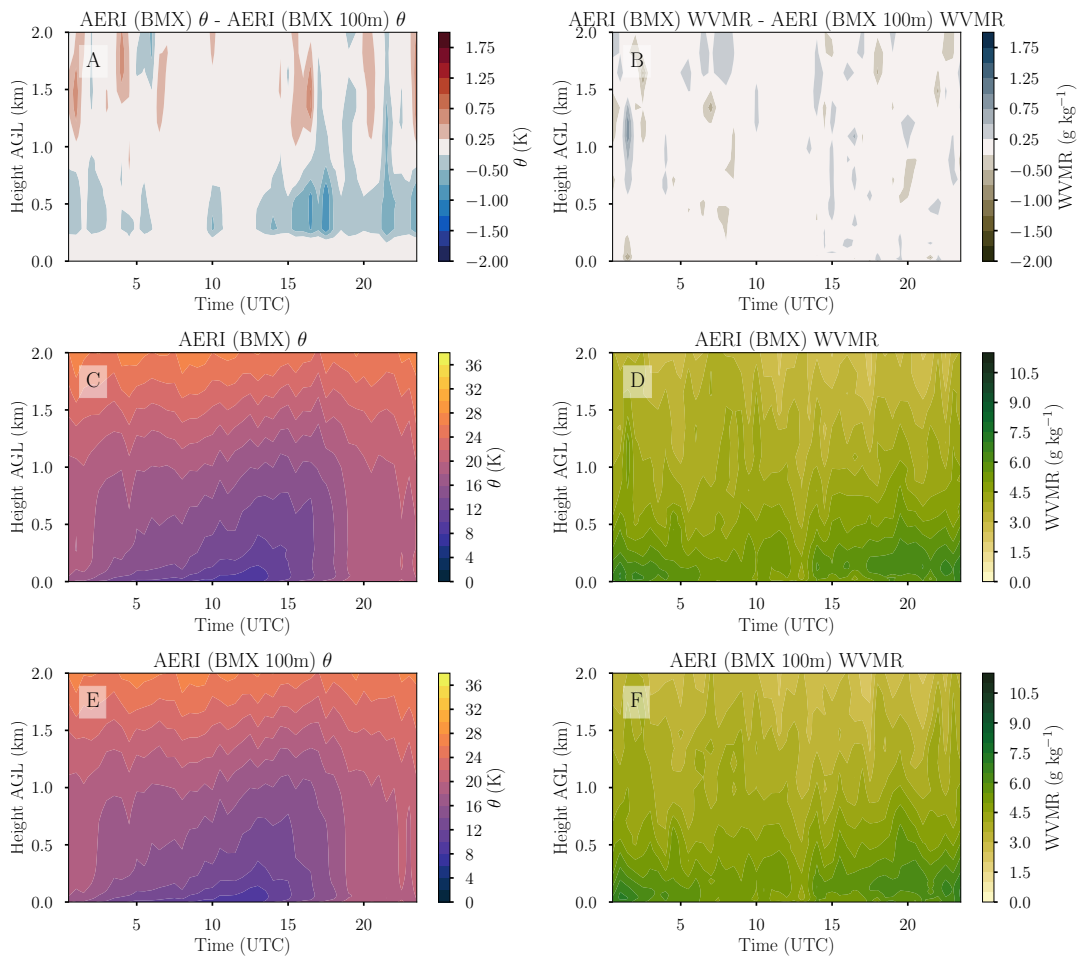


Figure 4.13: Similar to Figure 4.8, except comparing the retrievals using with a maximum superadiabatic height of 300 m (C, D) and with a maximum superadiabatic height of 100 m (E, F).

Figure 4.13 shows the time-height composites of potential temperature and water vapor mixing ratio of the default BMX retrievals with a superadiabatic maximum height of 300 m compared to the same time period using a 100-m superadiabatic maximum height (based on the radiosonde analysis). Overall, there continues to be relatively minimal difference in water vapor mixing ratio (Figure 4.13B). However, the BMX 100 m run is, on average, warmer than the control run from 300 m to 900 m during the daytime hours (Figure 4.13A). This is to be expected given the physical constraint of monotonically increasing potential temperature above the maximum superadiabatic height. Looking at the overall difference profile (Figure 4.14), mean differences are generally less than 1 °C, with a standard deviation of approximately 1 °C above .25 km. However, some individual profiles exhibit large variations between the two retrievals.

#### **4.2.2 Impact of using WxUAS**

Now, given it has been established that the prior is important to achieve accurate results in TROPoe, it is possible to revisit the LAPSE-RATE retrievals and see if there is a way to improve them. Given TROPoe is able to easily ingest observations from other platforms, additional constraints will likely help to improve the resulting retrievals. Using radiosonde data has already been shown to improve the retrievals in other field campaigns, but since radiosondes are a relatively slow profiling method (even when they are rapidly released), radiosonde data are only used above 3–4 km. This allows the instantaneous AERI and/or MWR data to provide the low level information where the atmosphere changes on quicker time scales, while the radiosonde only constrains the upper levels where the AERI has little information. Using the high-temporal resolution WxUAS data from LAPSE-RATE provides an opportunity to examine the impact of including these low-level observations to the retrieval.

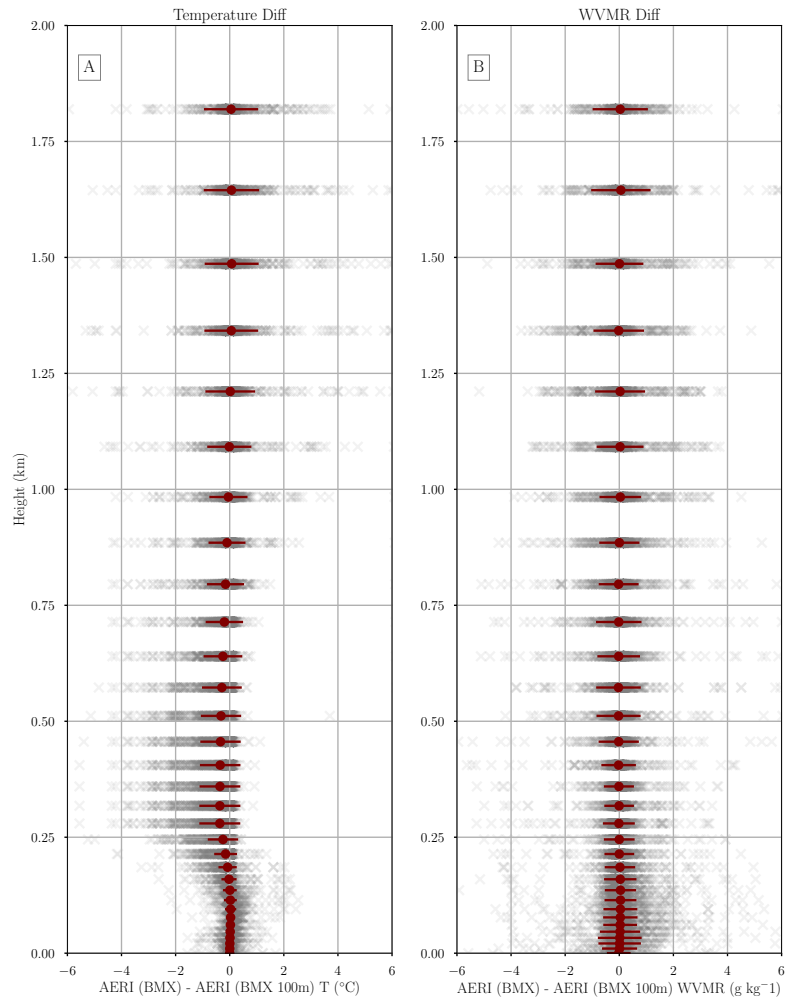


Figure 4.14: Profile of the differences between the base BMX retrieval and BMX retrieval with the superadiabatic max height set to 100 m for temperature (a) and water vapor mixing ratio (b) values at each retrieved level. The red points show the mean difference while the gray points are the individual differences. The errorbars indicate the standard deviation of the differences.



It is important to accurately specify the uncertainty of the WxUAS observation used. While the remote sensors and radiosondes presented in Chapter 3 have been characterized by previous studies, the CopterSonde is a relatively new platform. Thus we present specifications of the uncertainty in CopterSonde measurements when statistically compared to the RS92-SGP radiosonde in Table 4.1. These were determined from the standard deviations of the differences calculated from the intercomparisons during LAPSE-RATE and Flux Capacitor (Chapter 3). For completeness, the kinematic uncertainties are also included. Note that the wind speed and direction uncertainties were determined using data with wind speeds greater than  $4 \text{ m s}^{-1}$ .

Table 4.1: Summary of CopterSonde measurement specifications based on the results of this study when compared to the Vaisala RS92-SGP data used in Chapter 3

CopterSonde 2.5 Specifications	
Temperature	$\pm 0.5 \text{ }^\circ\text{C}$
Water vapor mixing ratio	$\pm 1 \text{ g kg}^{-1}$
Horizontal wind speed	$\pm 0.6 \text{ m s}^{-1}$ (in speeds $> 4 \text{ m s}^{-1}$ )
Horizontal wind direction	$\pm 4 \text{ }^\circ$ (in speeds $> 4 \text{ m s}^{-1}$ )

The LAPSE-RATE AERI data were reprocessed through TROPoe to confirm that the same patterns were observed between TROPoe and the original AERIOe retrievals shown in Chapter 3. Additionally, MWR data were also processed with TROPoe to determine the impact of low-level WxUAS data on MWR-only retrievals. Figure 4.15 shows the TROPoe results of AERI-only temperature and water vapor mixing ratio retrievals compared to the radiosondes launched during LAPSE-RATE. This is analogous to Figure 3.7 of the AERIOe retrievals, only excluding data from Flux Capacitor and using data up to 4 km, instead of the max height of the CopterSondes. The cut-off height of 4 km was chosen since RAP data are used to constrain the retrieval above this height. The following results are summarized in the Appendix

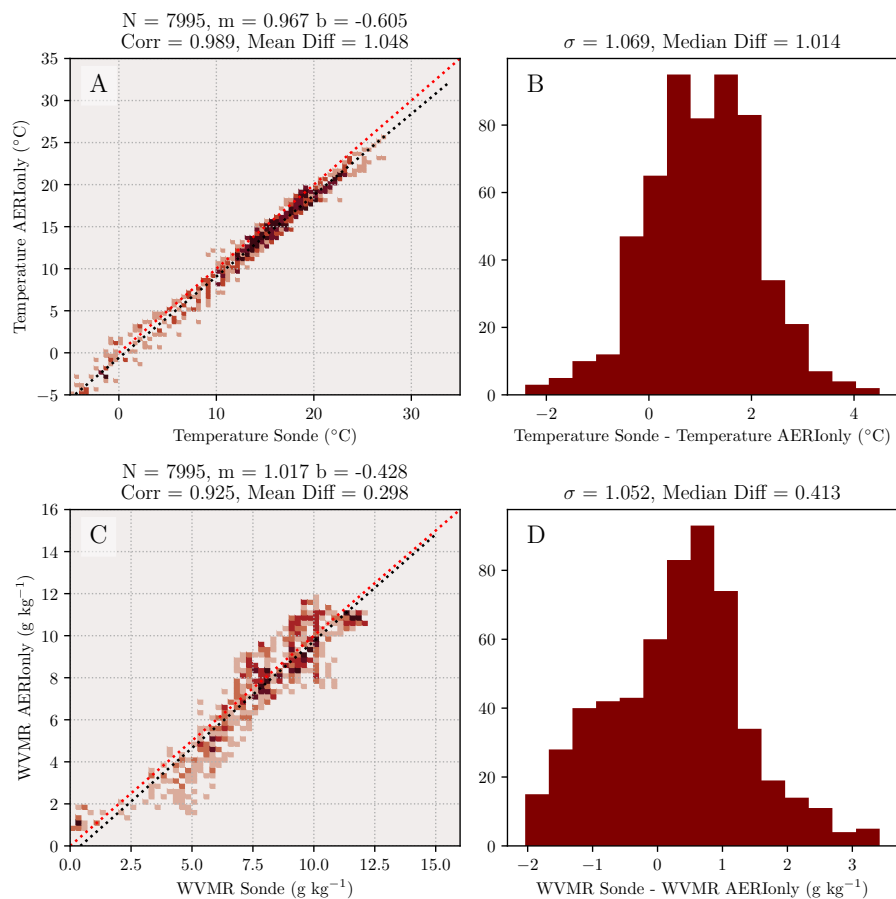


Figure 4.15: Two-dimensional histograms of AERI-only retrievals vs radiosonde measured temperature (A) and AERI-only retrieval water vapor mixing ratio vs radiosonde measured water vapor mixing ratio (C). The 2D histograms are binned to  $0.5\text{ }^{\circ}\text{C}$  for temperature and  $0.25\text{ g kg}^{-1}$  water vapor mixing ratio. The histograms on the right show the difference in temperature (B) and water vapor mixing ratio (D). The red dotted line is the 1-to-1 line and the black line is the least-squares regression. The slope ( $m$ ) and intercept ( $b$ ) are shown in the title. Various other statistics are also shown in the titles.  $N$  corresponds to the number of points,  $\text{Corr}$  is the Pearson correlation,  $\text{mean diff}$  is the mean difference between the AERI-only and the radiosonde,  $\sigma$  is the standard deviation of the differences, and  $\text{median diff}$  is the median difference between the radiosonde and the retrieval.

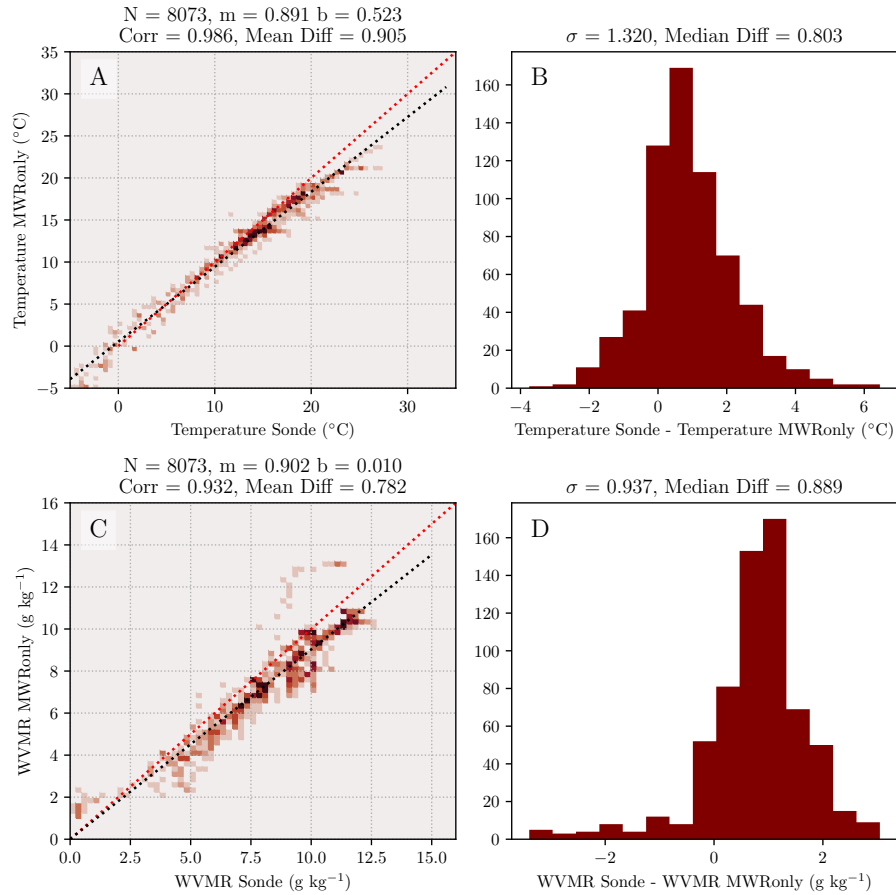


Figure 4.16: Similar to Figure 4.15, except for MWRonly temperature (A, B) and water vapor mixing ratio (C, D) retrievals.

in Table A.1. As seen before, temperature estimates from the AERI are slightly cooler than those measured by the radiosonde, on average, with a mean and median difference of 1 °C (Figure 4.15A and B). The correlation between the temperature measurements remains high at 0.99 (Figure 4.15A). The water vapor mixing ratio measurements also display similar patterns as before, namely the AERI retrievals are slightly drier than measurements from the radiosonde (Figure 4.15D).

Figure 4.16 shows the MWR-only TROPoe retrievals compared to radiosondes from LAPSE-RATE. The MWR-only retrievals exhibit similar patterns to the AERI-only retrievals. The MWR retrievals are approximately  $.9\text{ }^{\circ}\text{C}$  cooler on average compared to the radiosonde (Figure 4.16A) with a higher standard deviation on differences compared to the AERI-only retrievals (Figure 4.16B). Again, the water vapor mixing ratio is on average lower than the radiosonde measurements, with a mean difference of  $0.78\text{ g kg}^{-1}$ . This is higher than the AERI-only retrieval, which could be due to the MWR being less sensitive to water vapor. Curiously, the standard deviation is lower on the MWR-only retrievals than the AERI-only retrievals (Figure 4.16D), though this could be due to the relatively small sample size.

To examine the impact of the CopterSonde data on the retrieval, CopterSonde profiles were included in the observation vector and treated in the same way as radiosondes or model data are in the upper levels. The profiles are interpolated to the retrieval levels and then each level is interpolated in time to match the AERI/MWR retrieval times. Typically, radiosondes are not extrapolated out any further than 1 hour before or after the profile time. Since the CopterSondes launched much faster than radiosondes, this maximum extrapolation time was set to 30 minutes, which was the slowest launch cadence used during LAPSE-RATE. Recall, the maximum allowable height for CopterSonde profiles during the campaign was 910 m.

Figure 4.17 shows the impact of adding the CopterSonde data to the observation vector,  $\mathbf{Y}$ . The mean temperature bias is reduced by only  $0.05\text{ }^{\circ}\text{C}$  and the standard deviation of the differences decreases by  $0.02\text{ }^{\circ}\text{C}$  (Figure 4.17A and B). The water vapor mixing ratio shows more mixed results. The mean difference between the retrieval and radiosonde increases by approximately  $0.2\text{ g kg}^{-1}$  (Figure 4.17C), while the standard deviation reduces by  $.25\text{ g kg}^{-1}$  (Figure 4.17D). Looking at the histogram of differences of the AERI+CopterSonde retrievals (Figure 4.17D) compared to the

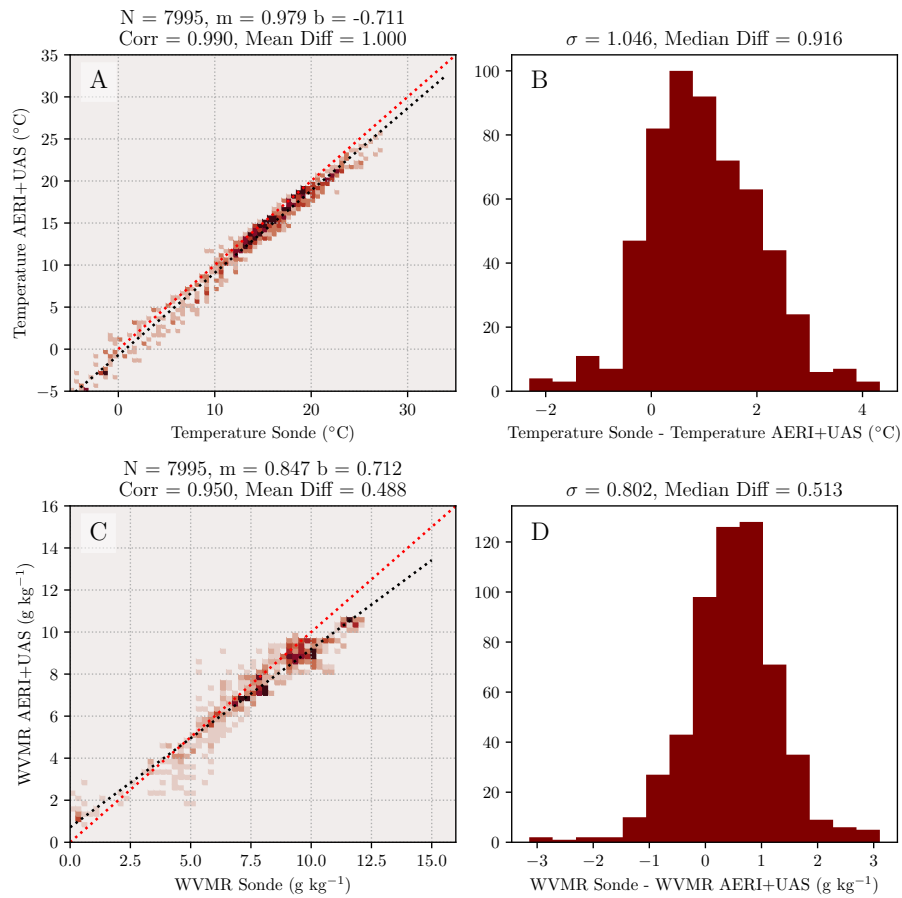


Figure 4.17: Similar to Figure 4.15, except for AERI+UAS temperature (A, B) and water vapor mixing ratio (C, D) retrievals.

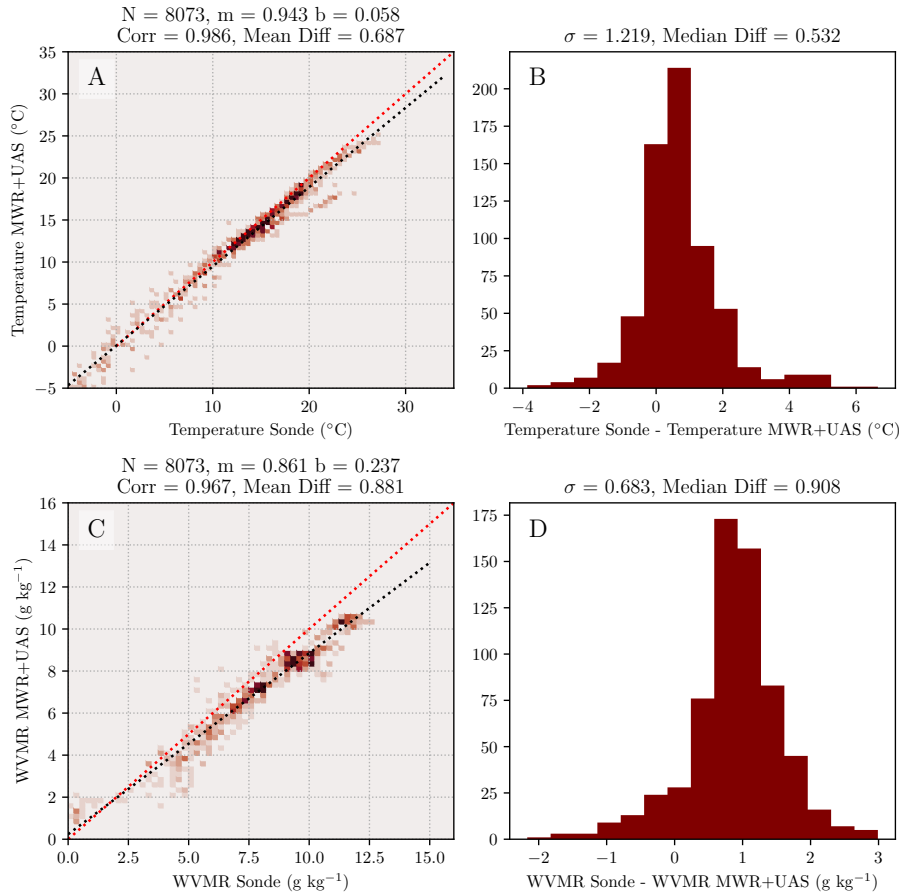


Figure 4.18: Similar to Figure 4.15, except for MWR+UAS temperature (A, B) and water vapor mixing ratio (C, D) retrievals.

AERIonly retrievals (Figure 4.15D), it appears the addition of the UAS made the differences follow a more Gaussian distribution.

The MWR+UAS retrievals show similar improvements to the AERI+UAS retrievals (Figure 4.18). The mean and median difference in temperature both decrease by approximately 0.3 °C (Figure 4.18A) and the standard deviation is reduced by 0.1 °C (Figure 4.18B). The water vapor measurements again show the same pattern as the AERI+UAS retrievals where the mean difference increases (Figure 4.18C) and the standard deviation decreases (Figure 4.18D). Given the recurrence of this pattern, it possible that the CopterSondes are the source of the moisture differences

discussed in Section 3.1.2, though it is still difficult to determine the true source of the differences in moisture between the radiosonde and the CopterSonde. However, the decreased standard deviation likely means the addition of low-level CopterSonde data can reduce retrieval uncertainty even at levels above where the CopterSonde is not able to fly.

There are a couple ways to examine this hypothesis. One way is to calculate the posterior correlation matrices. Figure 4.19 shows the comparison of the AERIonly correlation matrices for temperature and water vapor mixing ratio for a selected time that is representative of the whole dataset. The ideal posterior correlation matrix is an identity matrix; in other words, the off-diagonal components are all zero. The off-diagonal, level-to-level correlations for the AERI+UAS retrieval (Figure 4.19C) are slightly improved compared to the AERIonly temperature retrievals (4.19A). The improvements in the temperature correlation matrix are primarily concentrated in the lowest 1 km where the CopterSondes were flying. In terms of water vapor, again, most improvements are concentrated in the lowest 1 km (Figure 4.19D), with not much improvement in level-to-level correlation above. In fact, Figure 4.19D has a remarkably similar shape to Figure 3d in Smith et al. (2021) where WVDIAL were included in the retrieval.

In addition to the correlation matrices, the retrieval uncertainty can be examined by looking at the posterior covariance matrix. By taking the square-root of the diagonal, the standard deviation uncertainty of the retrieval with height can be examined. Using the same representative retrieval as in Figure 4.19, Figure 4.20 shows the 1-sigma uncertainty of the AERIonly and AERI+UAS retrieval. As seen in Figure 4.19, the greatest uncertainty reductions occur in the lowest 1 km (Figure 4.20A and B). However, here it is possible to see improvements aloft. Between 1 and 3 km, the temperature uncertainty is reduced by approximately 0.1 °C while below 1 km it is

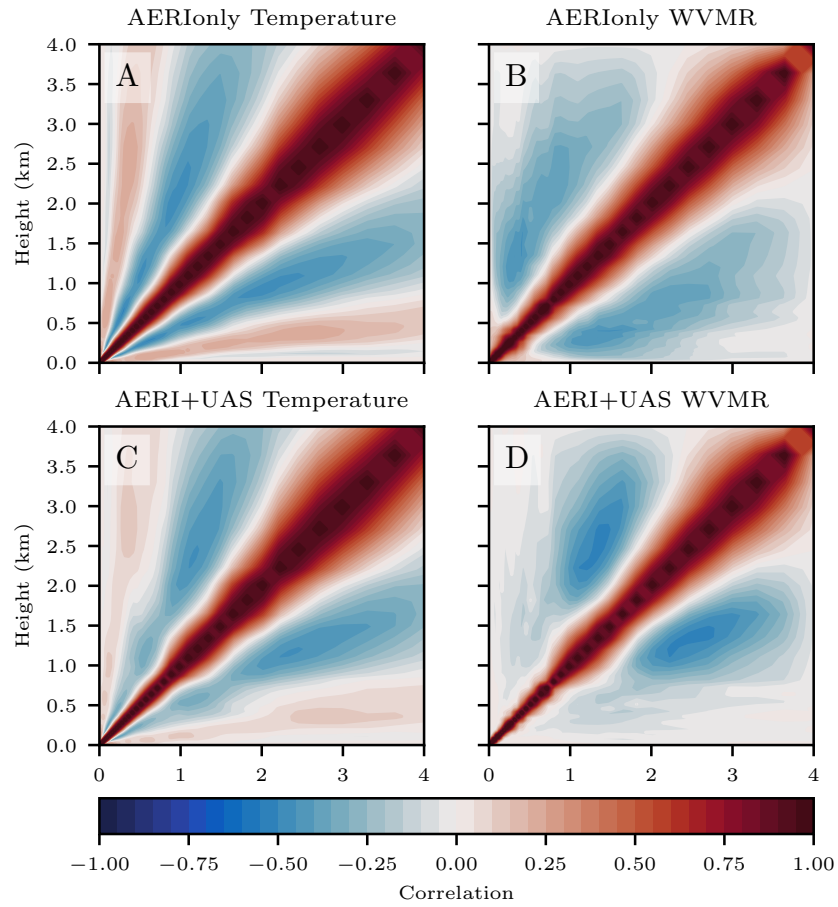


Figure 4.19: Posterior, level-to-level correlation matrices for temperature (A, C) and water vapor mixing ratio (B, D) a representative retrieval from LAPSE-RATE. The AERIonly retrievals are located on top, while the AERI+UAS are below.



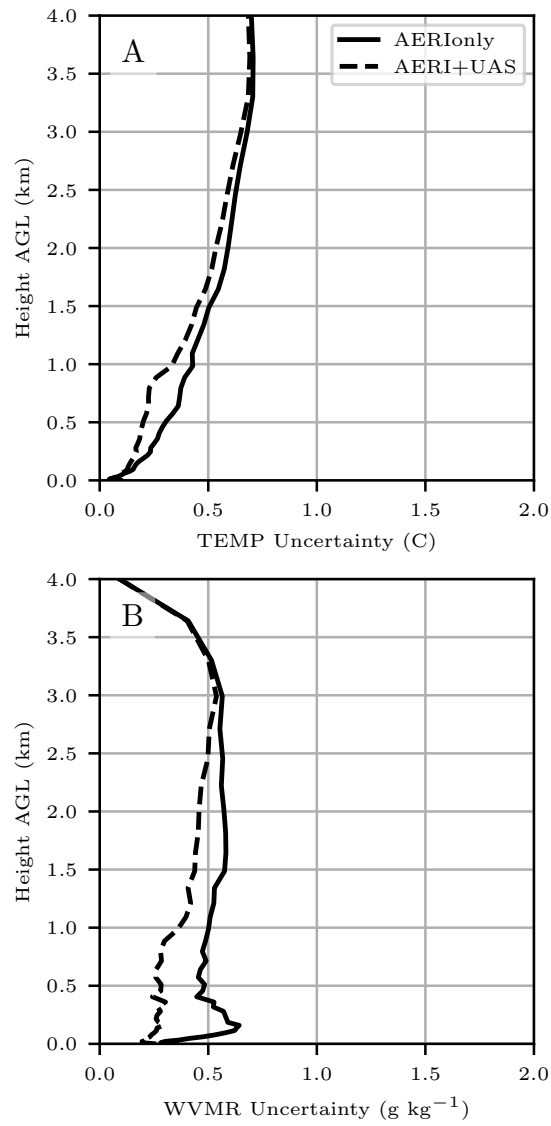


Figure 4.20: Temperature (A) and water vapor mixing ratio (B) uncertainty from a representative retrieval from LAPSE-RATE as a function of height. The AERIONly retrievals are denoted by solid lines, while the AERI+UAS lines are denoted by the dashed lines.

closer to 0.2 °C (Figure 4.20). The water vapor uncertainty is also reduced above 1 km by approximately 0.1 g kg<sup>-1</sup> (Figure 4.20).

The MWR+UAS retrievals also exhibit improvements over the MWRonly retrievals (Figure 4.21). The MWR has much less information content overall about the thermodynamic state of the atmosphere (Figure 4.21A and B). Similar to the AERI+UAS retrievals, the MWR+UAS temperature and water vapor fields are most improved in the lowest 1 km of the profile (Figure 4.21C and D). The off-diagonal correlations above the CopterSonde profiles are more noticeably improved for the MWR+UAS retrievals. The posterior correlation matrices for water vapor mixing ratio on the AERI+UAS (Figure 4.19D) and MWR+UAS (Figure 4.21D) retrieval exhibit nearly identical shapes, which indicates that these instrument measure very similar information content. This is significant because MWRs are currently much more available than AERIs and suggests that the addition of UAS to these sites could increase information even above where the WxUAS are allowed to fly.

These improvements are also seen in the uncertainty profiles from the same retrieval (Figure 4.22). The temperature uncertainty is reduced by nearly 0.5 °C below 1 km, tapering off to .25 °C at 2.5 km. The water vapor uncertainty is reduced by 0.5 g kg<sup>-1</sup> below 1 km. Uncertainty is reduced above 1 km to approximately the same levels as the AERI+UAS retrievals (Figure 4.22).

Overall, using ground-based remote sensors and WxUAS together tends to improve accuracy and minimize the limitations of each system individually. To date, most of these types of systems have been used on their own. However, combining remote sensors with WxUAS could improve accuracy and reduce uncertainty in the resulting products. Potential synergies between instruments and their possible applications are discussed in the next chapter.

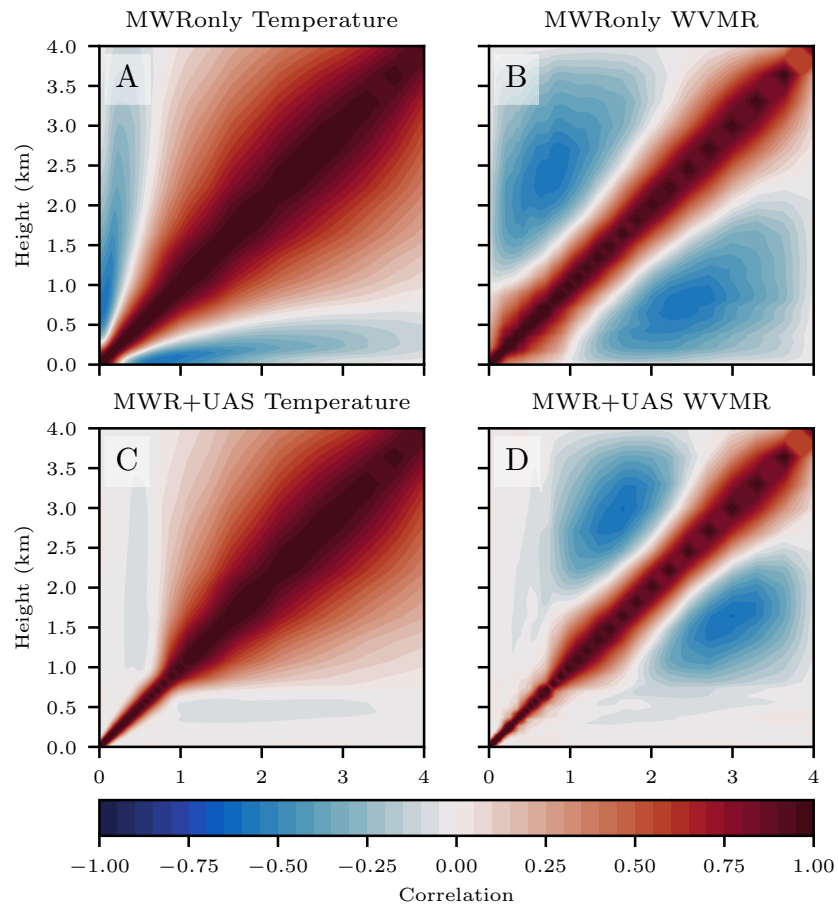


Figure 4.21: Similar to Figure 4.21, except showing showing MWRonly (top) and MWR+UAS (bottom) retrievals.

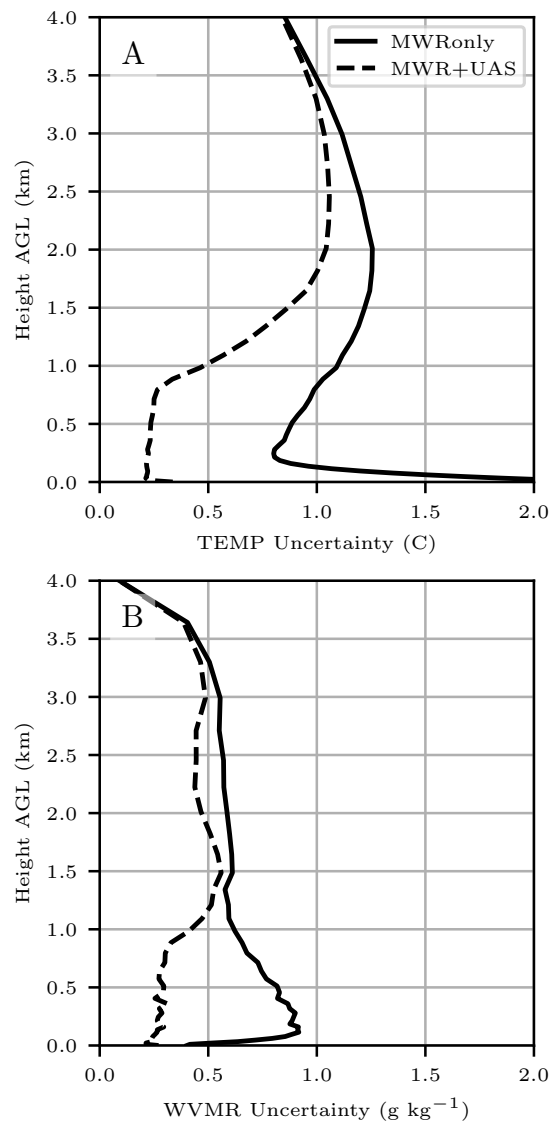


Figure 4.22: Similar to Figure 4.22, except showing showing MWRonly (solid line) and MWR+UAS (dashed line).

## Chapter 5

### Instrument Synergy

Thus far, the currently available instrumentation with potential to provide observations and assist in filling data gap that exists in the ABL have largely been treated as separate techniques. However, there could be certain advantages to combining observations from WxUAS with remote sensing data to provide a more accurate representation of processes in the ABL. Typically, there are three use cases for this type of instrumentation: data assimilation into NWP, forecaster situational awareness, and basic science. All of these have slightly different needs and could benefit from a different combination of instrumentation. In other words, even with cutting-edge boundary-layer profilers, there is no one solution to fill the boundary-layer data gap on a national scale. However, there are synergies that can be exploited for the various use cases.

For example, in the case of the CopterSonde and radiosonde comparison, outliers were found when the CopterSonde and radiosonde traversed temperature and moisture gradients at slightly different times during the morning boundary-layer transition. These outliers showcase how rapid profiling combined with remote sensing can provide high resolution observations of atmospheric processes and phenomenon. Data from a radiosonde and CopterSonde launch, along with some supplementary data from the CLAMPS DL, is shown in Figure 5.1. During this comparison, the radiosonde was launched promptly at 16:00 UTC on 17 July, 2018. Due to the very low winds, the radiosonde did not clear the flight area immediately and the CopterSonde flight had to be delayed by two minutes. When the CopterSonde launched at 16:02 UTC, the radiosonde had already traversed a small inversion at 450 m AGL. The CopterSonde also observed this inversion, though it was at 620 m AGL. The

outliers from this profile were in the layer between 450 m and 620 m where the inversion changed height. The likely cause of this rapid change in inversion height was an updraft that formed between 16:00 and 16:06 UTC (Figure 5.1b). During this time period, it was noted that a cloud formed while the CopterSonde was ascending. Referencing classical parcel theory, the updraft lifted and cooled the parcel to the lifted condensation level where latent heat release from condensation warmed the environment and modified the lapse rate. This same pattern was observed in multiple thermodynamic profiles is evidence that the combination of the CopterSonde and DL is a powerful combination for parcel scale observations.

To further illustrate the utility of combining the CopterSonde and DL observations, we can revisit the LLJ observed during the overnight period of Flux Capacitor by including the horizontal wind data from the DL overlaid with the temperature data from the CopterSonde (Figure 5.2). Using the high resolution temperature profiles from the CopterSonde near the surface, it is possible to see how mechanical mixing induced by the LLJ mixed warmer air from the residual layer to the surface. As the LLJ reached peak wind speeds at 5 UTC, a warming trend is seen in both the low-level CopterSonde data and the Oklahoma Mesonet 10-m temperature. The AERIoe retrieval from this case does pick up on the signal in the lowest levels, but due to the rapid drop in information content (and thus data resolution) with height, the data are noticeably noisy above 200-m (Figure 3.11). More frequent co-located WxUAS flights and DL profiles could help improve ABL height estimation, especially for the nocturnal stable boundary-layer.

Parcel-scale observations will be vital in basic research. Additionally, many of the research questions that need investigation require nimble approaches to observations. As an example, improving the conceptual model of CI will require precision observations in areas where CI is expected. Models cannot be completely relied upon for positioning of instrumentation (for reasons discussed in 1.1). Thus, in field campaigns

focused on CI, instrument positioning is often decided based on the available data at the time. If a platform were to be highly nimble and deployable in less than a few minutes, it would be advantageous for studying phenomena that are localized and on time scales less than 1–2 hours. Systems like CLAMPS take 15–30 minutes to deploy and the AERI and MWR inside are not sensitive enough to observe meaningful changes on these short time scales. Doppler lidars have already been successfully deployed in a nimble framework (Clements and Oliphant 2014; Laser 2020). Typically the thermodynamics from these nimble profiling systems are provided by radiosondes, but as discussed before, they are not well suited for rapid profiling. A complicating factor, especially near thunderstorms, is the balloons are quickly advected away from their launch point, making their geographically-varying data difficult to interpret. Pairing a WxUAS with a nimble Doppler lidar could provide the high fidelity observations required in complex environments.

Combining data from WxUAS with DLs may also be the most *affordable* way to measure ABL thermodynamic and kinematics. While all the studies previously described used scanning DLs, which are typically more expensive, there are cheaper profiling DLs that are built solely to profile the wind field. These tend to be relatively low-power and cheap systems and if paired with a WxUAS like the CopterSonde, could provide quality measurements for assimilation or operational forecasting and/or now-casting. One immediately impactful use case for this is assisting with fire weather forecasting, especially with respect to the nimble concept. Operational incident meteorologists and wildland firefighters would benefit from improved information about relative humidity and wind direction for determining where fire may spread.

However, one disadvantage to WxUAS is they are somewhat mechanically complex, and with current battery technology, are limited to a certain number of power cycles before the batteries need replaced. Thus, even if a reliable launch box is invented, it will be very difficult to have a network of WxUAS running at all times.

The utility of WxUAS may be relegated to on-demand, high-resolution WxUAS profiles to augment a network of remote sensors. Remote sensors have the advantage for long-term deployments since they are mechanically simple. Additionally, the direct uncertainty quantification that results from the retrieval makes it easier to include the proper uncertainty into DA systems. The ability of TROPoe to accept many different observation types could provide a framework with which to provide various combinations of observations, while keeping them in a consistent format. Dynamically changing the levels of the retrieval that are assimilated based on the information content in the retrieved profile (as in Coniglio et al. 2019) makes it simple to add and subtract observation types as needed.

Many institutions already own and operate MWRs (e.g., New York Mesonet, University of Alabama Huntsville, University of Louisiana Monroe, NOAA's Physical Science Laboratory). The simple addition of a relatively affordable WxUAS to their facility would improve the quality of observations and provide wind speed and direction measurements. Used in a retrieval framework like TROPoe, WxUAS could be used only when needed, thus minimizing wear-and-tear on the airframes and batteries. Examples where WxUAS could provide more detailed information include preceding severe weather events, air mass boundary passages, and during expected winter weather events where determining the freezing level is crucial.



2018-07-17 16:02 UTC

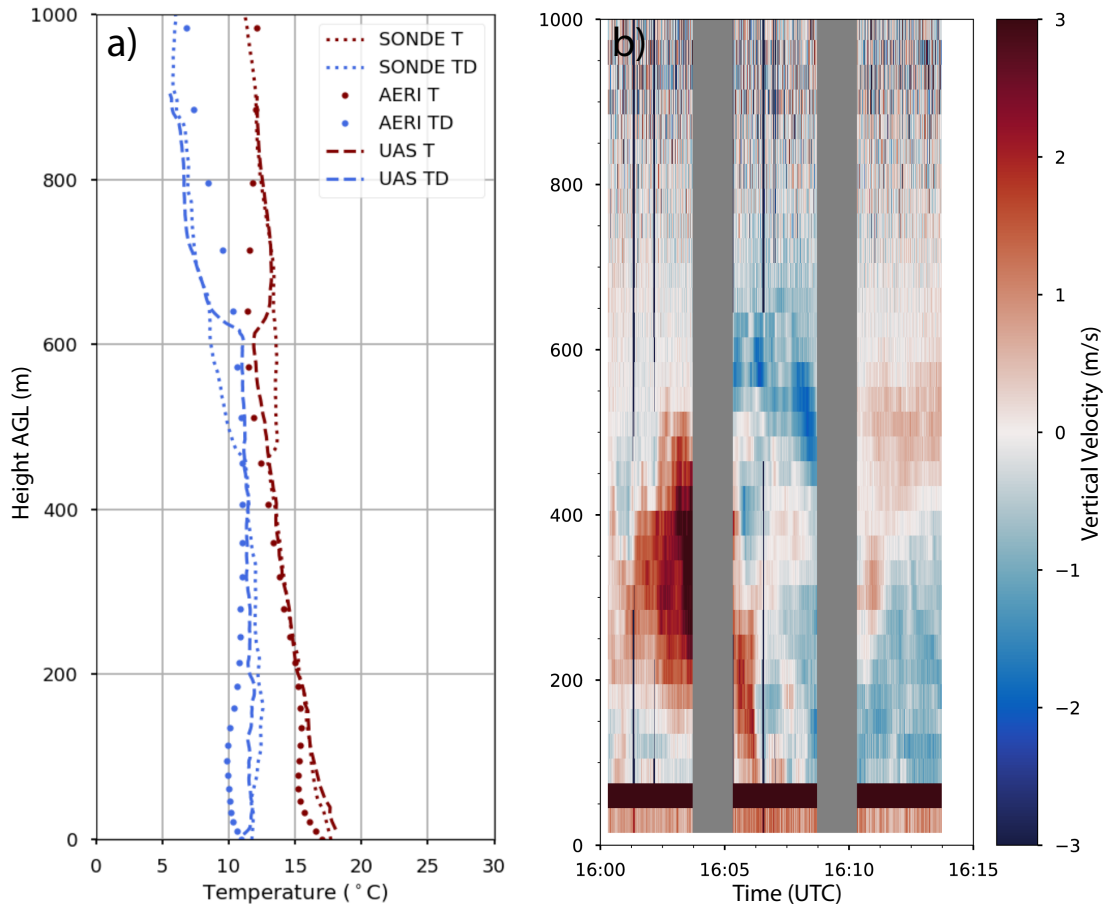


Figure 5.1: Example profile of temperature (red) and dew point temperature (blue) from each observation platform (a) and a time height cross section of vertical velocity measured from the CLAMPS DL from the same time period (b). The gray areas in (b) indicate the DL was not in vertical stare mode and was performing PPI scans.

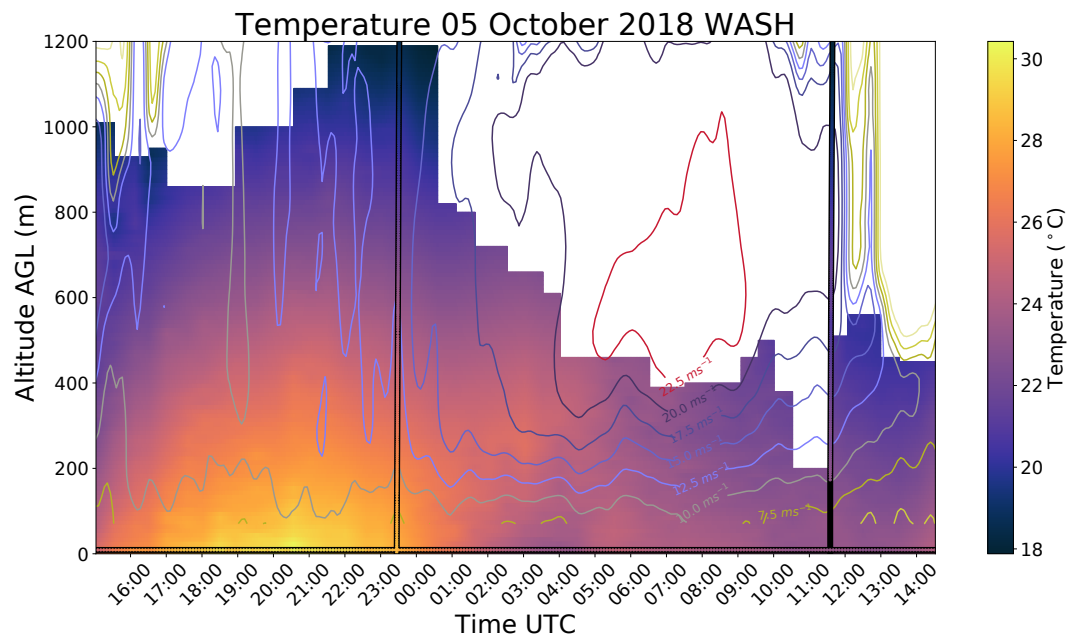


Figure 5.2: Same as Figure 1.2, only with horizontal wind speed contoured instead of the temperature.

## Chapter 6

### Conclusions

While there may never be a one-size-fits-all solution to filling the ABL data gap, there are many technologies on the horizon that can contribute to solving the problem outlined in Chapter 1. As they come online, careful consideration of their strengths and weaknesses should be taken into account while siting instrumentation. Not only should each technology be considered as an independent solution, they should also be planned in the context of other systems strengths' and weaknesses as well. As has been shown in this research, multiple systems can be combined to create more powerful observations than each system on its own. There have been relatively few studies that integrated many different types of measurements to evaluate instrument synergies. The Land–Atmosphere Feedback Experiment (LAFE, Wulfmeyer et al. 2018) is one of the most expansive experiments to examine thermodynamic and kinematic atmospheric processes through combining multiple instrument types. The Perdigão 2017 experiment (Fernando et al. 2019) included a large array of meteorological towers and scanning DLs to examine atmospheric flows in complex terrain for wind energy applications. Data from this campaign were used to advance methods for estimating quantities such as turbulent kinetic energy (e.g., Wildmann et al. 2019) in complex terrain. The goal of the studies herein were to evaluate the platforms on their own as well as in a synergistic configuration. Here are some of the main conclusions from these studies:

- Currently available technologies are capable of fulfilling the goals set out by National Research Council (2009) and Hoff et al. (2012). However, with continued testing and evaluation, these technologies could still be improved upon.

- Wind speed estimates from rotary-wing, profiling WxUAS benefit from being calibrated and validated using ground-based wind profilers such as DLs. Additionally, simple relationships between the tilt of the air frame and the wind speed likely do not work well at higher wind speeds. More complex relationships should continue to be explored.
- Physics-based thermodynamic retrievals such as AERIOe and TROPoe still require a representative estimate of the average state of the atmosphere for a given location to use as an a priori dataset. Combining these retrievals with other datasets, such as those from WxUAS, can help overcome this limitation.
- Some combinations of instruments are complementary in the information they provide. For example, WxUAS and DLs together provide very detailed observations of small scale processes that occur in the boundary layer.

## 6.1 Limitations

One important note to contextualize the analyses in Section 4.2: while the mean differences in the observations derived from independent systems are often fairly small, individual profiles still can vary wildly (see Figure 4.14). Thus there are two ways to interpret these results: the “retrieval science” standpoint and the “meteorological” standpoint. For instance, when analyzing the maximum allowed height of a superadiabatic layer, from a retrieval science standpoint this parameter has minimal impact. Mean differences of temperature are less than 1 °C and with standard deviations of the differences on the same order as the mean difference. It could be argued that these discrepancies fall within the range of uncertainty outlined by Hoff et al. (2012). However, from a meteorological standpoint, individual profiles can sometimes exhibit drastic differences. Without careful scrutiny, these profiles could be misinterpreted. Thus, there is still plenty of work to be done in how to assimilate these new types of

data and how to incorporate them into forecaster workflows. For example, forecasters often rely on mean lapse rates to determine areas where enhanced mixing may result in convection initiation. If forecasters were to use the data from Section 4.2 for this purpose, there could have been erroneous conclusions.

The fact that there are limited quality validation datasets for these type of retrievals outside of the SGP and the various ARMs sites makes it extremely difficult to determine which parameters need finely tuned to the location. Even more so, changing small, seemingly insignificant parameters can have a significant impact on an individual retrieval. As these new profiling instruments continue to be used in novel ways, it is important to continue to collect validation datasets along side them, specifically to enable scientists to push the envelope for retrieval science. Along these lines, at least while boundary-layer profiling systems continue to remain relatively novel, creating super sites where many types of boundary-layer profilers are present will help continue to improve retrieval science (e.g., facilities like those operated by ARM).

Most of the data collected from this study occurred in the mid-latitudes under relatively normal conditions. The community needs to continue to collect quality observational datasets in all weather and climate extremes to evaluate the optimal instrumentation for that regime.

## **6.2 Looking Forward**

An additional area where thermodynamic observations could still be improved is inside of clouds. Passive sensing methods using retrievals like TROPoe cannot currently retrieve accurate temperature and humidity profiles above cloud base. Similarly, boundary-layer profiling from space-born satellites is largely affected by clouds. Typically in data assimilation, most cloudy areas observed from satellite are disregarded. Active thermodynamic profilers (e.g., WVDIAL, Raman lidar) also cannot

typically see into clouds because, at the wavelength of electromagnetic radiation used, the signal is quickly extinguished by water droplets. Due to current regulatory issues, WxUAS are not permitted to fly inside of clouds unless special permission is granted. Even with special permission, careful consideration must be taken to ensure sensors remain dry while being well aspirated. Thus, even most observations from radiosondes should not be trusted in clouds due to water loading on the sensors. Above the freezing level, water accumulated on the sensors can solidify and cause erroneous measurements. This is also an issue on WxUAS since traditional, crewed-aircraft deicing measures do not translate well to small systems like the CopterSonde. Thus, more development is required to reliably fly in icing conditions.

Going forward, developing scalable observational architecture that can adapt to the network-of-networks concept will be crucial to its success. Consistent guidelines for data management/preparation, uncertainty reporting, and calibration procedures still need to be discussed and adopted. Remote sensing systems can likely lean on prior data standards used in climate research facilities developed by ARM. However, WxUAS are in the “wild west” stage of development, with many different solutions and data formats being proposed. As systems mature and are more widely used, these standards will be increasingly important to ensure wide adoption of the observations, especially for any multi-instrument profiling sites.

As mentioned previously, one of the major advantages of a framework like TROPoe is the ability to include many different types of observations in the observation vector while still getting a consistent output and estimate of the uncertainty within the profile. More studies using TROPoe with varying instrumentation combinations are necessary to determine if this is the proper way to move forward with creating a nationwide network. At the moment, there does not exist an equivalent retrieval for kinematic measurements. Developing a similar retrieval for kinematic measurements

would further the concept of being able to tailor observation platforms to the observation site while still providing consistent output. Work is already under way to lay the ground work for such a retrieval.

One aspect that has not been extensively explored or discussed in these studies is the representativeness of the individual profiles. The WxUAS in particular are capable of measuring hyper-local thermodynamic features that may not be representative of the larger area surrounding the profiling site. With respect to the remote sensors, there are possible configurations that may result in more representative measurements over a larger area. For example, the HATPRO performs off-zenith scans to gather more information on the boundary layer. In fact, these elevation scans in a retrieval like TROPoe create similar information content to the AERI (Blumberg et al. 2015b). This can also give some information about how heterogeneous the boundary layer structure may be by comparing the brightness temperatures from both sides of the scan. Additionally, the HATPRO could be equipped with an azimuthal scanner to provide information about temperature and moisture heterogeneity in all directions. All of the thermodynamic profiling information in the studies here only used zenith information. However, there is still debate as to which approach is better (Hoff et al. 2012).

In conclusion, ABL measurements can provide important observations for addressing a multitude of research questions related to the Earth system. The field is at a point where many different types of research platforms are available and likely will revolutionize boundary-layer studies. The systems analyzed in these studies all show promise when validated via the historically standard radiosonde measurements. With careful consideration of the strengths of currently available platforms, and by being creative in how and where systems are deployed, a highly adaptable observation network could be built to satisfy requirements for a number of spatio-temporal scales and

significantly improve understanding of the part of the atmosphere in which directly impacts many high-impact weather phenomena.



## Bibliography

- Angevine, W. M., J. Brioude, S. McKeen, and J. S. Holloway, 2014: Uncertainty in Lagrangian pollutant transport simulations due to meteorological uncertainty from a mesoscale WRF ensemble. *Geoscientific Model Development*, **7** (6), 2817–2829, doi:10.5194/gmd-7-2817-2014.
- Angevine, W. M., J. M. Edwards, M. Lothon, M. A. LeMone, and S. R. Osborne, 2020: Transition Periods in the Diurnally-Varying Atmospheric Boundary Layer Over Land. *Boundary-Layer Meteorology*, doi:10.1007/s10546-020-00515-y.
- Arya, P. S., 2001: *Introduction to Micrometeorology*, Vol. 79. Academic Press.
- Ash, K. D., M. J. Egnoto, S. M. Strader, W. S. Ashley, D. B. Roueche, K. E. Klockow-McClain, D. Caplen, and M. Dickerson, 2020: Structural Forces: Perception and Vulnerability Factors for Tornado Sheltering within Mobile and Manufactured Housing in Alabama and Mississippi. *Weather, Climate, and Society*, **12** (3), 453–472, doi:10.1175/WCAS-D-19-0088.1.
- Ashley, W. S., 2007: Spatial and Temporal Analysis of Tornado Fatalities in the United States: 1880–2005. *Weather and Forecasting*, **22** (6), 1214–1228, doi:10.1175/2007WAF2007004.1.
- Banta, R. M., Y. L. Pichugina, N. D. Kelley, R. M. Hardesty, and W. A. Brewer, 2013: Wind energy meteorology: Insight into wind properties in the turbine-rotor layer of the atmosphere from high-resolution doppler lidar. *Bulletin of the American Meteorological Society*, **94** (6), 883–902, doi:10.1175/BAMS-D-11-00057.1.
- Banta, R. M., and Coauthors, 2015: 3D volumetric analysis of wind turbine wake properties in the atmosphere using high-resolution doppler lidar. *Journal of Atmospheric and Oceanic Technology*, **32** (5), 904–914, doi:10.1175/JTECH-D-14-00078.1.
- Barbieri, L., and Coauthors, 2019: Intercomparison of Small Unmanned Aircraft System (sUAS) Measurements for Atmospheric Science during the LAPSE-RATE Campaign. *Sensors*, **19** (9), 2179, doi:10.3390/s19092179.
- Barthelmie, R., S. Pryor, N. Wildmann, and R. Menke, 2018: Wind turbine wake characterization in complex terrain via integrated Doppler lidar data from the Perdigão experiment. *Journal of Physics: Conference Series*, **1037**, 052022, doi:10.1088/1742-6596/1037/5/052022.
- Behrendt, A., V. Wulfmeyer, C. Senff, S. K. Muppa, F. Späth, D. Lange, N. Kalthoff, and A. Wieser, 2020: Observation of sensible and latent heat flux profiles with lidar. *Atmospheric Measurement Techniques*, **13** (6), 3221–3233, doi:10.5194/amt-13-3221-2020.

- Bell, T., P. Klein, N. Wildmann, and R. Menke, 2018, submitted: Analysis of flow in complex terrain using multi-doppler lidar retrievals. *Atmospheric Measurement Techniques*.
- Bell, T. M., B. R. Greene, P. M. Klein, M. Carney, and P. B. Chilson, 2020: Confronting the boundary layer data gap: Evaluating new and existing methodologies of probing the lower atmosphere. *Atmospheric Measurement Techniques*, **13** (7), 3855–3872, doi:10.5194/amt-13-3855-2020.
- Bell, T. M., P. M. Klein, J. K. Lundquist, and S. Waugh, 2021: Remote-sensing and radiosonde datasets collected in the San Luis Valley during the LAPSE-RATE campaign. *Earth System Science Data*, **13** (3), 1041–1051, doi:10.5194/essd-13-1041-2021.
- Blumberg, W. G., D. D. Turner, U. Löhnert, and S. Castleberry, 2015a: Ground-based temperature and humidity profiling using spectral infrared and microwave observations. Part II: Actual retrieval performance in clear-sky and cloudy conditions. *Journal of Applied Meteorology and Climatology*, **54** (11), 2305–2319, doi:10.1175/JAMC-D-15-0005.1.
- Blumberg, W. G., D. D. Turner, U. Löhnert, and S. Castleberry, 2015b: Ground-Based Temperature and Humidity Profiling Using Spectral Infrared and Microwave Observations. Part II: Actual Retrieval Performance in Clear-Sky and Cloudy Conditions. *Journal of Applied Meteorology and Climatology*, **54** (11), 2305–2319, doi:10.1175/JAMC-D-15-0005.1.
- Bodini, N., J. K. Lundquist, and R. K. Newsom, 2018: Estimation of turbulence dissipation rate and its variability from sonic anemometer and wind Doppler lidar during the XPIA field campaign. *Atmospheric Measurement Techniques*, **11** (7), 4291–4308, doi:10.5194/amt-11-4291-2018.
- Bonin, T., P. Chilson, B. Zielke, and E. Fedorovich, 2013: Observations of the Early Evening Boundary-Layer Transition Using a Small Unmanned Aerial System. *Boundary-Layer Meteorology*, **146** (1), 119–132, doi:10.1007/s10546-012-9760-3.
- Bonin, T. A., and Coauthors, 2017: Evaluation of turbulence measurement techniques from a single Doppler lidar. *Atmospheric Measurement Techniques*, **10** (8), 3021–3039, doi:10.5194/amt-10-3021-2017.
- Brock, F. V., K. C. Crawford, R. L. Elliott, G. W. Cuperus, S. J. Stadler, H. L. Johnson, and M. D. Eilts, 1995: The Oklahoma Mesonet: A Technical Overview. *Journal of Atmospheric and Oceanic Technology*, **12** (1), 5–19, doi:10.1175/1520-0426(1995)012<0005:TOMATO>2.0.CO;2.
- Brotzge, J. A., and Coauthors, 2020: A Technical Overview of the New York State Mesonet Standard Network. *Journal of Atmospheric and Oceanic Technology*, **37** (10), 1827–1845, doi:10.1175/JTECH-D-19-0220.1.

- Browning, K. A., and R. Wexler, 1968: The determination of kinematic properties of a wind field using doppler radar. *Journal of Applied Meteorology*, **7** (1), 105–113, doi:10.1175/1520-0450(1968)007<0105:TDOKPO>2.0.CO;2.
- Businger, J. A., J. C. Wyngaard, Y. Izumi, and E. F. Bradley, 1971: Flux-Profile Relationships in the Atmospheric Surface Layer. *Journal of the Atmospheric Sciences*, **28** (2), 181–189, doi:10.1175/1520-0469(1971)028<0181:FPRITA>2.0.CO;2.
- Calhoun, R., R. Heap, M. Princevac, R. Newsom, H. Fernando, and D. Ligon, 2006: Virtual towers using coherent doppler lidar during the joint urban 2003 dispersion experiment. *Journal of Applied Meteorology and Climatology*, **45** (8), 1116–1126, doi:10.1175/JAM2391.1.
- Chilson, P., A. Gleason, B. Zielke, F. Nai, M. Yeary, P. Klein, and W. Shalamunec, 2009: SMARTSonde: A small UAS platform to support radar research.
- Chilson, P. B., and Coauthors, 2019: Moving towards a network of autonomous UAS atmospheric profiling stations for observations in the earth’s lower atmosphere: The 3D mesonet concept. *Sensors*, **19** (12), doi:10.3390/s19122720.
- Chipilski, H. G., X. Wang, and D. B. Parsons, 2020: Impact of Assimilating PECAN Profilers on the Prediction of Bore-Driven Nocturnal Convection: A Multiscale Forecast Evaluation for the 6 July 2015 Case Study. *Monthly Weather Review*, **148** (3), 1147–1175, doi:10.1175/MWR-D-19-0171.1.
- Choukulkar, A., and Coauthors, 2017: Evaluation of single and multiple Doppler lidar techniques to measure complex flow during the XPIA field campaign. *Atmospheric Measurement Techniques*, **10** (1), 247–264, doi:10.5194/amt-10-247-2017.
- Chow, F. K., C. Schär, N. Ban, K. A. Lundquist, L. Schlemmer, and X. Shi, 2019: Crossing Multiple Gray Zones in the Transition from Mesoscale to Microscale Simulation over Complex Terrain. *Atmosphere*, **10** (5), 274, doi:10.3390/atmos10050274.
- Clements, C. B., and A. J. Oliphant, 2014: The California State University Mobile Atmospheric Profiling System: A Facility for Research and Education in Boundary Layer Meteorology. *Bulletin of the American Meteorological Society*, **95** (11), 1713–1724, doi:10.1175/BAMS-D-13-00179.1.
- Coniglio, M. C., J. Correia, P. T. Marsh, and F. Kong, 2013: Verification of Convection-Allowing WRF Model Forecasts of the Planetary Boundary Layer Using Sounding Observations. *Weather and Forecasting*, **28** (3), 842–862, doi:10.1175/WAF-D-12-00103.1.
- Coniglio, M. C., G. S. Romine, D. D. Turner, and R. D. Torn, 2019: Impacts of Targeted AERI and Doppler Lidar Wind Retrievals on Short-Term Forecasts of the Initiation and Early Evolution of Thunderstorms. *Monthly Weather Review*, **147** (4), 1149–1170, doi:10.1175/MWR-D-18-0351.1.

- Crook, N. A., 1996: Sensitivity of Moist Convection Forced by Boundary Layer Processes to Low-Level Thermodynamic Fields. *Monthly Weather Review*, **124** (8), 1767–1785, doi:10.1175/1520-0493(1996)124<1767:SOMCFB>2.0.CO;2.
- de Boer, G., S. Waugh, A. Erwin, S. Borenstein, C. Dixon, W. Shanti, A. Houston, and B. Argrow, 2021: Measurements from mobile surface vehicles during the Lower Atmospheric Profiling Studies at Elevation – a Remotely-piloted Aircraft Team Experiment (LAPSE-RATE). *Earth System Science Data*, **13** (1), 155–169, doi:10.5194/essd-13-155-2021.
- de Boer, G., and Coauthors, 2020a: Data generated during the 2018 LAPSE-RATE campaign: An introduction and overview. *Earth System Science Data*, **12** (4), 3357–3366, doi:10.5194/essd-12-3357-2020.
- de Boer, G., and Coauthors, 2020b: Development of Community, Capabilities, and Understanding through Unmanned Aircraft-Based Atmospheric Research: The LAPSE-RATE Campaign. *Bulletin of the American Meteorological Society*, **101** (5), E684–E699, doi:10.1175/BAMS-D-19-0050.1.
- Degelia, S. K., X. Wang, and D. J. Stensrud, 2019: An Evaluation of the Impact of Assimilating AERI Retrievals, Kinematic Profilers, Rawinsondes, and Surface Observations on a Forecast of a Nocturnal Convection Initiation Event during the PECAN Field Campaign. *Monthly Weather Review*, **147** (8), 2739–2764, doi:10.1175/MWR-D-18-0423.1.
- Durre, I., R. S. Vose, and D. B. Wuertz, 2006: Overview of the Integrated Global Radiosonde Archive. *Journal of Climate*, **19** (1), 53–68, doi:10.1175/JCLI3594.1.
- Fabry, F., 2006: The Spatial Variability of Moisture in the Boundary Layer and Its Effect on Convection Initiation: Project-Long Characterization. *Monthly Weather Review*, **134** (1), 79–91, doi:10.1175/MWR3055.1.
- Fernando, H. J. S., and Coauthors, 2019: The perdigão: Peering into microscale details of mountain winds. *Bulletin of the American Meteorological Society*, **100** (5), 799–819, doi:10.1175/BAMS-D-17-0227.1, <https://doi.org/10.1175/BAMS-D-17-0227.1>.
- Fiebrich, C. A., J. R. Ziolkowska, P. B. Chilson, and E. A. Pillar-Little, 2021: Potential Socioeconomic and Environmental Benefits and Beneficiaries of UAS Atmospheric Profiles from a 3D Mesonet. *Weather, Climate, and Society*, **13** (2), 377–391, doi:10.1175/WCAS-D-20-0118.1.
- Frew, E. W., B. Argrow, S. Borenstein, S. Swenson, C. A. Hirst, H. Havenga, and A. Houston, 2020: Field observation of tornadic supercells by multiple autonomous fixed-wing unmanned aircraft. *Journal of Field Robotics*, **37** (6), 1077–1093, doi:10.1002/rob.21947.

- Gal-Chen, T., M. Xu, and W. L. Eberhard, 1992: Estimations of atmospheric boundary layer fluxes and other turbulence parameters from Doppler lidar data. *Journal of Geophysical Research: Atmospheres*, **97 (D17)**, 18 409–18 423, doi:10.1029/91JD03174, <https://agupubs.onlinelibrary.wiley.com/doi/pdf/10.1029/91JD03174>.
- Gebauer, J. G., A. Shapiro, E. Fedorovich, and P. Klein, 2018: Convection Initiation Caused by Heterogeneous Low-Level Jets over the Great Plains. *Monthly Weather Review*, **146 (8)**, 2615–2637, doi:10.1175/MWR-D-18-0002.1.
- Geerts, B., and Coauthors, 2017: The 2015 Plains Elevated Convection at Night Field Project. *Bulletin of the American Meteorological Society*, **98 (4)**, 767–786, doi:10.1175/BAMS-D-15-00257.1.
- Gioli, B., F. Miglietta, F. P. Vaccari, A. Zaldei, and B. D. Martino, 2006: The Sky Arrow ERA, an innovative airborne platform to monitor mass, momentum and energy exchange of ecosystems. *Annals of Geophysics*, **49 (1)**, doi:10.4401/ag-3159.
- González-Rocha, J., C. A. Woolsey, C. Sultan, and S. F. J. De Wekker, 2019: Sensing wind from quadrotor motion. *Journal of Guidance, Control, and Dynamics*, **42 (4)**, 836–852, doi:10.2514/1.G003542, <https://doi.org/10.2514/1.G003542>.
- Greene, B., A. Segales, T. Bell, E. Pillar-Little, and P. Chilson, 2019: Environmental and sensor integration influences on temperature measurements by rotary-wing unmanned aircraft systems. *Sensors*, **19 (6)**, 1470, doi:10.3390/s19061470.
- Greene, B. R., 2018: Boundary layer profiling using rotary-wing unmanned aircraft systems: Filling the atmospheric data gap. Ph.D. thesis, University of Oklahoma.
- Greene, B. R., A. R. Segales, S. Waugh, S. Duthoit, and P. B. Chilson, 2018: Considerations for temperature sensor placement on rotary-wing unmanned aircraft systems. *Atmospheric Measurement Techniques*, **11 (10)**, 5519–5530, doi:10.5194/amt-11-5519-2018.
- Hane, C. E., H. B. Bluestein, T. M. Crawford, M. E. Baldwin, and R. M. Rabin, 1997: Severe Thunderstorm Development in Relation to Along-Dryline Variability: A Case Study. *Monthly Weather Review*, **125 (2)**, 231–251, doi:10.1175/1520-0493(1997)125<0231:STDIRT>2.0.CO;2.
- Hane, C. E., C. L. Ziegler, and H. B. Bluestein, 1993: Investigation of the Dryline and Convective Storms Initiated along the Dryline: Field Experiments during COPS-91. *Bulletin of the American Meteorological Society*, **74 (11)**, 2133–2145, doi:10.1175/1520-0477(1993)074<2133:IOTDAC>2.0.CO;2.
- Helbig, M., and Coauthors, 2021: Integrating continuous atmospheric boundary layer and tower-based flux measurements to advance understanding of land-atmosphere interactions. *Agricultural and Forest Meteorology*, **307**, 108 509, doi:10.1016/j.agrformet.2021.108509.

- Hill, M., R. Calhoun, H. J. S. Fernando, A. Wieser, A. Dörnbrack, M. Weissmann, G. Mayr, and R. Newsom, 2010: Coplanar doppler lidar retrieval of rotors from t-rex. *Journal of the Atmospheric Sciences*, **67** (3), 713–729, doi:10.1175/2009JAS3016.1.
- Hoff, R. M., and R. M. Hardesty, 2012: Thermodynamic profiling technologies workshop report to the national science foundation and the national weather service. Tech. rep., National Center for Atmospheric Research / National Center for Atmospheric Research. doi:10.5065/D6SQ8XCF.
- Honnert, R., and Coauthors, 2020: The Atmospheric Boundary Layer and the “Gray Zone” of Turbulence: A Critical Review. *Journal of Geophysical Research: Atmospheres*, **125** (13), e2019JD030317, doi:10.1029/2019JD030317.
- Houston, A. L., B. Argrow, J. Elston, J. Lahowetz, E. W. Frew, and P. C. Kennedy, 2012: The collaborative Colorado–Nebraska unmanned aircraft system experiment. *Bulletin of the American Meteorological Society*, **93** (1), 39–54, doi:10.1175/2011BAMS3073.1, <https://doi.org/10.1175/2011BAMS3073.1>.
- Hu, J., N. Yussouf, D. D. Turner, T. A. Jones, and X. Wang, 2019: Impact of Ground-Based Remote Sensing Boundary Layer Observations on Short-Term Probabilistic Forecasts of a Tornadoic Supercell Event. *Weather and Forecasting*, **34** (5), 1453–1476, doi:10.1175/WAF-D-18-0200.1.
- Hu, X.-M., J. W. Nielsen-Gammon, and F. Zhang, 2010: Evaluation of Three Planetary Boundary Layer Schemes in the WRF Model. *Journal of Applied Meteorology and Climatology*, **49** (9), 1831–1844, doi:10.1175/2010JAMC2432.1.
- Hubbard, K. G., X. Lin, C. B. Baker, and B. Sun, 2004: Air Temperature Comparison between the MMTS and the USCRN Temperature Systems. *Journal of Atmospheric and Oceanic Technology*, **21** (10), 1590–1597, doi:10.1175/1520-0426(2004)021<1590:ATCBTM>2.0.CO;2.
- Janjić, Z. I., 1994: The Step-Mountain Eta Coordinate Model: Further Developments of the Convection, Viscous Sublayer, and Turbulence Closure Schemes. *Monthly Weather Review*, **122** (5), 927–945, doi:10.1175/1520-0493(1994)122<0927:TSMECM>2.0.CO;2.
- Klein, P., and Coauthors, 2015: LABEL: A multi-institutional, student-led, atmospheric boundary layer experiment. *Bulletin of the American Meteorological Society*, **96** (10), 1743–1764, doi:10.1175/BAMS-D-13-00267.1.
- Knuteson, R. O., and Coauthors, 2004a: Atmospheric emitted radiance interferometer. Part I: Instrument design. *Journal of Atmospheric and Oceanic Technology*, **21** (12), 1763–1776, doi:10.1175/JTECH-1662.1.

- Knuteson, R. O., and Coauthors, 2004b: Atmospheric emitted radiance interferometer. Part II: Instrument performance. *Journal of Atmospheric and Oceanic Technology*, **21** (12), 1777–1789, doi:10.1175/JTECH-1663.1.
- Koch, S. E., M. Fengler, P. B. Chilson, K. L. Elmore, B. Argrow, D. L. Andra, and T. Lindley, 2018: On the use of unmanned aircraft for sampling mesoscale phenomena in the preconvective boundary layer. *Journal of Atmospheric and Oceanic Technology*, **35** (11), 2265–2288, doi:10.1175/JTECH-D-18-0101.1, <https://doi.org/10.1175/JTECH-D-18-0101.1>.
- Kral, S. T., and Coauthors, 2018: Innovative Strategies for Observations in the Arctic Atmospheric Boundary Layer (ISOBAR)—The Hailuoto 2017 Campaign. *Atmosphere*, **9** (7), 268, doi:10.3390/atmos9070268.
- Lange, D., A. Behrendt, and V. Wulfmeyer, 2019: Compact Operational Tropospheric Water Vapor and Temperature Raman Lidar with Turbulence Resolution. *Geophysical Research Letters*, **46** (24), 14 844–14 853, doi:10.1029/2019GL085774.
- Laser, J., 2020: Evaluation of the Warn-on-Forecast System with Doppler Lidar and Mobile Radiosondes from TORUS2019. URL <https://shareok.org/handle/11244/325438>.
- Lawrence, D. A., and B. B. Balsley, 2013: High-resolution atmospheric sensing of multiple atmospheric variables using the DataHawk small airborne measurement system. *Journal of Atmospheric and Oceanic Technology*, **30** (10), 2352–2366, doi:10.1175/JTECH-D-12-00089.1, <https://doi.org/10.1175/JTECH-D-12-00089.1>.
- Liljegren, J. C., E. E. Clothiaux, G. G. Mace, S. Kato, and X. Dong, 2001: A new retrieval for cloud liquid water path using a ground-based microwave radiometer and measurements of cloud temperature. *Journal of Geophysical Research: Atmospheres*, **106** (D13), 14 485–14 500, doi:10.1029/2000JD900817.
- Lim, J. R., B. F. Liu, and M. Egnoto, 2019: Cry Wolf Effect? Evaluating the Impact of False Alarms on Public Responses to Tornado Alerts in the Southeastern United States. *Weather, Climate, and Society*, **11** (3), 549–563, doi:10.1175/WCAS-D-18-0080.1.
- Liu, Y., and Coauthors, 2019: Fire behaviour and smoke modelling: Model improvement and measurement needs for next-generation smoke research and forecasting systems. *International Journal of Wildland Fire*, **28** (8), 570–588, doi:10.1071/WF18204.
- Löhnert, U., and O. Maier, 2012: Operational profiling of temperature using ground-based microwave radiometry at Payerne: Prospects and challenges. *Atmospheric Measurement Techniques*, **5** (5), 1121–1134, doi:10.5194/amt-5-1121-2012.

- Mann, J., and Coauthors, 2017: Complex terrain experiments in the new european wind atlas. *Philosophical Transactions of the Royal Society A: Mathematical, Physical and Engineering Sciences*, **375** (2091), 20160 101, doi:10.1098/rsta.2016.0101, <https://royalsocietypublishing.org/doi/pdf/10.1098/rsta.2016.0101>.
- Maschwitz, G., U. Löhnert, S. Crewell, T. Rose, and D. D. Turner, 2013: Investigation of ground-based microwave radiometer calibration techniques at 530 hPa. *Atmospheric Measurement Techniques*, **6** (10), 2641–2658, doi:10.5194/amt-6-2641-2013.
- McPherson, R. A., and Coauthors, 2007: Statewide Monitoring of the Mesoscale Environment: A Technical Update on the Oklahoma Mesonet. *Journal of Atmospheric and Oceanic Technology*, **24** (3), 301–321, doi:10.1175/JTECH1976.1.
- Monin, A., and A. Obukhov, 1959: Basic laws of turbulent mixing in the ground layer of the atmosphere.
- Nakanishi, M., and H. Niino, 2004: An Improved Mellor–Yamada Level-3 Model with Condensation Physics: Its Design and Verification. *Boundary-Layer Meteorology*, **112** (1), 1–31, doi:10.1023/B:BOUN.0000020164.04146.98.
- National Research Council, 2009: *Observing Weather and Climate from the Ground up: A Nationwide Network of Networks*. The National Academies Press, Washington, DC, doi:10.17226/12540.
- Neumann, P. P., and M. Bartholmai, 2015a: Real-time wind estimation on a micro unmanned aerial vehicle using its inertial measurement unit. *Sensors and Actuators A: Physical*, doi:10.1016/j.sna.2015.09.036.
- Neumann, P. P., and M. Bartholmai, 2015b: Real-time wind estimation on a micro unmanned aerial vehicle using its inertial measurement unit. *Sensors and Actuators A: Physical*, **235**, 300–310, doi:10.1016/j.sna.2015.09.036.
- Newman, J. F., T. A. Bonin, P. M. Klein, S. Wharton, and R. K. Newsom, 2016: Testing and validation of multi-lidar scanning strategies for wind energy applications. *Wind Energy*, **19** (12), 2239–2254, doi:10.1002/we.1978, <https://onlinelibrary.wiley.com/doi/pdf/10.1002/we.1978>.
- Olson, J. B., and Coauthors, 2019: Improving Wind Energy Forecasting through Numerical Weather Prediction Model Development. *Bulletin of the American Meteorological Society*, **100** (11), 2201–2220, doi:10.1175/BAMS-D-18-0040.1.
- Palomaki, R. T., N. T. Rose, M. van den Bossche, T. J. Sherman, and S. F. J. De Wekker, 2017: Wind estimation in the lower atmosphere using multirotor aircraft. *Journal of Atmospheric and Oceanic Technology*, **34** (5), 1183–1191, doi:10.1175/JTECH-D-16-0177.1, <https://doi.org/10.1175/JTECH-D-16-0177.1>.



- Parsons, D. B., M. A. Shapiro, R. M. Hardesty, R. J. Zamora, and J. M. Intrieri, 1991: The Finescale Structure of a West Texas Dryline. *Monthly Weather Review*, **119** (5), 1242–1258, doi:10.1175/1520-0493(1991)119<1242:TFSOAW>2.0.CO;2.
- Päschke, E., R. Leinweber, and V. Lehmann, 2015: An assessment of the performance of a 1.5  $\mu\text{m}$  Doppler lidar for operational vertical wind profiling based on a 1-year trial. *Atmospheric Measurement Techniques*, **8** (6), 2251–2266, doi:10.5194/amt-8-2251-2015.
- Pearson, G., F. Davies, and C. Collier, 2009: An analysis of the performance of the UFAM pulsed doppler lidar for observing the boundary layer. *Journal of Atmospheric and Oceanic Technology*, **26** (2), 240–250, doi:10.1175/2008JTECHA1128.1, <https://doi.org/10.1175/2008JTECHA1128.1>.
- Petäjä, T., and Coauthors, 2016: Enhanced air pollution via aerosol-boundary layer feedback in China. *Scientific Reports*, **6**, 18 998, doi:10.1038/srep18998.
- Reuder, J., P. Brisset, M. Jonassen, M. Müller, and S. Mayer, 2009: The small unmanned meteorological observer SUMO: A new tool for atmospheric boundary layer research. *Meteorologische Zeitschrift*, **18** (2), 141–147.
- Reuder, J., M. O. Jonassen, and H. Ólafsson, 2012: The Small Unmanned Meteorological Observer SUMO: Recent developments and applications of a micro-UAS for atmospheric boundary layer research. *Acta Geophysica*, **60** (5), 1454–1473, doi:10.2478/s11600-012-0042-8.
- Rhea, J. O., 1966: A study of thunderstorm formation along dry lines. *Journal of Applied Meteorology (1962-1982)*, **5** (1), 58–63, URL <http://www.jstor.org/stable/26172401>.
- Rochette, L., W. L. Smith, M. Howard, and T. Bratcher, 2009: ASSIST, Atmospheric Sounder Spectrometer for Infrared Spectral Technology: Latest development and improvement in the atmospheric sounding technology. *Imaging Spectrometry XIV*, International Society for Optics and Photonics, Vol. 7457, 745702, doi:10.1117/12.829344.
- Rodgers, C. D., 2000: *Inverse Methods for Atmospheric Sounding: Theory and Practice*, Series on Atmospheric, Oceanic, and Planetary Physics, Vol. 2. World Scientific.
- Romine, G. S., C. S. Schwartz, C. Snyder, J. L. Anderson, and M. L. Weisman, 2013: Model Bias in a Continuously Cycled Assimilation System and Its Influence on Convection-Permitting Forecasts. *Monthly Weather Review*, **141** (4), 1263–1284, doi:10.1175/MWR-D-12-00112.1.
- Rose, T., S. Crewell, U. Löhnert, and C. Simmer, 2005: A network suitable microwave radiometer for operational monitoring of the cloudy atmosphere. *Atmospheric Research*, **75** (3), 183, 200, doi:10.1002/we.1978.

- Saide, P. E., and Coauthors, 2015: Central American biomass burning smoke can increase tornado severity in the U.S. *Geophysical Research Letters*, **42** (3), 956–965, doi:10.1002/2014GL062826.
- Salesky, S. T., and W. Anderson, 2018: Buoyancy effects on large-scale motions in convective atmospheric boundary layers: Implications for modulation of near-wall processes. *Journal of Fluid Mechanics*, **856**, 135–168, doi:10.1017/jfm.2018.711.
- Salesky, S. T., and W. Anderson, 2020: Coherent Structures Modulate Atmospheric Surface Layer Flux-Gradient Relationships. *Physical Review Letters*, **125** (12), 124501, doi:10.1103/PhysRevLett.125.124501.
- San-Miguel-Ayanz, J., J. D. Carlson, M. Alexander, K. Tolhurst, G. Morgan, R. Sneeuwjagt, and M. Dudley, 2003: Current Methods to Assess Fire Danger Potential. *Wildland Fire Danger Estimation and Mapping*, Series in Remote Sensing, Vol. Volume 4, WORLD SCIENTIFIC, 21–61, doi:10.1142/9789812791177\_0002.
- Sathe, A., and J. Mann, 2013: A review of turbulence measurements using ground-based wind lidars. *Atmospheric Measurement Techniques*, **6** (11), 3147–3167, doi:10.5194/amt-6-3147-2013.
- Schaefer, J. T., 1974a: The Life Cycle of the Dryline. *Journal of Applied Meteorology (1962-1982)*, **13** (4), 444–449, URL <https://www.jstor.org/stable/26176495>.
- Schaefer, J. T., 1974b: A Simulative Model of Dryline Motion. *Journal of the Atmospheric Sciences*, **31** (4), 956–964, doi:10.1175/1520-0469(1974)031<0956:ASMODM>2.0.CO;2.
- Schroeder, J. L., W. S. Burgett, K. B. Haynie, I. Sonmez, G. D. Skwira, A. L. Doggett, and J. W. Lipe, 2005: The West Texas Mesonet: A Technical Overview. *Journal of Atmospheric and Oceanic Technology*, **22** (2), 211–222, doi:10.1175/JTECH-1690.1.
- Schultz, D. M., C. C. Weiss, and P. M. Hoffman, 2007: The Synoptic Regulation of Dryline Intensity. *Monthly Weather Review*, **135** (5), 1699–1709, doi:10.1175/MWR3376.1.
- Segales, A. R., B. R. Greene, T. M. Bell, W. Doyle, J. J. Martin, E. A. Pillar-Little, and P. B. Chilson, 2020: The CopterSonde: An insight into the development of a smart unmanned aircraft system for atmospheric boundary layer research. *Atmospheric Measurement Techniques*, **13** (5), 2833–2848, doi:10.5194/amt-13-2833-2020.
- Shin, H. H., and J. Dudhia, 2016: Evaluation of PBL Parameterizations in WRF at Subkilometer Grid Spacings: Turbulence Statistics in the Dry Convective Boundary Layer. *Monthly Weather Review*, **144** (3), 1161–1177, doi:10.1175/MWR-D-15-0208.1.

- Smith, E. N., J. G. Gebauer, P. M. Klein, E. Fedorovich, and J. A. Gibbs, 2019: The Great Plains Low-Level Jet during PECAN: Observed and Simulated Characteristics. *Monthly Weather Review*, **147** (6), 1845–1869, doi:10.1175/MWR-D-18-0293.1.
- Smith, E. N., and Coauthors, 2021: Evaluation and Applications of Multi-Instrument Boundary-Layer Thermodynamic Retrievals. *Boundary-Layer Meteorology*, **181** (1), 95–123, doi:10.1007/s10546-021-00640-2.
- Steenefeld, G. J., A. a. M. Holtslag, C. J. Nappo, B. J. H. van de Wiel, and L. Mahrt, 2008: Exploring the Possible Role of Small-Scale Terrain Drag on Stable Boundary Layers over Land. *Journal of Applied Meteorology and Climatology*, **47** (10), 2518–2530, doi:10.1175/2008JAMC1816.1.
- Stiperski, I., M. Calaf, and M. W. Rotach, 2019: Scaling, anisotropy, and complexity in near-surface atmospheric turbulence. *Journal of Geophysical Research: Atmospheres*, **124** (3), 1428–1448, doi:10.1029/2018JD029383.
- Stiperski, I., M. Chamecki, and M. Calaf, 2021: Anisotropy of Unstably Stratified Near-Surface Turbulence. *Boundary-Layer Meteorology*, **180** (3), 363–384, doi:10.1007/s10546-021-00634-0.
- Stull, R. B., 1988: *An Introduction to Boundary Layer Meteorology*. Softcover reprint of the original 1st ed. 1988 edition ed., Springer, Dordrecht.
- Tanner, B. D., E. Swiatek, and C. Maughan, 1996: Field comparisons of naturally ventilated and aspirated radiation shields for weather station air temperature measurements. *Conference on Agricultural and Forest Meteorology*, Vol. 22, 227–230.
- Tomaszewski, J. M., and J. K. Lundquist, 2021: Observations and simulations of a wind farm modifying a thunderstorm outflow boundary. *Wind Energy Science*, **6** (1), 1–13, doi:10.5194/wes-6-1-2021.
- Turner, D. D., and W. G. Blumberg, 2019: Improvements to the AERIoe Thermodynamic Profile Retrieval Algorithm. *IEEE Journal of Selected Topics in Applied Earth Observations and Remote Sensing*, **12** (5), 1339–1354, doi:10.1109/JSTARS.2018.2874968.
- Turner, D. D., and U. Löhnert, 2014: Information Content and Uncertainties in Thermodynamic Profiles and Liquid Cloud Properties Retrieved from the Ground-Based Atmospheric Emitted Radiance Interferometer (AERI). *Journal of Applied Meteorology and Climatology*, **53** (3), 752–771, doi:10.1175/JAMC-D-13-0126.1.
- Virtanen, P., and Coauthors, 2020: SciPy 1.0: Fundamental algorithms for scientific computing in Python. *Nature Methods*, **17** (3), 261–272, doi:10.1038/s41592-019-0686-2.

- Walters, J. E., L. R. Mason, K. Ellis, and B. Winchester, 2020: Staying Safe in a Tornado: A Qualitative Inquiry into Public Knowledge, Access, and Response to Tornado Warnings. *Weather and Forecasting*, **35** (1), 67–81, doi:10.1175/WAF-D-19-0090.1.
- Weckwerth, T. M., and D. B. Parsons, 2006: A Review of Convection Initiation and Motivation for IHOP\_2002. *Monthly Weather Review*, **134** (1), 5–22, doi:10.1175/MWR3067.1.
- Werner, C., 2005: Doppler Wind Lidar. *Lidar: Range-Resolved Optical Remote Sensing of the Atmosphere*, C. Weitkamp, Ed., Springer Series in Optical Sciences, Springer, New York, NY, 325–354, doi:10.1007/0-387-25101-4\_12.
- Wildmann, N., N. Bodini, J. K. Lundquist, L. Bariteau, and J. Wagner, 2019: Estimation of turbulence dissipation rate from Doppler wind lidars and in situ instrumentation for the Perdigão 2017 campaign. *Atmospheric Measurement Techniques*, **12** (12), 6401–6423, doi:10.5194/amt-12-6401-2019.
- Wildmann, N., M. Hofsäß, F. Weimer, A. Joos, and J. Bange, 2014: MASC—a small remotely piloted aircraft (RPA) for wind energy research. *Advances in Science and Research*, **11**, 55, doi:10.5194/asr-11-55-2014.
- Wildmann, N., S. Kigle, and T. Gerz, 2018: Coplanar lidar measurement of a single wind energy converter wake in distinct atmospheric stability regimes at the Perdigão 2017 experiment. *Journal of Physics: Conference Series*, **1037** (5), 052006, doi:10.1088/1742-6596/1037/5/052006.
- Wildmann, N., G. A. Rau, and J. Bange, 2015: Observations of the early morning boundary-layer transition with small remotely-piloted aircraft. *Boundary-Layer Meteorology*, **157** (3), 345–373, doi:10.1007/s10546-015-0059-z.
- World Health Organization, 2016: Ambient air pollution: A global assessment of exposure and burden of disease.
- Wulfmeyer, V., and Coauthors, 2018: A New Research Approach for Observing and Characterizing Land–Atmosphere Feedback. *Bulletin of the American Meteorological Society*, **99** (8), 1639–1667, doi:10.1175/BAMS-D-17-0009.1.
- Wyngaard, J. C., 2004: Toward Numerical Modeling in the “Terra Incognita”. *Journal of the Atmospheric Sciences*, **61** (14), 1816–1826, doi:10.1175/1520-0469(2004)061<1816:TNMITT>2.0.CO;2.
- Yong Han, and E. R. Westwater, 2000: Analysis and improvement of tipping calibration for ground-based microwave radiometers. *IEEE Transactions on Geoscience and Remote Sensing*, **38** (3), 1260–1276, doi:10.1109/36.843018.

- Zhang, Y., D. Li, Z. Lin, J. A. Santanello, and Z. Gao, 2019: Development and Evaluation of a Long-Term Data Record of Planetary Boundary Layer Profiles From Aircraft Meteorological Reports. *Journal of Geophysical Research: Atmospheres*, **124** (4), 2008–2030, doi:10.1029/2018JD029529.
- Zhou, B., Y. Li, and S. Miao, 2021: A Scale-Adaptive Turbulence Model for the Dry Convective Boundary Layer. *Journal of the Atmospheric Sciences*, **78** (5), 1715–1733, doi:10.1175/JAS-D-20-0240.1.
- Zhou, B., M. Xue, and K. Zhu, 2018: A Grid-Refinement-Based Approach for Modeling the Convective Boundary Layer in the Gray Zone: Algorithm Implementation and Testing. *Journal of the Atmospheric Sciences*, **75** (4), 1143–1161, doi:10.1175/JAS-D-17-0346.1.
- Ziegler, C. L., and C. E. Hane, 1993: An Observational Study of the Dryline. *Monthly Weather Review*, **121** (4), 1134–1151, doi:10.1175/1520-0493(1993)121<1134:AOSOTD>2.0.CO;2.
- Ziegler, C. L., and E. N. Rasmussen, 1998: The Initiation of Moist Convection at the Dryline: Forecasting Issues from a Case Study Perspective. *Weather and Forecasting*, **13** (4), 1106–1131, doi:10.1175/1520-0434(1998)013<1106:TIOMCA>2.0.CO;2.

## Appendix A

Run Name	Temperature Bias (°C)	Temperature Standard Dev. (°C)	WVMR Bias (g kg <sup>-1</sup> )	WVMR Standard Dev. (g kg <sup>-1</sup> )	Notes
AERI-only	1.05	1.07	0.30	1.05	These TROPoe retrievals exhibit the same patterns seen in the AERIOe retrievals from Chapter \ref{chap:intercomparions}
MWR-only	0.91	1.32	0.78	0.94	Higher WVMR bias than AERI-only, but lower standard deviation. MWRs are less sensitive to water vapor, but lower standard deviation could be due to the small sample size.
AERI+UAS	1.00	1.04	0.49	0.80	Minimal improvements for temperature, but the WVMR standard deviation shows improvements. WVMR bias is larger than AERI-only, but this could be due to sensor bias present on the CopterSondes or the radiosondes. Differences for temperature and WVMR are both exhibit more Gaussian distributions.
MWR+UAS	0.69	1.20	0.88	0.69	Shows similar improvements to AERI+UAS, though there is a larger impact on the temperature measurements.

Table A.1: Summary of results from the TROPoe tests presented in Section 4.2.2. The temperature and WVMR bias are relative to the measurements collected by the co-located Vaisala RS92-SGP radiosondes. The standard deviation is the standard deviation of the differences between the measurements from the retrieval and the radiosonde.